LUCAS SOARES PEREIRA

Numerical analysis of waste transport inside a building drainage network and sediments removal from ballast tanks using the Moving Particle Semi-Implicit

Revised version

São Paulo
2021

LUCAS SOARES PEREIRA

Numerical analysis of waste transport inside a building drainage network and sediments removal from ballast tanks using the Moving Particle Semi-Implicit

Revised version

Master thesis presented to the Polytechnic School at University of São Paulo as a requirement for obtaining the Master's degree in Science.

Area of Concentration: Construction Engineering

Advisor: Prof. Dr. Cheng Liang-Yee

São Paulo

2021

Este exemplar foi revisado e corrigido em relação à versão original, sob responsabilidade única do autor e com a anuência de seu orientador.

São Paulo, _____ de _____ de _____

Assinatura do autor: _____

Assinatura do orientador: _____

Catalogação-na-publicação

Pereira, Lucas Soares

Numerical analysis of waste transport inside a building drainage network and sediments removal from ballast tanks using the Moving Particle Semi Implicit / L. S. Pereira -- versão corr. -- São Paulo, 2020.

100 p.

Dissertação (Mestrado) - Escola Politécnica da Universidade de São Paulo. Departamento de Engenharia de Construção Civil.

1.Dinâmica de fluido computacional 2.Sistema de esgoto predial 3.Transporte de sólidos 4.Tanque de lastro 5.Remoção de sedimentos I.Universidade de São Paulo. Escola Politécnica. Departamento de Engenharia de Construção Civil II.t.

Pereira, L. S. Numerical analysis of waste transport inside a building drainage network and sediments removal from ballast tanks using the Moving Particle Semi-Implicit. 2021. Master thesis (Master's degree in Science) – Polytechnic School, University of São Paulo, São Paulo, 2021.

Approved on:

Master's Committee

Prof. Dr. _____
Institution _____
Judgement _____

Prof. Dr. _____
Institution _____
Judgement _____

Prof. Dr. _____
Institution _____
Judgement _____

ACKNOWLEDGMENTS

I would like to express my gratitude to Prof. Liang-Yee Cheng for being a present advisor, his vast knowledge and the valuable discussions during this research have inspired me to go always further.

I would like to thank the help of my colleagues of the MPS/TPN-USP group, Dr. Marcio Michiharu Tsukamoto, Dr. Fabio Kenji Motezuki, Dr. Cezar Augusto Bellezi, Dr. Rubens Augusto Amaro Junior, MSc Gabriel Henrique de Souza Ribeiro and Eng. Pedro Henrique Saggioratto Osello.

I would like also to say thanks to my parents, Joaquim and Zumira, my brother, Fabio, and my fiancée, Bárbara. Without their support this work would not be possible.

I would like to acknowledge the Conselho Nacional de Desenvolvimento Científico e Tecnológico (CNPq) for providing scholarship support during my Master study.

ABSTRACT

PEREIRA, L. S. Numerical analysis of waste transport inside a building drainage network and sediments removal from ballast tanks using the Moving Particle Semi-Implicit. 2021. Master thesis (Master's degree in Science) – Polytechnic School, University of São Paulo, São Paulo, 2021.

Fluid-solid interactions are complex dynamics phenomena with various applications in engineering, for example, fresh concrete flow, flow in a drainage system and sediment removal in ballast water exchange. Considering the complexity of those phenomena, the process cannot be precisely described through analytical solutions. The use of experimental models is an option, but due the high costs involved, this approach can be applied only for specific cases. Therefore, the computational approach has the advantages of flexibility and reduced costs. Traditionally, simulations of fluids are based on Eulerian description and meshes are necessary for the calculation. Over the years its disadvantages became clear when applying in phenomena with large deformation or moving boundary. Thereby, the meshfree methods were proposed to overcome these problems, an example is the Moving Particle Semi-implicit (MPS), it is based on a Lagragian description and discretization of the domain in particles. Originally, the MPS was developed for simulation of incompressible flows and was recently adopted in different applications. The advantage of the method is the capability to reproduce high non-linear phenomena with large deformation. In this study, the MPS is applied to investigate two processes involving fluid-solid interactions: waste transport inside a building drainage network, in which the solid is modeled as a rigid body, and sediments removal from ballast tanks, in which the sediments are modeled as denser fluids. The first study is a numerical investigation of the waste transport performance of a building drainage network under water conservation criteria, in which the reduced discharge volume results in an unsteady flow characterized by short duration and low energy. Due the intermittent flow in the initial sections of the drainage network, waste deposition in the horizontal drains that directly receive the effluents are of special concern. In the simulations, a simplified bathroom drainage model is adopted to investigate the influence of the pipe and discharge parameters. The hydrodynamics in the vicinity of a wye and its influence on the waste transport are also evaluated. Moreover, an investigation on the unphysical frictional loss inside a horizontal pipe due the wall boundary modeling is carried out. The results show that the pipe geometry modeling has significant influence on the numerical accuracy. In the second study, experiment and numerical simulations

were carried out aiming to investigate the effectiveness of the flow-through method on the removal of the sediment accumulated in double bottom ballast tanks, that might be a habitat for invasive species and represent a threat for the biodiversity. The effects of the flow rate and the density of the sediments were also considered. In addition to this, two tank modifications aiming to improve the sediment removal were also evaluated: the presence of a flow deflector and injection of water from the bottom. The results show that the flow-through ballast water exchange method might not be effective to remove the sediments entrapped between the bottom stiffeners, and the proposed modifications, despite challenging implementation, improve the sediment removal.

Keywords: Computational fluid dynamics. Particle-based method. Sediments removal. Solid transport. Ballast tank. Building drainage system.

RESUMO

PEREIRA, L. S. Análise numérica do transporte de resíduos sólidos em um sistema predial de esgoto sanitário e da remoção de sedimentos em tanque de lastro usando o *Moving Particle Semi-Implicit*. 2021. Dissertação (Mestre em ciência) – Escola Politécnica, Universidade de São Paulo, São Paulo, 2021.

Fenômenos interação fluido-sólido possuem diversas aplicações na engenharia como, por exemplo, no escoamento de concreto fresco, em fluxo de redes de esgoto e em tanques contendo sedimentos. Em face de sua complexidade, soluções analíticas não são capazes de descrevê-los com precisão. Uma alternativa é a utilização de abordagem experimental, porém, devido aos altos custos envolvidos, torna-se restrita a poucos casos. A abordagem computacional tem como vantagens flexibilidade e menores custos. Tradicionalmente, simulações de fluidos são baseadas na descrição Euleriana e utilização de malha. No entanto, as suas desvantagens ficam evidentes na simulação de fenômenos que envolvem grande deformação ou fronteiras móveis. Assim, de forma a contornar essas dificuldades métodos sem malha foram propostos, como, por exemplo, o *Moving Particle Semi-implicit* (MPS), que é baseado em descrição Lagrangiana e discretização do domínio em partículas. Originalmente, o MPS foi desenvolvido para a simulação de fluidos incompressíveis com superfície livre e recentemente foi adotado em diversas aplicações. A virtude desse método é a capacidade de simular fenômenos altamente não lineares com grandes deformações. Neste estudo, o MPS é utilizado para investigar dois fenômenos envolvendo interação sólido-fluido: transporte de resíduos em sistema de esgoto sanitário, no qual o sólido é modelo como um corpo rígido, e remoção de sedimentos em tanques de lastro, no qual o sedimento é modelo como um fluido denso. O primeiro estudo é uma investigação numérica do transporte de resíduos sólidos em uma rede predial de esgoto sanitário submetida a medidas de redução de consumo de água. Devido ao fluxo intermitente nos trechos iniciais da rede, a deposição de sólidos nos trechos horizontais que recebem os dejetos é especialmente preocupante. Nas simulações, um modelo simplificado da rede de esgoto sanitário de um banheiro é adotado para investigar a influência de parâmetros da tubulação e da descarga. A hidrodinâmica na região de uma junção a 45° e sua influência no transporte de sólido também são avaliados. Além disso, a perda numérica dentro uma tubulação horizontal decorrente da modelagem da parede também é investigada. Os resultados mostram que a modelagem da geometria da tubulação tem uma influência significativa na precisão das simulações. No segundo estudo, experimento e simulações computacionais foram realizados

para investigar a efetividade do processo do método *flow-through* na remoção de sedimento acumulado em tanques de lastro de duplo fundo, que pode ser um habitat para espécies invasoras e representar uma ameaça para a biodiversidade. Os efeitos da vazão e da massa específica dos sedimentos também foram considerados. Adicionalmente, duas modificações objetivando melhorar a remoção de sedimentos foram avaliadas: a presença de um defletor de fluxo e injeção de água pelo fundo. Os resultados mostram que o método *flow-through* pode não ser efetivo para remover sedimentos aprisionados entre os reforços estruturais do fundo do tanque de lastro, e as modificações propostas, apesar de sua desafiadora implementação, induzem ao aumento de remoção de sedimentos.

Palavras-chave: Dinâmica de fluido computacional. Método baseado em partículas. Remoção de sedimentos. Transporte de sólidos. Tanque de lastro. Sistema predial de esgoto predial.

LIST OF FIGURES

LIST OF TABLES

LIST OF ABBREVIATIONS

AABB	Axis-aligned bounding box
ABS	Acrylonitrile butadiene styrene
CFD	Computational Fluid Dynamics
DEM	Discrete Element Modelling
ERP	Explicitly represented polygon
IMO	International Maritime Organization
MPS	Moving Particle Semi-implicit
NPCD	Neighborhood particles centroid deviation
PVA	Polyvinyl Alcohol
PVC	Polyvinyl Chloride
SPH	Smoothed Particle Hydrodynamics
WC	Water closet

LIST OF SYMBOLS

Greek alphabet

α	coefficient of artificial compressibility
α_{rep}	repulsive coefficient
β	coefficient of free surface detection based on particle number density
γ	coefficient of relaxation
$\Delta\rho$	difference of density between fluids
Δh	water level difference between two connected tubes of a manometer
Δt	time step
δ	coefficient of free surface detection based on weighted centroid deviation
θ	deflector angle of the ballast tank model
λ	correction parameter
μ	kinematic friction coefficient
ν	kinematic viscosity
ξ_n	coefficient of collision
ρ	density
σ_i	weighted centroid deviation
ϕ	arbitrary function
ϕ_i	arbitrary function of particle i
ϕ_j	arbitrary function of particle j
$\Omega_{i'}$	set of neighbors of mirror particle i'
$\vec{\omega}$	angular velocity

Latin alphabet

A	flow cross-sectional area
A_0	number of sediment colored pixels at initial instant
A_n	number of sediment colored pixels at instant n
A_r	area ratio
$\vec{a}$	vector acceleration
a_0	parameter of acceleration intensity of the flow conditioning model

D	piping diameter
d	number of spatial dimensions
$\vec{f}$	external forces
$\vec{f}_c$	solid bodies contact force
$\vec{f}_g$	gravitational forces
$\vec{f}_h$	hydrodynamic forces
$\vec{f}_n$	normal component of the solid bodies contact force
$\vec{f}_t$	tangential component of the solid bodies contact force
g	gravitational field intensity
$\vec{g}$	gravitational field vector
h	water height
h_i	inflow height
h_{sed}	sediment material height
$\mathbf{I}$	matrix of inertia
i	pipe slope
L	characteristic linear dimension
l_0	initial distance between particles
$\vec{M}$	external moments
m	mass
n^0	particle number density for a complete support of neighbor particles
n^*	explicitly estimated particle number density
n^*_{avg}	average explicitly estimated particle number density of all fluid particles
n_i	particle number density of particle i
n^*_i	explicitly estimated particle number density of particle i
$\vec{n}_i^{wall}$	unit normal vector at the position of particle i
P	pressure
P_i	pressure of particle i
$\hat{P}_i$	minimum pressure between the neighborhood of particle i
$P_i^{t+\Delta t}$	pressure of particle i at instant $t + \Delta t$
P_j	pressure of particle j
P_w	wetted perimeter
Q	flow rate

Re	Reynolds number
R_h	hydraulic radius
Ri	Richardson number
$\mathbf{R}_i^{ref}$	transformation matrix
R_r	coefficient of sediment removal
$\vec{r}$	vector position of solid body center
r_e	effective radius
$\vec{r}_i$	vector position of particle i
$\vec{r}_{i'}$	vector position of mirror particle i'
$\vec{r}_i^*$	explicitly estimated vector position of particle i
$\vec{r}_i^t$	vector position of particle i at instant t
$\vec{r}_i^{wall}$	vector position of the closest point on the polygon to particle i
$\vec{r}_{ij}$	vector distance between particles i and j
$\left\|\vec{r}_{ij}\right\|$	distance between particles i and j
$\left\|\vec{r}_{ij}^*\right\|$	explicitly estimated distance between particles i and j
$\vec{r}_j$	vector position of particle j
s	scalar area of the solid body surface
$\vec{s}$	vector area of the solid body surface
T	dimensionless time
T^*	dimensionless time of the steady flow phase
T_t	dimensionless time of the end of the transient period
t	time
t_f	duration of the warming up phase of the flux control boundary condition
U	inflow velocity
u	magnitude of the vector velocity
$\vec{u}$	vector velocity
$\vec{u}_f$	steady velocity vector of the flux control boundary condition
$\vec{u}_i$	vector velocity of particle i
$\vec{u}_i^*$	explicitly estimated vector velocity of particle i
$\vec{u}_i^t$	vector velocity of particle i at instant t
$\vec{u}_i^{wall}$	vector velocity of the wall at the point at which acts the force of particle i
$\vec{u}_j$	vector velocity of particle j

V_b	ballast tank volume
V_d	discharge volume of WC flush
v_x	x component of magnitude velocity
W	width of the tank model
w	weight function
x_0	minimum limit of the flow conditioning region
x_f	maximum limit of the flow conditioning region
x_i	position of particle i in the x- axis
x_{ij}	distance between the particles i and j in the x-axis
y_{ij}	distance between the particles i and j in the y-axis
z_{ij}	distance between the particles i and j in the z-axis

CONTENTS

1 INTRODUCTION

Fluid-solid interactions are complex dynamics phenomena with various applications in engineering. The prediction of those phenomena is particularly challenging due large number of intervening factors that must be considered. Thus, analytical solutions are restricted to cases with quite simple geometry and physics. The experimental approach is an alternative to provide meaningful data to better understand the hydrodynamical process of complex cases. Moreover, the data obtained through experiments of reduced scale models can be used to validate numerical tools. However, this approach has as disadvantages the high costs involved and limitation due scale effects.

The numerical or computational approach is another option to investigate such complex phenomena. This approach has as advantages the flexibility to reproduce in detail complex geometries using real scale models and reduced costs compared with experiments. Traditionally, simulations of fluids are based on Eulerian description and meshes are necessary for the calculation. Over the years, the limitation of the mesh-based methods became clear when applying in phenomena with large deformation, moving boundary, fragmentation and merging of the free surface. Thereby, aiming to overcome these problems the meshfree methods were proposed, among them the particle-based ones. The advantage of the particle-based methods is the capability of reproduce high non-linear phenomena with large deformation.

An example of meshfree particle-based method is the Smoothed Particle Hydrodynamics (SPH), which was initially proposed for astrophysical problems and after was adapted to simulate incompressible flows (Gingold; Monaghan, 1977; Lucy, 1977). The Moving Particle Semi-implicit (MPS) is also a particle-based method, it is based on a Lagragian description and discretization of the domain in particles (Koshizuka, 1995; Koshizuka; Oka, 1996). Originally, the MPS was developed for simulation of incompressible flows and since then was adapted for different applications.

Despite of high computational costs, the MPS is well established in investigation of Newtonian fluid flows, as water. Recently, the method was applied in simulations of non-Newtonian fluids flows or multiphase flows, as for example in civil engineering, fresh concrete flow (Motezuki et al., 2015) and waste transport in building drainage network (Cheng et al., 2016a).

In this study, the MPS is applied to investigate two fluid-solid interaction processes: waste transport inside a building drainage network, in which the solid is modeled as a rigid body, and sediments removal from ballast tanks, in which the sediments are modeled as denser

fluids.

In recent years, the adoption of water saving practices and water closet (WC) of low flush volume decreased the flow rate inside the building drainage network resulting in an unsteady flow characterized by short duration and low energy for waste transport, especially in the initial sections of the drainage network. The horizontal drains that directly receive the effluent of the WC are of special concern since the reduced flow might compromise its self-cleaning performance. The aim of the study is to numerically investigate the flow inside a simplified bathroom drainage system and evaluate the influence of the WC flush volume, pipe diameter and pipe slope on the flow. Additionally, the effect of a wye on the solid transport performance is also investigated.

Concerning safety and stability of ships, when they are travelling with low or without cargo, ballast water is used, and seawater is the most often choice. During the ballasting operation small organisms are introduced, and when discharged they might represent a threat for the local biodiversity. In order to reduce the potential impact of invasive species transported inside ballast tanks, the exchange of the ballast water must be performed in regions where the invasive organisms have little chance to survive. Several studies were reported in the literature focusing on the analysis of the effectiveness of the ballast water exchange procedures, but the presence of sediments accumulated in the bottom of the ballast tanks is often neglected. The sediments accumulated in ballast tanks might be a habitat for invasive species, reducing the effectiveness of the ballast water exchange and degrading the ballast water.

The accumulation of sediments in the double bottom ballast water tanks are of special concern due the geometry that disfavor the sediment removal. Thus, the objective of the study is to investigate experimentally and numerically the process of sediment removal from double bottom ballast tanks during the flow-through ballast water exchange, in which pumping water three times the tank volume shall be performed. Two-dimensional reduced-scale model of one compartment of a double bottom ballast tank is adopted for experimental and numerical approaches. In the experiments, the sediments are represented using a granular material. The effects of the flow rate and the density of the sediments were also considered. In addition to this, the effectiveness of flow deflection devices and injection of water from the bottom of the tank on improving the effectiveness of the removal of sediments were also evaluated.

In the next chapter, the main features of the MPS method are described, including the governing equations, numerical operators, algorithm, and modeling of the boundary conditions. A new boundary condition is proposed aiming to model numerically the square mesh used in the experiments of double bottom ballast tanks with injection of water from the bottom.

Chapter 3 focuses on the analysis of hydrodynamics inside a building drainage network. Initially, a literature review about the flow in horizontal partially filled pipes and the impact of the reduction of the WC flush volume is presented. After that, the simplified bathroom drainage network model is described, and the results of the simulations are discussed. The effects of the pipe wall modeling technique are also investigated.

Chapter 4 concentrates on the analysis of sediment removal of double bottom ballast tanks. A literature review about the water exchange procedures and its effectiveness is presented. After that, the experimental apparatus, the material used as sediment in the experiments and the manometer calibration are showed. Next, the numerical results are discussed in comparison with experimental ones. Finally, chapter 5 provides the conclusions of the work and some recommendations for future research.

The investigations presented in this work were developed by the research group coordinated by Prof. Dr. Cheng Liang-Yee, within this context the contribution of the author to this work are the numerical modeling, simulations, validation, and analysis presented in chapter 3 and the experimental and numerical investigations, numerical modeling, simulations, validation, and data analysis of the chapter 4.

2 NUMERICAL METHOD

The numerical method adopted in this study is based on the Moving Particle Semi-implicit (MPS), which was originally proposed by Koshizuka and Oka, (1996) to simulate incompressible flows with free surface. The MPS is a Lagragian meshless method that discretize the space domain in particles and is suitable for modeling complex geometries with large displacements and deformation.

2.1 GOVERNING EQUATIONS

The governing equations of the fluid domain are the continuity equation and the momentum equation:

$$\frac{D\rho}{Dt} + \rho\nabla \cdot \vec{u} = 0 \tag{1}$$

$$\frac{D\vec{u}}{Dt} = -\frac{1}{\rho}\nabla P + \nu\nabla^2\vec{u} + \vec{f} \tag{2}$$

where ρ is density, t is time, $\vec{u}$ is the vector velocity, P is pressure, ν is the kinematic viscosity and $\vec{f}$ are the external forces.

2.2 NUMERICAL OPERATORS

In the solution of the governing equations, the differential operators are replaced by approximated discrete differential operators derived based on a weight function that depends on the distance between particles. The weight function can be given by

$$w\left(\left\|\vec{r}_{ij}\right\|\right) = \begin{cases} \dfrac{r_e}{\left\|\vec{r}_{ij}\right\|} - 1 & \left\|\vec{r}_{ij}\right\| \le r_e \\ 0 & \left\|\vec{r}_{ij}\right\| > r_e \end{cases} \tag{3}$$

where $\left\|\vec{r}_{ij}\right\|$ is distance between particles i and j and r_e is effective radius, which delimits the compact support, as showed in Figure 1. In addition, $\vec{r}_{ij} = \vec{r}_j - \vec{r}_i$, where $\vec{r}_i$ and $\vec{r}_j$ are the spatial position of the particle i and j, respectively. For the three-dimensional cases carried out in this work, r_e is set to $2.1l_0$, where l_0 is the initial distance between particles.

Figure 1 – Graphical representation of the weight function.

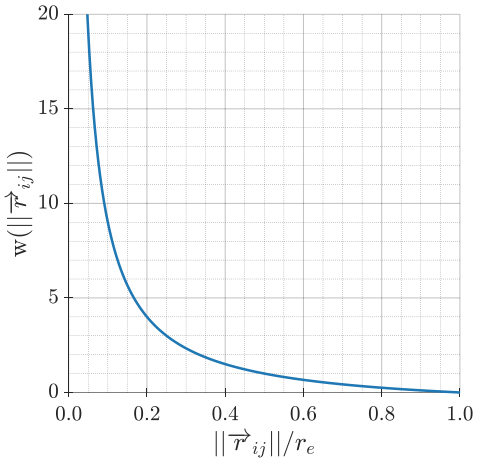

Source: the author.

For each particle i, the sum of the weight of all neighbor particles j inside the effective radius, is called as particle number density n_i:

$$n_i = \sum_{j \neq i} w(\|\vec{r}_{ij}\|) \tag{4}$$

as the particle number density is proportional to the density, it is used as a reference to ensure the incompressibility of the fluid.

For an arbitrary function ϕ and an arbitrary vector $\vec{\phi}$, the gradient, divergence and Laplacian operators of a particle i, considering the neighbor particle j, are defined respectively by:

$$\langle \nabla \phi \rangle_i = \frac{d}{n^0} \sum_{j \neq i} \left[\frac{(\phi_j - \phi_i)}{\|\vec{r}_{ij}\|^2} (\vec{r}_{ij}) w(\|\vec{r}_{ij}\|) \right] \tag{5}$$

$$\langle \nabla \vec{\phi} \rangle_i = \frac{d}{n^0} \sum_{j \neq i} \left[\frac{(\vec{\phi}_j - \vec{\phi}_i)}{\|\vec{r}_{ij}\|^2} (\vec{r}_{ij}) w(\|\vec{r}_{ij}\|) \right] \tag{6}$$

$$\langle \nabla^2 \phi \rangle_i = \frac{2d}{n^0 \lambda} \sum_{j \neq i} (\phi_j - \phi_i) w(\|\vec{r}_{ij}\|) \tag{7}$$

where d is the number of spatial dimensions, n^0 is the particle number density for a complete support of neighbor particles, $\langle \quad \rangle_i$ denotes discrete form and λ is a correction parameter given by:

$$\lambda = \sum_{j \neq i} \frac{\left\|\vec{r}_{ij}\right\|^2 w\left(\left\|\vec{r}_{ij}\right\|\right)}{\sum_{j \neq i} w\left(\left\|\vec{r}_{ij}\right\|\right)} \tag{8}$$

A modified pressure gradient was used to prevent unstable behavior when attracting forces act between particles. The pressure gradient can be calculated as:

$$\langle \nabla P \rangle_i = \frac{d}{n^0} \sum_{j \neq i} \left[\frac{\left(P_j - \hat{P}_i\right)}{\left\|\vec{r}_{ij}\right\|^2} \left(\vec{r}_{ij}\right) w\left(\left\|\vec{r}_{ij}\right\|\right) \right] \tag{9}$$

where $\hat{P}_i$ is the minimum pressure among the neighborhood of particle i, ensuring that only repulsive forces are present and avoiding particle clustering.

2.3 MODELING OF THE BOUNDARY CONDITIONS

2.3.1 Free surface

In the present work, the neighborhood particles centroid deviation (NPCD) method is adopted to identify the free-surface particles (Tsukamoto; Cheng; Motezuki, 2016). The NPCD method improves the stability and accuracy of the pressure computation by eliminating spurious oscillations due to misdetection of free-surface particles inside the fluid domain. In the NPCD technique, a particle is defined as free surface if:

$$\begin{cases} n_i < \beta \cdot n_0 \\ \sigma_i > \delta \cdot l_0 \end{cases} \tag{10}$$

the deviation σ_i is written as:

$$\sigma_i = \frac{\sqrt{\left(\sum_{j \neq i} w\left(\left\|\vec{r}_{ij}\right\|\right) x_{ij}\right)^2 + \left(\sum_{j \neq i} w\left(\left\|\vec{r}_{ij}\right\|\right) y_{ij}\right)^2 + \left(\sum_{j \neq i} w\left(\left\|\vec{r}_{ij}\right\|\right) z_{ij}\right)^2}}{\sum_{j \neq i} w\left(\left\|\vec{r}_{ij}\right\|\right)} \tag{11}$$

where x_{ij}, y_{ij} and z_{ij} are the distance between the particles i and j in the axes x, y and z, respectively. In this work, the coefficients β and δ are adopted equal to 0.97 and 0.2,

respectively. The Dirichlet pressure boundary condition is imposed to the detected free-surface particles.

2.3.2 Rigid wall

In the present study, the rigid walls were modeled using one of the two approaches: particle-based wall modeling and polygon wall modeling.

2.3.2.1 Particle wall modeling

The solid walls were modeled using three layers of fixed particles, as showed in Figure 2. The particles of the layer in contact with fluid particles are called wall particles, and the pressure of this layer is calculated together with the fluid particles using the Poisson's equation. The other two layers of fixed particles are called dummies particles, which are used only to ensure the correct calculation of the particle number density in the region of the wall.

Figure 2 – Solid wall boundary conditions.

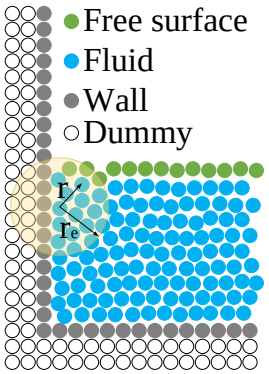

Source: the author.

2.3.2.2 Polygon wall modeling

The explicitly represented polygon (ERP) wall boundary model (Mitsume et al., 2015) is used to model the solid wall. The ERP model represents solid walls as triangular polygons in an explicit way without using distance functions. Moreover, the creation of virtual neighbor particles or special adaptations for angled edges are not required. It is worth noticing that in the ERP the Neumann boundary condition for pressure and the free-slip/no-slip condition for velocity on the walls are satisfied.

An axis-aligned bounding box (AABB) hierarchy, implemented using the C++ library libigl, is adopted in the present study to accelerate the calculation of the distances between the particles and polygons.

Since the solid walls are represented by polygons in the ERP model, the compact support of fluid particles near the walls is not fully filled with particles. Hence, the numerical operators of these particles are divided into the contribution due fluid particles $\langle\ \ \rangle^{particle}$, see Eqs. 5, 6 and 7, and due polygon walls $\langle\ \ \rangle^{wall}$, see Figure 3.

Figure 3 – Polygon wall modeling. Calculation of numerical operators with ERP model

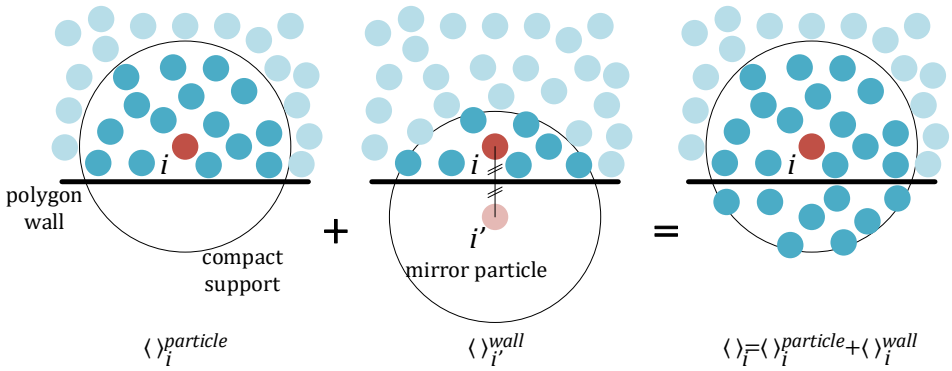

Source: Amaro Jr et al., 2019.

To calculate the numerical operators $\langle\ \ \rangle^{wall}$, first, the position of the mirror particle i' corresponding to particle i is computed by:

$$\vec{r}_{i'} = 2\vec{r}_i^{wall} - \vec{r}_i \tag{12}$$

where $\vec{r}_i^{wall}$ is the closest point on the polygon to particle i.

Afterwards, the pressure gradient and Laplacian of the velocity for the no-slip boundary condition of the mirror particle i' are computed considering its neighbors including the original particle i, the set $\Omega_{i'}$, and are multiplied by the transformation matrix $\mathbf{R}_i^{ref}$ or the identity matrix $\mathbf{I}$ (Mitsume et al., 2015):

$$\langle \nabla P \rangle_i^{wall} = \mathbf{R}_i^{ref} \frac{d}{n^0} \sum_{j \in \Omega_{i'}} (P_j + P_i - 2\bar{P}_i) \frac{(\vec{r}_j - \vec{r}_{i'})}{\|\vec{r}_{i'j}\|^2} w(\|\vec{r}_{i'j}\|) \tag{13}$$

$$\langle \nabla^2 \vec{u} \rangle_i^{wall} = -\mathbf{I} \frac{2d}{\lambda n^0} \sum_{j \in \Omega_{i'}} (\vec{u}_j - \vec{u}_{i'}) w(\|\vec{r}_{i'j}\|) \tag{14}$$

Finally, the operators are added to the numerical operators $\langle \quad \rangle^{particle}$ of particle i:

$$\langle \nabla P \rangle_i = \langle \nabla P \rangle_i^{particle} + \langle \nabla P \rangle_i^{wall} \tag{15}$$

$$\langle \nabla^2 \vec{u} \rangle_i = \langle \nabla^2 \vec{u} \rangle_i^{particle} + \langle \nabla^2 \vec{u} \rangle_i^{wall} \tag{16}$$

The transformation matrix for reflection across the plane $\mathbf{R}_i^{ref}$, whose unit normal vector at the position of particle i is $\vec{n}_i^{wall}$ is expressed as:

$$\mathbf{R}_i^{ref} = \mathbf{I} + 2\vec{n}_i^{wall} \otimes \vec{n}_i^{wall} \tag{17}$$

The Eq. 16 represents the Laplacian of velocity for the no-slip boundary condition on a wall whose velocity of the mirror particle is:

$$\vec{u}_{i'} = -\mathbf{I}\{\vec{u}_i - 2[\vec{u}_i^{wall} - (\vec{n}_i^{wall} \cdot \vec{u}_i^{wall})\vec{n}_i^{wall}]\} \tag{18}$$

where $\vec{u}_i^{wall}$ is the velocity of the wall at the point at which it is acted on by the force of particle i.

A repulsive force $\vec{f}_i^{rep}$ is added to Eq. 15 to prevent penetrations of the fluid particles at curved edges of the bodies:

$$\vec{f}_i^{rep} = \begin{cases} -\alpha_{rep}\left(\dfrac{0.5l_0}{\|\vec{r}_{ij}\|} - 1\right)\vec{n}_i^{wall} & \|\vec{r}_{ij}\| \le 0.5l_0 \\ 0 & \|\vec{r}_{ij}\| > 0.5l_0 \end{cases} \tag{19}$$

where α_{rep} is a repulsive coefficient empirically determined.

The particle number density n_i also is partitioned into the contribution due the fluid particles $n_i^{particle}$ and the polygon walls n_i^{wall}. Under the assumption that the wall near the fluid particle is flat, the dummy particles j' are arranged in a uniform particle distribution below the flat wall, and n_i^{wall} is evaluated using the dummies:

$$n_i^{wall} = f(d_{wall}) = \sum w(\|\vec{r}_{ij'}\|) \tag{20}$$

where f is determined by a linear interpolation of precomputed values at a given discrete distance d_{wall}. d_{wall} represents the normal distance between the fluid particle i and the nearest polygon wall. It should be emphasized that the values used to obtain f are computed at a few points within the effective radius r_e at the beginning of the simulation and are stored in a lookup table, then saving the processing time.

2.3.3 Rigid body dynamics

The rigid body is discretized by particles whose relative positions remain unchanged during the simulation. The governing equations of motion of rigid bodies are the translational and rotational motion equations:

$$m\vec{a} = \sum \vec{f} \tag{21}$$

$$\mathbf{I} \cdot \vec{\omega} + \vec{\omega} \times (\mathbf{I} \cdot \vec{\omega}) = \sum \vec{M} \tag{22}$$

where m is the mass of the rigid body, $\vec{a}$ is the acceleration at the center of the rigid body, $\vec{\omega}$ is the angular velocity about the principal axes of the rigid body and $\vec{M}$ is the external moment. The external forces considered are the gravitational $\vec{f_g}$, hydrodynamical $\vec{f_h}$ and contact between rigid bodies $\vec{f_c}$. The contribution of hydrodynamic and gravity force and the moment $\vec{M}$ acting on the rigid body are calculated as:

$$\vec{f_g} = m\vec{g} \tag{23}$$

$$\vec{f_h} = -\iint_S P d\vec{s} \tag{24}$$

$$\vec{M} = -\iint_S \vec{r} \times P d\vec{s} \tag{25}$$

where $\vec{g}$ is the gravitational field acceleration, P is the hydrodynamical pressure acting on the solid surface s and $\vec{r}$ is the position of the center of the rigid body. The shear forces are neglected, only the normal component of the hydrodynamic load is considered.

The normal $\vec{f_n}$ and tangential $\vec{f_t}$ components of the force of contact between rigid bodies are modeled using a penalty-based spring dashpot based on the Discrete Element Modelling (DEM) formulation (Cundall; Strack, 1979). The collision between rigid bodies is detected when the distance between the bodies is lower than the distance between particles l_0.

The normal force acting between the particles of the surface of the rigid bodies in contact is calculated following a non-linear Hertz's elastic contact theory (Johnson, 1985). The tangential force between the particles in contact is given by the minimum value either calculated following a Coulomb friction law or a linear model of repulsive and damped forces. The force of collision between the rigid bodies is the average value of the forces between the particles in contact. Moreover, the average moment between the particles in contact is applied in the center of mass of the rigid bodies (Amaro Jr.; Osello; Cheng, 2017).

2.3.4 Inflow

Inflow boundary condition is used to inject fluid particles during the simulation. From outside, the wall and dummies particles of the inflow section are displaced perpendicularly to the wall, when a wall particle crosses the wall edge, it is converted to a fluid particle. At the same time, the dummy particle behind is converted to wall, and a new dummy particle is added to assure that two layers of dummy particles are beside the wall particle and the particle number density is always correctly calculated.

2.3.5 Flow conditioning

For the recirculation of the fluid a flow conditioning proposed by Bellezi et al (2013) was adopted. The recirculation technique is shown in Figure 4. It is composed by a periodic boundary condition and flow conditioning technique to reproduce a close circuit flow recirculation in particle-based simulations.

Through the periodic boundaries, a particle that reaches the downstream limit of the computational domain is reintroduced in the upstream end, as inflow to the domain, with the same physical properties. Moreover, when calculating the discrete differential operators of the particles near the domain limits, the particles in the opposite side also must be considered. On the other hand, the flow conditioning technique is essentially the adjustment of the inflow velocity to the desired flow velocity profile. This adjustment is carried inside the flow conditioning region located immediately before the tank inlet (Figure 4).

Figure 4 – Recirculation boundary condition: inlet from side wall (a) and inlet from bottom (b).

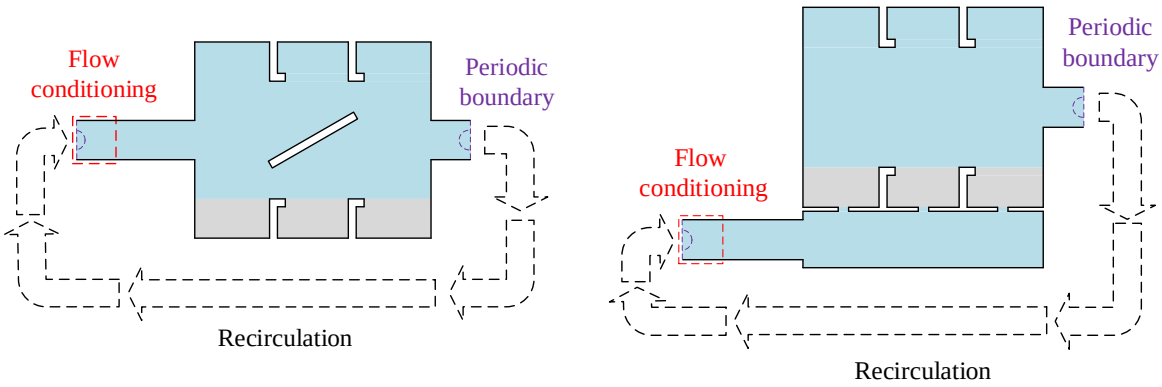

(a) (b)

Source: the author.

In the simulations, with the fluid starting from the rest, an acceleration field in the main flow direction is applied to the fluid. In this warming up process, only the periodic boundary condition is applied, and the acceleration is calculated by

$$a = \frac{3u_f}{t_r} \tag{26}$$

where u_f is the magnitude of the desired mean steady velocity in the main flow direction and t_r is the duration of the transient period.

After reaching the target velocity, in addition to the periodic condition, a flow conditioning is also applied to ensure that the velocity profile of the recirculation flow meets the desired inflow velocity profile. This is done by a modified Navier-Stokes equation with a numerical damping term:

$$\frac{D\vec{u}}{Dt} = -\frac{1}{\rho}\nabla P + \nu\nabla^2\vec{u} + \vec{f} + \frac{\partial\vec{u}_f}{\partial t} \tag{27}$$

where $\vec{u}_f$ is the vector velocity. The transverse components of the velocity are suppressed in the flow conditioning region and in the present study it is assumed that the target velocity profile at the inlet is uniform. The flow conditioner suppresses variations in mean flow velocity and adjusts the incoming recirculation particle velocity to desired inlet velocity within the flow conditioning region using a function of sinusoidal shape $f(x)$ and the velocity difference $\epsilon(\vec{u})$. Hence, the numerical damping term follows:

$$\frac{\partial \vec{u}_f}{\partial t} = \epsilon(\vec{u}) f(x) \rightarrow \frac{\partial \vec{u}_f}{\partial t} = (\vec{u}_f - \vec{u}) a_0 \frac{\sin\left(\pi \frac{x_i - x_0}{x_f - x_0} - \frac{\pi}{2}\right) + 1}{2} \quad (28)$$

where $\vec{u}$ is the particle velocity, a_0 is a numerical parameter to adjust the acceleration intensity, x_i is the particle position in the x-axis and x_0 and x_f are, respectively, the minimum and maximum limits of the flow conditioning region. The shape function $f(x)$ adjusts the intensity of the acceleration as a function of position on x-axis using a sinusoidal function in order to obtain a smooth transition of the incoming particles velocity to the desired inlet velocity, avoid discontinuity in the computational simulation and provide a stable computation.

2.3.6 Virtual strainer

In the investigation of the sediment removal due to ballast water exchange, to model numerically the square mesh used in the experiments in the cases with injection of water from the bottom, a new boundary condition is proposed in the present study.

Physically, the effect of the mesh is a strainer to restrict the downward motion of the sediments deposited on it. Numerically, this was implemented by assigning zero vertical component of the velocity of the sediment particles on the mesh when the vertical component is negative. This is done during the explicitly estimation of the vertical velocity of the sediment particles on the mesh, and it effectively avoid the sediment particles flow down through the openings, as showed in Figure 5.

Figure 5 – Virtual strainer boundary condition.

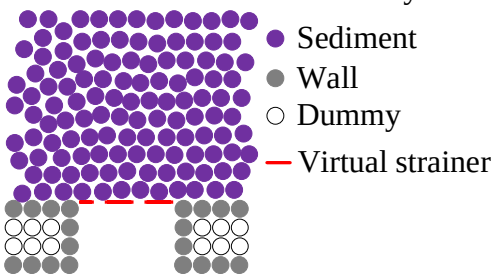

Source: the author.

2.4 ALGORITHM

The MPS adopts a semi-implicit algorithm. In each time step, velocity, position, and particle number density of all fluid particles are estimated explicitly considering the external forces and viscous term of the Navier-Stokes.

$$\vec{u}_i^* = \vec{u}_i^t + \left[\nu\langle\nabla^2\vec{u}\rangle_i + \vec{f}\right]^t \Delta t \tag{29}$$

$$\vec{r}_i^* = \vec{r}_i^t + \vec{u}_i^* \Delta t \tag{30}$$

$$n_i^* = \sum_{j \neq i} w\left(\left\|\vec{r}_{ij}^*\right\|\right) \tag{31}$$

Where $\vec{u}_i^*$, $\vec{r}_i^*$ and n_i^* are respectively the explicitly estimated velocity, position and particle number density of particle i, $\left\|\vec{r}_{ij}^*\right\|$ is explicitly estimated distance between particles i and j, $\vec{u}_i^t$ and $\vec{r}_i^t$ are the velocity and position of particle i at instant t, respectively, and Δt is the time step.

After the explicit prediction of velocity and position of the fluid particles, the pressure of all fluid and wall particles are calculated implicitly solving a Poisson's equation of pressure at $t + \Delta t$. The Poisson's equation is given by

$$\langle\nabla^2 P\rangle_i^{t+\Delta t} - \alpha\frac{\rho}{\Delta t^2}P_i^{t+\Delta t} = \gamma_1\frac{\rho}{\Delta t^2}\frac{n^0 - n_i^*}{n^0} + \gamma_2\frac{\rho}{\Delta t}\nabla\cdot\vec{u}_i \tag{32}$$

where γ_1 and γ_2 are relaxation coefficients used to reduce the pressure oscillation, α is the coefficient of artificial compressibility and $P_i^{t+\Delta t}$ is the pressure of particle i at instant $t + \Delta t$. In order to stabilize the calculations in confined flows without free surface, which do not have any Dirichlet boundary condition for pressure, a modified Poisson equation for pressure proposed by Arai et al. (2013) was adopted.

$$\langle\nabla^2 P\rangle_i^{t+\Delta t} - \alpha\frac{\rho}{\Delta t^2}P_i^{t+\Delta t} = -\gamma_1\frac{\rho}{\Delta t^2}\frac{n_i^* - n_{avg}^*}{n_{avg}^*} \tag{33}$$

Where n_{avg}^* is the average particle number density of all fluid particles in the intermediate step.

After the Poisson's equation is implicitly solved, the velocity and position of particles are corrected considering the pressure gradient term of Navier-Stokes.

$$\vec{u}_i^{t+\Delta t} = \vec{u}_i^* - \frac{\Delta t}{\rho}\langle \nabla P \rangle_i^{t+\Delta t} \quad (34)$$

$$\vec{r}_i^{t+\Delta t} = \vec{r}_i^* + \left(\vec{u}_i^{t+\Delta t} - \vec{u}_i^*\right)\Delta t \quad (35)$$

Where $\vec{u}_i^{t+\Delta t}$ and $\vec{r}_i^{t+\Delta t}$ are respectively the velocity and position of particle i at instant $t + \Delta t$. Table 1 summarizes the range, the adopted values and the reference study of the coefficients used in this study. The coefficients α_{rep}, γ_1 and γ_2 were calibrated for each simulation, while α, β and δ were adopted as suggested in the references.

Table 1 – Coefficients, range and adopted values.

Coefficient	Range	Adopted value	Reference
α	10^{-8}	10^{-8}	Ikeda et al. (2001)
α_{rep}	$10^6 - 10^7$	10^6	Mitsume et al. (2015)
β	$0.80 - 0.99$	0.97	Seiichi Koshizuka and Oka (1996)
δ	$0.15 - 0.25$	0.20	Tsukamoto et al. (2016)
γ_1	$0.001 - 0.01$	$0.0016 - 0.01$	Tanaka and Masunaga (2010)
γ_2	$-$	$0 - 0.05$	Lee et al. (2011)

In this study, a hybrid parallelized processing in computer cluster proposed by Fernandes et al. (2015) was adopted to speed up the simulations.

3 NUMERICAL INVESTIGATION ON THE HYDRODYNAMICS AND WASTE TRANSPORT IN HORIZONTAL DRAINS OF A BUILDING DRAINAGE NETWORK

The continued growth of urban areas imposes further pressure on the limited water resources, aiming to reduce the water stress, water management measures have been adopted, an example is the use of low flush volume water closet (WC). However, the reduced water consumption might compromise the self-cleaning performance of the building drainage network. The horizontal drains that directly receive the WC effluents are of special concern since the reduced discharge results in an unsteady flow characterized by shorter duration and lower energy for waste transport. The use of guides to design the drainage network that assume steady flow might lead to mis dimensioning of the pipes and increase the probability of solid deposition and clogging. In this way, sustainable provisions pose new challenges for an optimal design in building drainage infrastructure to ensure its self-cleaning performance.

The water flow through building drainage system is a highly nonlinear phenomenon that involves multiphase free-surface flows. In case of the partially filled horizontal pipes, it is predominantly a transient free-surface flow that interacts with solid wastes of complex geometries or sewages with a variety of rheological properties. Experimental investigations of the complex transient flow inside horizontal drains receiving the effluents of the WC flush discharge was carried out by Swaffield and McDougall (1996). The discharge of a WC flush generates a wave that propagates through the horizontal drain until a vertical stack. In long horizontal pipes, the wave becomes almost a stationary flow far from the WC, this effect was named wave attenuation. The wave attenuation pattern might result in a limited solid transport distance due the reduced downstream flow velocity (Littlewood and Butler, 2003).

In order to develop predictive models, Swaffield and McDougall (1996) experimentally studied the solid motion due WC flush discharge in horizontal drains and classified the transient flow in three phases. In the first phase, the solid is static, after the discharge of WC flush, the wave hits the solid, which is suddenly accelerated, but remains in contact with the pipe invert during the second phase. In the third phase, the solid free float with velocity higher than the main flow velocity because locally the flows velocity around the solid is higher. In general, the solid transport inside horizontal drains is dependent of the discharge flow rate, discharge time, pipe slope, pipe diameter and pipe roughness (McDougall and Swaffield, 2000). Also, the defective pipe slope and cross-section obstruction became of concern due the reduced flow inside drainage network (Swaffield et al., 1999).

The transported distance of a waste in a long pipe due single or repeated flushes of several different WC volumes was experimentally investigated by Kagami et al. (2013). An experiment performed with two WC flush volumes (4.8 L and 6.0 L) and two waste substitutes of PVA (Polyvinyl alcohol), indicated a minimum flow velocity for carrying the substitutes and a minimum water level upstream of the solid at which it is deposited (Akiyama et al., 2014). A study monitored the replacement of a WC of 6.8 L by a 4.8 L per flush and reported that the water consumption did not decrease due need of successive WC flushes (Valencio and Gonçalves, 2019). The authors also reported that the reduced flow might originate solid deposition in the initial sections of the sewage system.

Simplified analytical or semi-empirical approaches have been proposed to understand and predict the flow within pipes and to evaluate the self-cleaning performance of the drainage systems. An semi-empirical approach was adopted to obtain the parameters affecting the solid transport and predict the transported distance inside a building drainage network (Cheng et al., 2013). The method of characteristics is a velocity decrement model, in which the flow governing equations are combined to calculate the flow velocity and the water surface level, based on that the solid velocity and position are predicted (Swaffield and McDougall, 1996). Regarding the Mach number model, which requires only experimental reading of the height of water surface level, the method is capable of simulate the water level difference across the solid length. In this model, the presence of solid modifies the surrounding water, which in turn affects the solid transportation process (Gormley and Campbell, 2006).

Besides its simplifications, both methods require the experimental determination of the experimental parameters for each condition of pipe material, diameter, and slope. In this way, despite demanding higher computational cost, Computational Fluid Dynamics (CFD) techniques present the capability to simulate in-deep more complex scenarios under a variety of geometries and loading regimes, as well as considering the solid wastes and sewages. As an example, an Eulerian CFD technique based on volume of fluid model was employed to predict clogging locations in a building drainage system (Lee et al., 2013). In the simulations, a three-phase air-water-sludge model was adopted, in which the sludge was a high viscosity material.

Regarding the modeling of the complex fluid-solid interaction problem through more flexible and effective particle-based CFD techniques, a series of step-by-step investigations were reported using Moving Particle Semi-implicit (MPS) method. Initially, the effect of pipe diameter and pipe slope on the flow of a 6.0 L WC flush was investigated, the results showed a wave attenuation pattern in accordance with the literature (Cheng et al., 2012). In the following study, a more complex geometry of a building drainage network was proposed to

analyze the effect of the discharge of a wash basin and a shower of a secondary drain to the flow of WC effluent in the main drain (Cheng et al., 2013). The flow was also applied in a horizontal pipe at a base of a vertical stack. Another study investigated the effect of three geometries of the elbow (90° elbows with long radius, 90° elbows with short radius and a sequence of two 45° elbows) at a vertical stack's base on the waste transport in a horizontal drain (Cheng et al., 2014). The waste was modeled as a sludge with high viscosity. The next study focused on the effects of the pipe diameter and pipe slope on the solid waste transport inside horizontal drain, in which the solid was modeled as a discrete and rigid body (Cheng et al., 2016). An investigation on the influence of the initial position of the rigid solid inside a horizontal drain submitted to a WC flush was also carried out (Cheng et al., 2017).

The present chapter is divided in two studies. In the first part, an investigation on the hydrodynamics in the vicinity of a wye in a building drainage system is carried out. In the second part, an investigation on the unphysical frictional loss inside a horizontal pipe is carried out since the modeling of the pipe geometry has significant influence on the numerical accuracy. Two wall boundary modeling are adopted: in the first one all domain is modeled by particles and in the second one the fluid domain is represented by particles whereas wall boundaries are modeled by triangular polygons. Considering partially pipe flow with relatively low water level, the air inside the pipe and the air pressure oscillation due its entrapment was neglected in the current simulations.

3.1 INFLUENCE OF A WYE ON THE HYDRODYNAMICS AND WASTE TRANSPORT

In the current section, a simplified bathroom drainage system is studied aiming to evaluate the influence of a wye on the flow, the model adopted is the same used in (Cheng et al., 2013). Additionally, the effect of the wye on the solid transport performance is also investigated. Furthermore, the influence of the WC flush volume, pipe diameter and pipe slope on the flow and solid transport are analyzed. In the simulations, the conventional wall boundary modelling with discrete wall and dummy (ghost) particles is adopted.

3.1.1 Description of the cases

The simulated model consists of two horizontal pipes, the drain 1 receives the discharge of a WC and the drain 2 connects to a trap that receives the effluent of a shower and a wash

basin. Both drains are connected through a wye to a stack. Figure 6 shows the main dimensions of the simulated model. Aiming to investigate the influence of the parameters of the drain 1 on the flow, simulations with two diameters (75 and 100 mm) and three pipe declivities (0%, 1% and 2%) were carried out. The pipe diameter of the drain 2 was adopted 50 mm. The height of the water surface level was measured by 6 sensors positioned in the sections S1 to S6, as illustrated in Figure 6.

Figure 6 – Main dimensions and positions of the sensors of the simulated model (in meters).

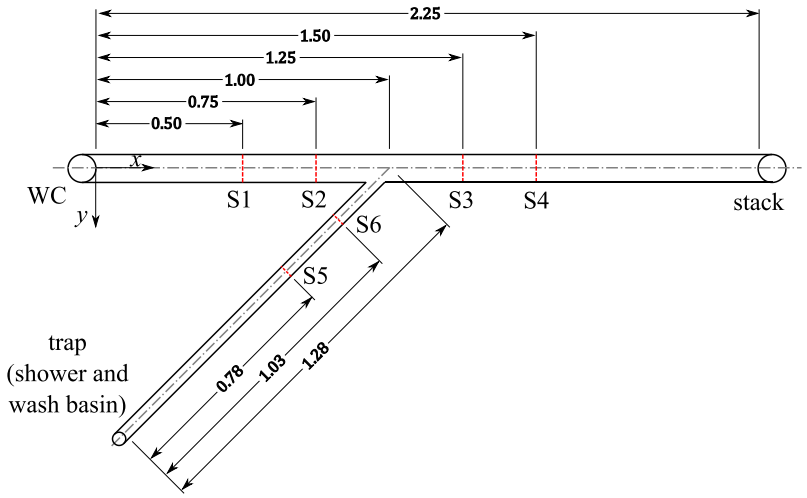

Source: the author.

Since shower and WC flush discharges have different time scales, from several minutes to few seconds, respectively, and focusing on the effects of the WC flush, while the flow rate from the shower is considered constant, the WC flush is considered transient. During the simulation, a constant flow rate of 0.35 L/s, resulting from the contributions of a shower (0.2 L/s) and a wash basin (0.15 L/s), was imposed as a boundary condition upstream of the drain 2. At 10 s, the flow inside the drains reaches steady state, then the WC flush is discharged upstream in the drain 1. In order to investigate the impact of the reduction of WC flush volume on the performance of the drainage system, two WC flush volumes (4.8 and 6.0 L) were simulated. Figure 7 shows the experimentally obtained discharge flow rate and accumulated volume of the WC flushes used in the simulations. The total duration of the simulations was 20 s.

Figure 7 – Discharge flow rate (a) and volume (b) of WC flushes, experimentaly obtained.

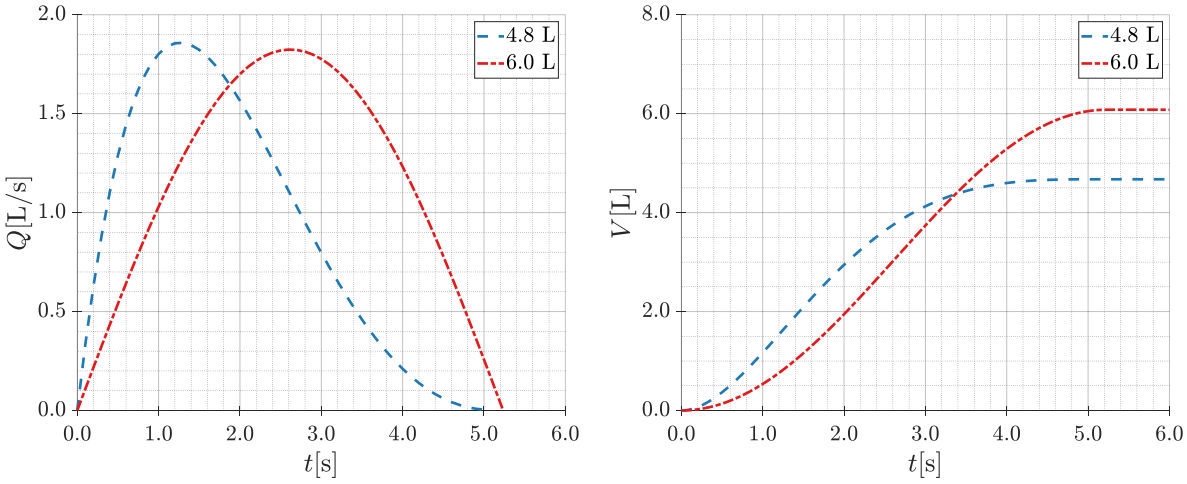

(a) (b)

Source: the author.

The solid transport performance was evaluated by using a cylindrical-shape rigid body positioned upstream of the drain 1 at beginning of the simulation. The material and dimensions of the free solid was based on the waste substitute of experimental study carried out by Akiyama et al. (2014). The cylinder has diameter of 30 mm and length of 80 mm. The material of pipe and solid are PVC (polyvinyl chloride) and PVA (polyvinyl alcohol), respectively. Table 2 presents material properties, as density ρ, mass m and numerical parameters, as collision between solids coefficient $\boldsymbol{\xi_n}$ and friction coefficient μ, used in the simulations.

Table 2 – Material properties and numerical parameters.

Material	ρ [kg/m³]	m [kg]	$\boldsymbol{\xi_n}$	μ
Solid	1010	0.06	0.05	–
Pipe	∞	∞	–	0.22

Source: the author.

The simulations were performed with distance between particles of 2.0 mm and time step of 10^{-4} s. The pressure smooth coefficient (γ_1) and the artificial compressibility coefficient (α) adopted were 0.01 and 10^{-8}, respectively. For the chosen resolution, at final instant the models have approximately 1.6 million of particles. The processing time for each case was approximately 50 hours using 8 nodes of computer cluster of the Numerical Offshore Tank (TPN/USP) (Cluster with 184 dedicated nodes Sun Blade X6275-2 Intel© Xeon© Processors X5560, 4 cores, 2.8 GHz and 24 GB of memory each).

Table 3 presents the nomenclature of the simulated cases. Two simulations were carried out for each case, the first without the solid aiming to analyze the hydrodynamic flow and the second with solid aiming to investigate the solid transport performance.

Table 3 – Nomenclature of the simulated cases.

Cases	WC flush volume V_d [L]	Drain 1 diameter D [mm]	Pipe slope i [%]
V48D075A0	4.8	75	0
V48D075A1	4.8	75	1
V48D075A2	4.8	75	2
V48D100A0	4.8	100	0
V48D100A1	4.8	100	1
V48D100A2	4.8	100	2
V60D075A0	6.0	75	0
V60D075A1	6.0	75	1
V60D075A2	6.0	75	2
V60D100A0	6.0	100	0
V60D100A1	6.0	100	1
V60D100A2	6.0	100	2

Source: the author.

3.1.2 Results and discussions

3.1.2.1 Hydrodynamic analysis

Figure 8 exhibits snapshots of the simulation of the cases V60D075A0 and V48D100A2. The snapshots show a view of the horizontal pipe model, in which the color scale of the fluid particles represents the magnitude of the flow velocity. The presented cases, V60D075A0 and V48D100A2, are extremes of simulations, the first one has higher WC flush volume, lower pipe diameter and slope, while the second one has lower WC flush volume, higher pipe diameter and slope. At 10 s, the WC flush is discharged generating a wave that propagates inside the drain 1.

Figure 8 (a) presents the flow inside horizontal drains for the case V60D075A0. The WC discharged wave flow through the wye at about 12.2 s. After 13 s, in the case V60D075A0 there is an increase of the water surface level in the drain 2 from the wye to upstream, at 15 s, the drain 2 is almost completely full filled. After end of the WC discharge, a backwater wave propagates inside the drain 1 reaching the pipe beginning at about 15 s, when the backwater

wave hits the upstream wall of drain 1, it returns flowing downward the pipe reaching the wye at 17 s. The water surface level of the drain 2 decreases after end of WC discharge, returning to the level before the WC discharge at 18 s.

Figure 8 (b) presents the flow inside horizontal drains for the case V48D100A2. After the wave front reaches the wye, at about 11.7 s, the height of the water surface level of drain 2 remains unaltered. Furthermore, the backwater wave inside the drain 1 does not occurs. The height of water surface level returns rapidly to the initial condition after end of WC flush discharge.

Figure 8 – Snapshots of the simulations of the cases V60D075A0 (a) and V48D100A2 (b) without solid.

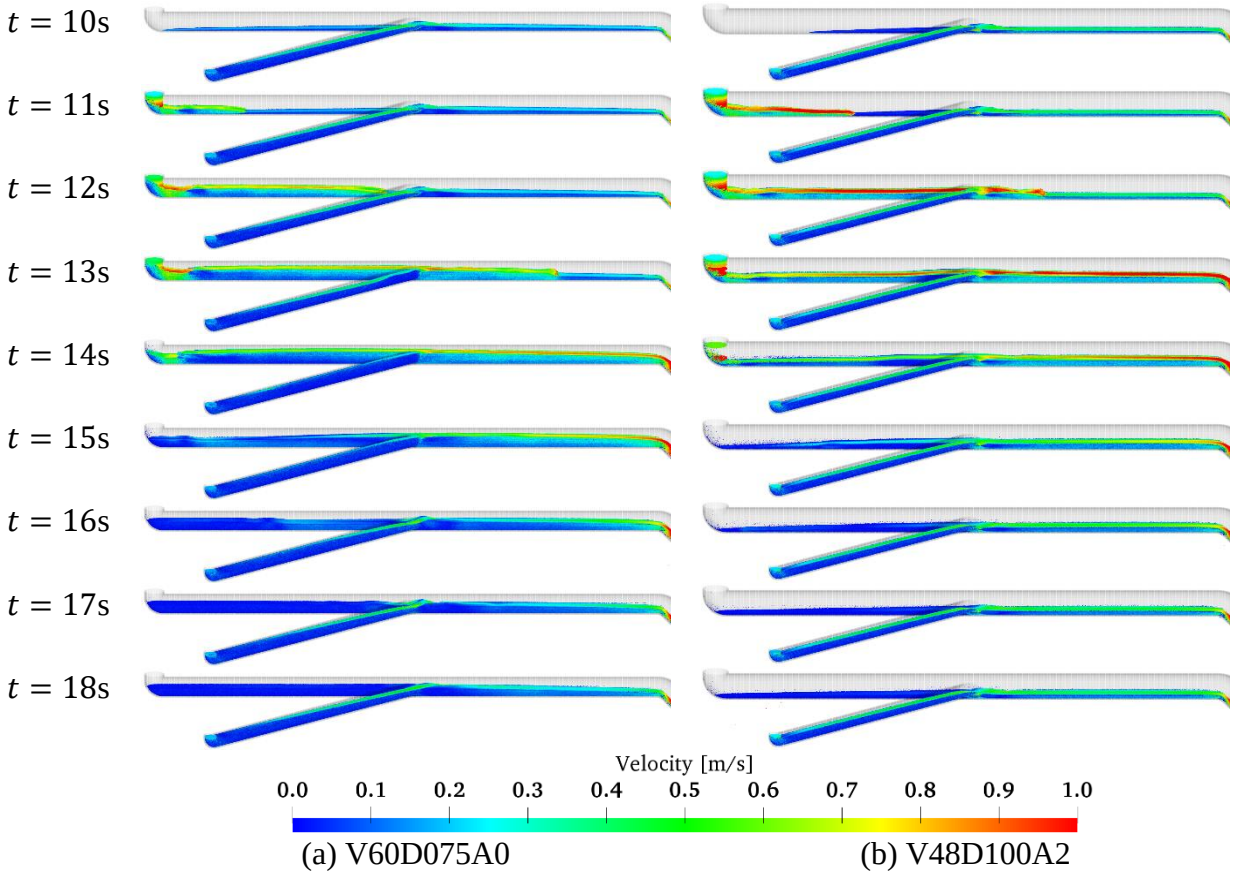

Source: the author.

Figure 9 shows the time series of height of water surface level in the sections from S1 to S6 for cases V48D075A0 and V60D100A2. The curves of height of water surface level in sections that are located 0.25 m from the wye (S2, S3 and S6) are represented with darker color, while the curves of the sections with a distance of 0.50 m from the wye (S1, S4 and S5) are represented with lighter colors. The sensors from S1 to S4 are located in the drain 1 and the sensors S5 and S6 are located in drain 2, as showed in Figure 6.

At 10 s, the flow from the trap due the discharge of the shower and wash basin reached steady state, the water level measured in the sensors of the drain 2 is constant. Before the WC flush discharge, the height of water surface level in sensor S5 are approximately 42 and 35 mm for the cases V48D075A0 and V60D100A2, respectively. After the WC flush discharge, the height of water surface level in the drain 1 quickly increases.

As showed in Figure 9 (a), at 13 s, the sensor S2 of the case V48D075A0 has a peak of about 52 mm related with the flow through of the wavefront of the WC flush. After a decrease of the height of water surface level, at about 16 s, the height of the water surface level increases again. The second peak is related with the encounter of the discharges in the wye, which originate a backwater wave in the drain 1 of the cases with lower diameter (75 mm) and lower pipe slope (0 and 1%). The magnitude of the backwater wave height depends on WC flush volume and pipe slope, the oscillation of the water level is about 10 mm for the critical case V60D075A0.

In comparison, the curve of the height of the water surface level of the sensor S2 of the case V60D100A2, showed in Figure 9 (b), has only one peak of about 45 mm at 14.5 s. After the end of the WC flush discharge, the water surface level inside the drain 1 quickly decreases.

Figure 9 – Height of water surface level in the sections S1 to S6 for the cases V48D075A0 (a) and V60D100A2 (b).

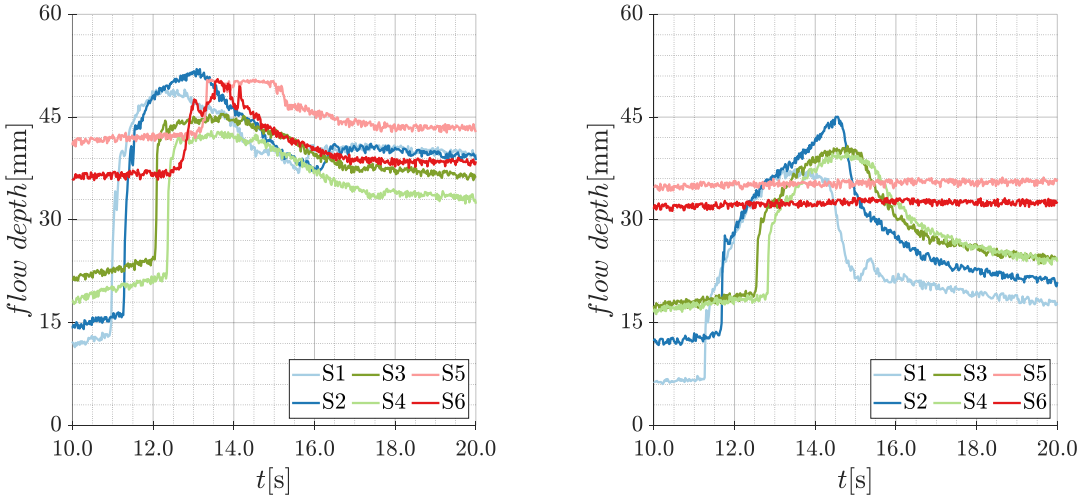

(a) (b)

Source: the author.

Figure 10 exhibits the time series of the pipe filling in the sections from S1 to S6 for the cases V60D075A0 and V60D075A2. In cases with diameter of 75 mm, the WC flush discharge in the drain 1 leads to the increase of the water surface level in the drain 2. In case V60D075A0 (Figure 10 (a)), the pipe filling in the sections of the drain 2 (S5 and S6) remains higher than

0.85 for almost 3 s, that might indicate a flow regime change (Ng et al., 2018). In comparison, in the case with higher slope V60D075A2 (Figure 10 (b)), the pipe filling of the sections of the drain 2 remains always below the mentioned threshold.

Figure 10 – Pipe filling in the sections S1 to S6 for the cases V60D075A0 (a) and V60D075A2 (b).

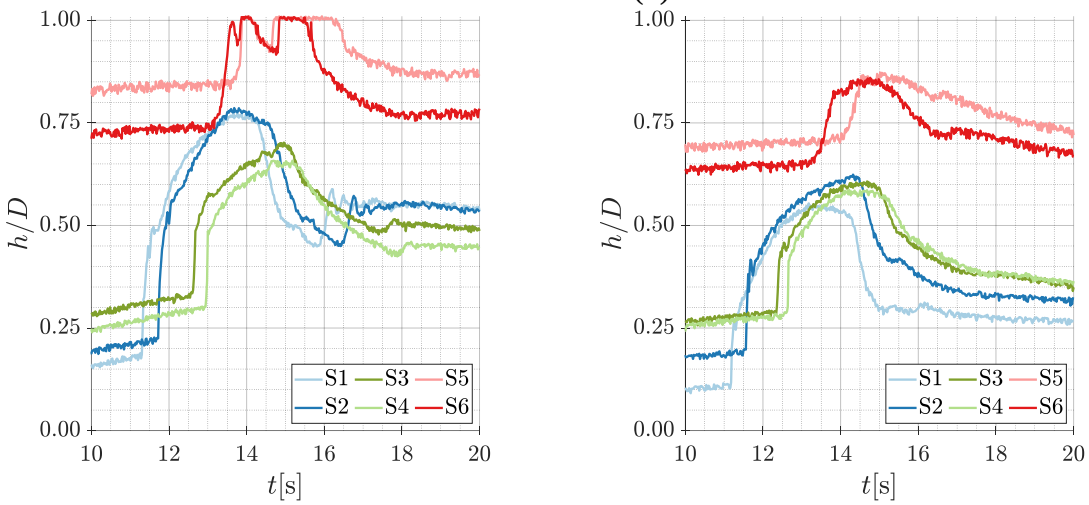

Source: the author.

It is important to point out that while the fluid is subjected to atmospheric pressure in the partially filled pipe, the fully filled pipe is subjected to a pressure-driven flow, in which the pipe flow rate is lower in comparison with the free surface flow, and the pressure oscillation caused by the fully filled pipe flow might compromise trap seals. Moreover, when the pipe section is almost completely full with the pipe filling close to 1.0, the air entrapped cannot be neglected. In this way, in those conditions the current numerical model cannot correctly reproduce the flow.

Figure 11 presents the maximum pipe filling in section S6 of the drain 2 as a function of slope for all simulated cases. In general, the pipe filling of the cases with diameter of 75 mm is higher than the cases with 100 mm. Also, the increase of the pipe slope results in lower value of maximum pipe filling. Finally, the case with diameter of 75 mm and WC flush volume of 4.8 L, results in lower pipe filling than the WC flush volume of 6.0 L, specially for the case with 1 % slope.

Figure 11 – Maximum pipe filling in section S6 as a function of slope for simulated cases.

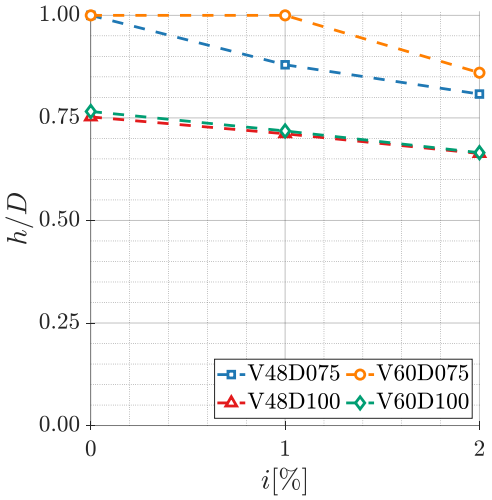

Source: the author.

3.1.2.2 Solid transport

In the second phase of the study, a rigid solid was positioned at the beginning of the simulations upstream in the drain 1 aiming to evaluate the solid transport performance of the simplified bathroom drainage model.

Figure 12 shows snapshots of the simulations with solid for the cases V48D100A0 and V60D075A2. The color scale of the fluid particles represents the magnitude of the flow velocity.

In case V48D100A0 (Figure 12 (a)), at 10 s, the WC flush is discharged, the wavefront hits the solid, that is suddenly accelerated and slides in contact with the pipe invert. When the solid approaches the wye, the solid velocity decreases due to the influence of the flow from the drain 2. At 14 s, the solid stops and remains deposited until the end of the simulation.

In case V60D075A2 (Figure 12 (b)), the solid is also accelerated after the WC flush discharge, sliding in pipe invert. When it approaches the wye, the solid velocity decreases, the height of the water surface level upstream of the solid increases and the solid is entirely lifted off. After the wye, the solid velocity increases again, reaching the stack before 14 s.

Figure 12 – Snapshots of the simulations of the cases V48D100A0 (a) and V60D075A2 (b) with solid.

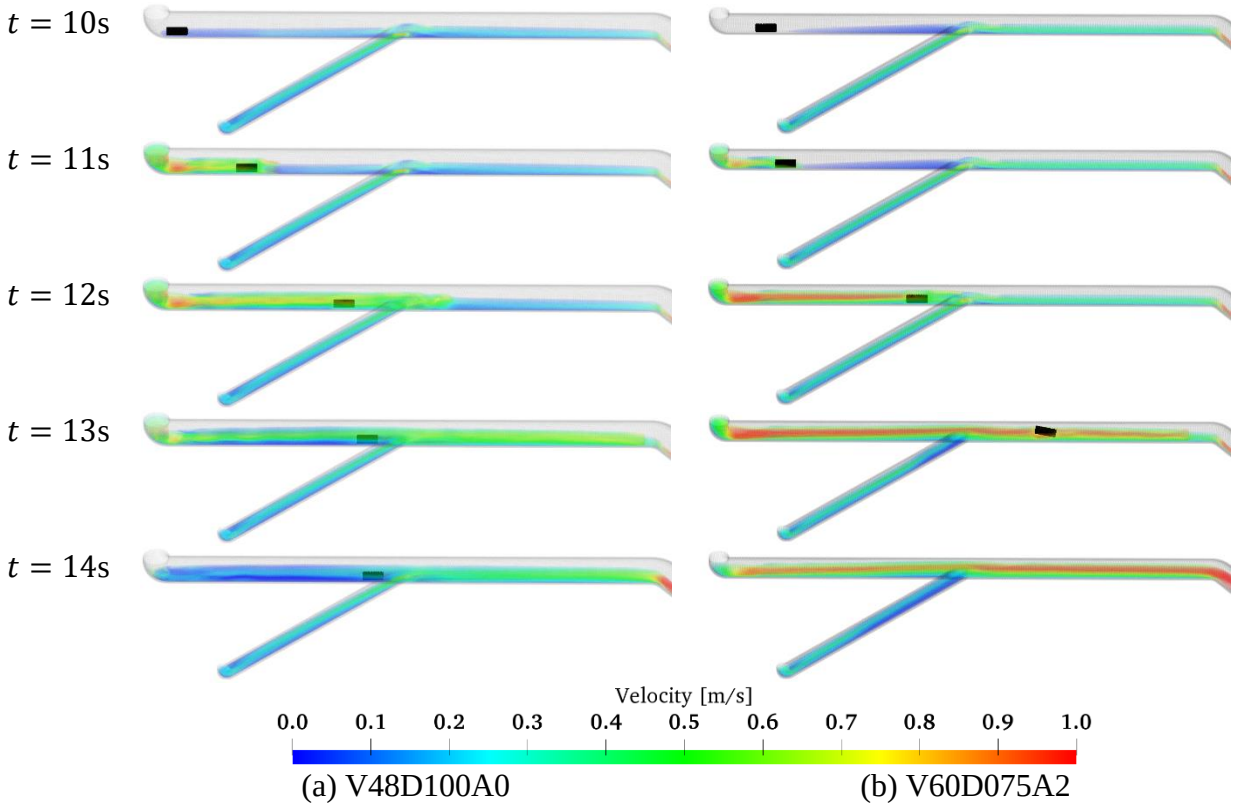

(a) V48D100A0 (b) V60D075A2

Source: the author.

Figure 13 exhibits time series of the solid position in the drain 1 for all simulated cases. The axes of the coordinate system are showed in Figure 6, where the origin of x-axis is in the begin of the drain 1. In the cases with pipe slope of 1% or 2%, before the WC flush discharge the solid slowly slides in the pipe invert, therefore, at 10 s, the solid position is slightly different for each case. When the wavefront of the WC flush discharge reaches the solid, the curves exhibit an inflection related with the increase of velocity of the solid.

In general, of the 12 simulated cases, in 2 conditions the solid did not reach the stack during the simulation (Figure 13 (b)), namely V48D100A0 and V60D100A0, both with diameter of 100 mm and null pipe slope. Although the curves of the two cases between 10 s and 12 s are similar to those of higher slope cases, when the solid approaches the wye, the curves exhibit a second inflection and the solid remains deposited until simulation end 0.9 m downstream from its initial position.

Considering the two cases with diameter of 100 mm and pipe slope of 1%, the solid flow through the wye with difficult, which can be seen in the slope change of the solid's position curve when it is approaching 1.0 m. The time needed to reach the stack was lower for the cases

with pipe slope of 2% (dotted lines of Figure 13). In these cases, the solid reached the stack in less than 4 s.

Figure 13 – Time series of the solid position in x-axis with diameter of 75 mm (a) and 100 mm (b).

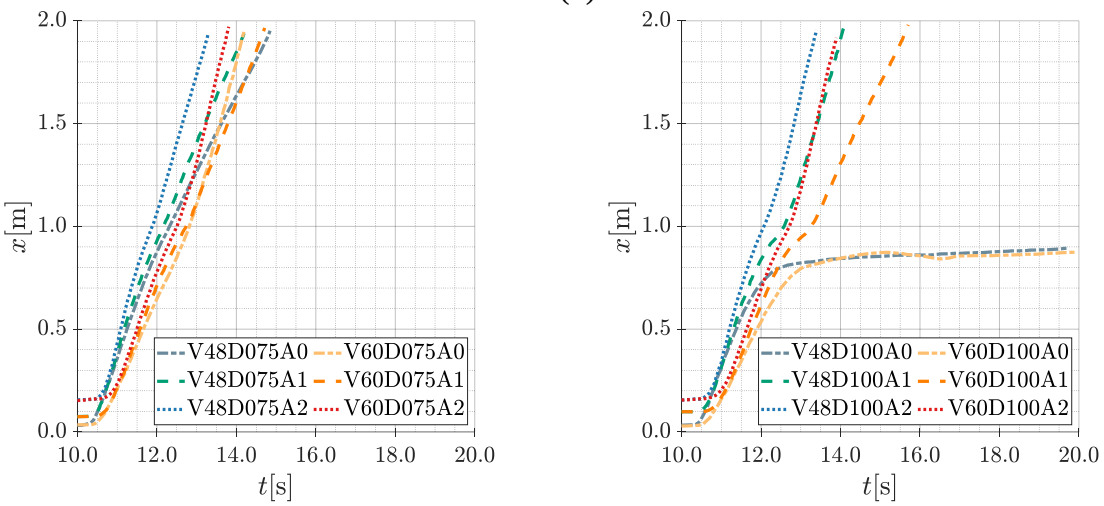

(a) $D = 75$ mm (b) $D = 100$ mm

Source: the author.

Figure 14 presents the time series of the solid velocity in the drain 1 for the simulated cases. After the wave front of the WC flush discharge hits the solid, it is suddenly accelerated until reaches between 10.5 s and 12.0 s a peak of velocity, which ranges from 0.4 m/s in case V60D100A0 to 0.8 m/s in case V48D075A2. The first velocity peak of the solid is related with the velocity of the surge wave of WC discharge, which is dependent of the diameter and WC flush flow rate.

Considering a partially filled pipe, the smaller the pipe diameter, the faster the wave flows inside the pipe. Regarding to the WC flush flow rate, despite lower fluid volume of the flush of 4.8 L, the shorter time duration of the discharge results in a slightly higher flow rate peak in comparison with the flush of 6.0 L (Figure 7). Therefore, the cases with 4.8 L WC flush volumes exhibit higher velocity peak. The first phase of the solid motion, before the wye, is dominated by remarkably high impulsive hydrodynamic loads.

When the solid is approaching the wye, it is deaccelerated due to the influence of the flow incoming from the drain 2. In cases V48D100A0 and V60D100A0, the solid velocity decreases, stops near 14.0 s and remains deposited until end of simulation (Figure 14 (b)). In the other cases, the reduction of the solid velocity is not enough for its deposition, after it flows through the wye, the solid is reaccelerated. As an example, the solid in the case V60A100A1

has its velocity decreased to 0.17 m/s in the wye region and after flowing through the wye is reaccelerated, reaching the stack with velocity of 0.5 m/s.

In general, the final velocity of the solid exceeds the velocity peak before the wye, because while in the first phase the solid slides in the pipe invert, in the second phase, after the wye, due to the flow from the drain 2, the solid free floats, which reduces the friction due to the contact with the pipe, while receives additional thrust and is further accelerated. Moreover, in the second phase of the solid motion hydrostatic head and pipe slope become relevant.

Figure 14 – Time series of the solid velocity in x-axis with diameter of 75 mm (a) and 100 mm (b).

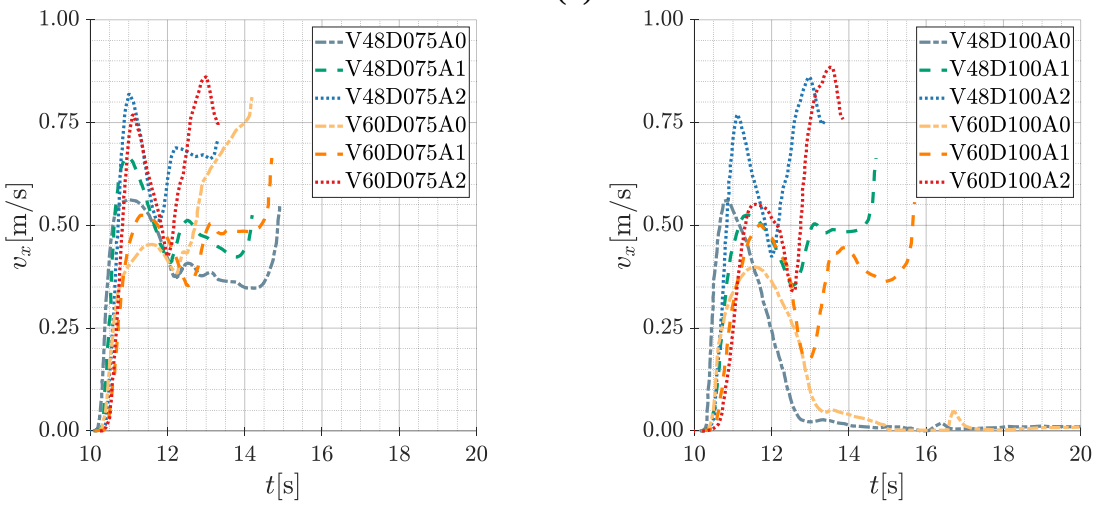

(a) $D = 75$ mm (b) $D = 100$ mm

Source: the author.

3.2 INFLUENCE OF THE WALL BOUNDARY MODELING OF CIRCULAR GEOMETRIES

In the conventional implementation of particle-based methods, wall boundaries are modeled by discrete wall and dummy (ghost) particles. A smoother representation of circular geometries using the particle modeling requires very high resolution, otherwise, it may result in inaccurate geometrical representations that may cause abnormal flow near the wall boundaries or unphysical frictional forces on the near wall fluid particles.

In order to address this issue, the adoption of polygons mesh to represent the wall boundaries is an alternative modeling technique. Aiming to verify the effectiveness of the polygonal mesh modeling, a transient free-surface flow inside a horizontal pipe considering two pipe wall modeling is simulated in the present research. In the first one all domain is modeled

by particles and in the second one the fluid domain is represented by particles whereas wall boundaries are modeled by triangular polygons.

3.2.1 Description of the cases

The simulated model represents a horizontal pipe of diameter $D = 0.05$ m and length 1.0 m subject to a constant inflow $Q = 0.35$ L/s combined with outflow at the end of the pipe (see Figure 15). Three inflow heights (h_i) were considered, namely $0.05, 0.025$ and 0.0125 m, given the relations $h_i/D = 1.0, 0.5$ and 0.25. In order to monitor the water level in the pipe, 2 probes were placed at 0.50 m (S1) and 0.75 m (S2) from the upstream inflow section. The duration of simulations was 20 s.

Figure 15 – Main dimensions and sensor position of the simulated model (in meters).

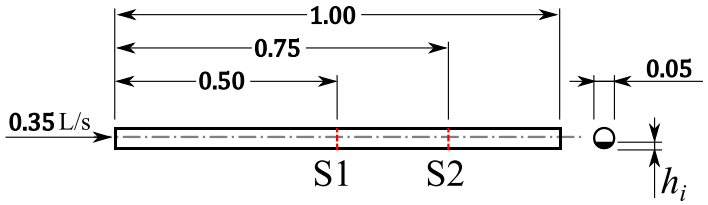

Source: the author.

The fluid density and viscosity were adopted as 1000 kg/m³ and 10^{-6} m²/s, respectively. The Reynolds number for $h_i/D = 1.0, 0.5, 0.25$ are $Re = 9 \times 10^3, 1.8 \times 10^4, 2.7 \times 10^4$, respectively. Reynolds number is given by $Re = 4R_h U/\nu$, where the hydraulic radius is $R_h = A/P_w$, A is the flow cross-sectional area, P_w is the wetted perimeter and U is the inflow velocity.

The numerical parameters adopted in the particle wall and polygon wall modeling are given in Table 4 and Table 5, respectively. Three particle distances (l_0) were simulated, $0.005, 0.002$ and 0.001 m, representing the resolutions $D/l_0 = 10, 25, 50$.

The simulations were performed on the same machine which is equipped with Intel© Xeon© Processors E5-2680 v2 (10 cores, 2.8 GHz and 128 GB of memory each).

Table 4 – Particle wall modeling: numerical parameters, approximate number of particles and computational cost.

Distance between particles (l_0) [mm]	5	2	1
Resolution (D/l_0)	10	25	50
Initial number of particles	31908	164424	643836
Final number of particles	43155	321249	1831708
Time step [ms]	0.2	0.1	0.05
Computational time [hr]	1.6	42.3	1111.1
Relaxation coefficient γ_1	0.0016	0.0025	0.0025
Relaxation coefficient γ_2	0.04	0.05	0.05
Compressibility coefficient α [ms²/kg]	10^{-8}	10^{-8}	10^{-8}

Source: the author.

Table 5 – Polygon wall modeling: numerical parameters, approximate number of particles and computational cost.

Distance between particles (l_0) [mm]	5	2	1
Resolution (D/l_0)	10	25	50
Initial number of particles	552	2268	7368
Final number of particles	6203	105530	834817
Time step [ms]	0.2	0.1	0.05
Computational time [hr]	1.2	35.7	1090.6
Relaxation coefficient γ_1	0.0016	0.0025	0.0025
Relaxation coefficient γ_2	0.04	0.05	0.05
Compressibility coefficient α [ms²/kg]	10^{-8}	10^{-8}	10^{-8}
Repulsive coefficient (α_{rep}) [N/m²]	10^6	10^6	10^6

Source: the author.

3.2.2 Results and discussions

The snapshots of the simulations using both boundary modeling for the inflows $h_i/D = 1.00, 0.50$ and 0.25, at $t = 10$ s, are presented in Figure 16, Figure 17 and Figure 18, respectively. The colors are related to fluid velocity magnitude.

Figure 16 – Snapshots of the simulations with particle (a) and polygon (b) wall modeling and inflow $h_i/D = 1.00$ at $t = 10$ s. Resolutions $D/l_0 = 10$ (top), 25 (middle) and 50 (bottom).

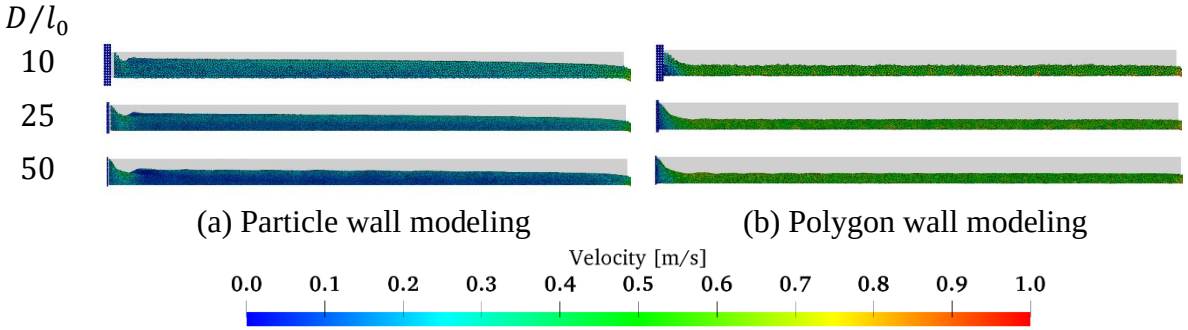

Source: the author.

Figure 16 shows that the water surface levels computed by using the particle wall modeling are higher than those obtained using the polygon wall modeling for the inflow relation $h_i/D = 1.00$. Moreover, the flow velocities computed using the particle wall modeling are lower than those calculated by the polygon wall modeling.

For the simulations with inflow $h_i/D = 0.50$, see Figure 17, results similar to those presented in Figure 16 are obtained. The snapshots show that, along the pipe, the water surface levels computed using the particle wall modeling decrease significantly while the water surface levels computed by using polygon wall remain almost constant.

Figure 17 – Snapshots of the simulations with particle (a) and polygon (b) wall modeling and inflow $h_i/D = 0.50$ at $t = 10$ s. Resolutions $D/l_0 = 10$ (top), 25 (middle) and 50 (bottom).

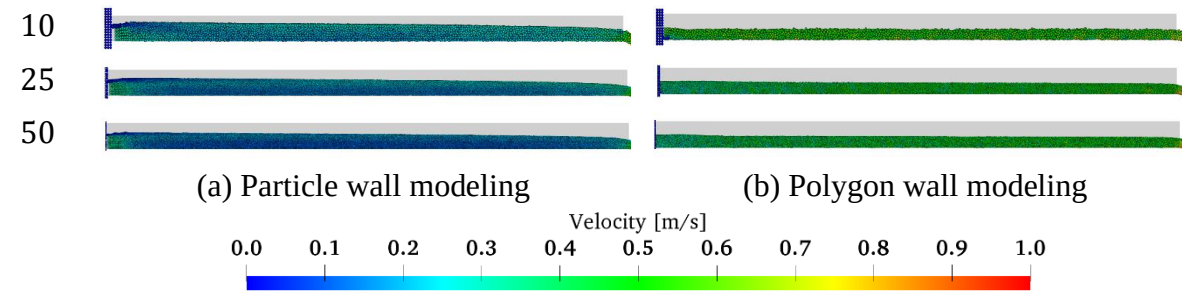

Source: the author.

Figure 18 shows the snapshots for the inflow $h_i/D = 0.25$. Similar to the previous cases, the water surface levels computed using the particle wall and polygon wall modeling are different, and much higher flow velocities associated to significantly lower water surface level occur when polygon wall modeling is adopted. Furthermore, hydraulic jump is formed in the simulations with the particle wall modeling, while the simulations using polygon wall modeling present a smooth free-surface profile independent of the model resolution.

Figure 18 – Snapshots of the simulations with particle (a) and polygon (b) wall modeling and inflow $h_i/D = 0.25$ at $t = 10$ s. Resolutions $D/l_0 = 10$ (top), 25 (middle) and 50 (bottom).

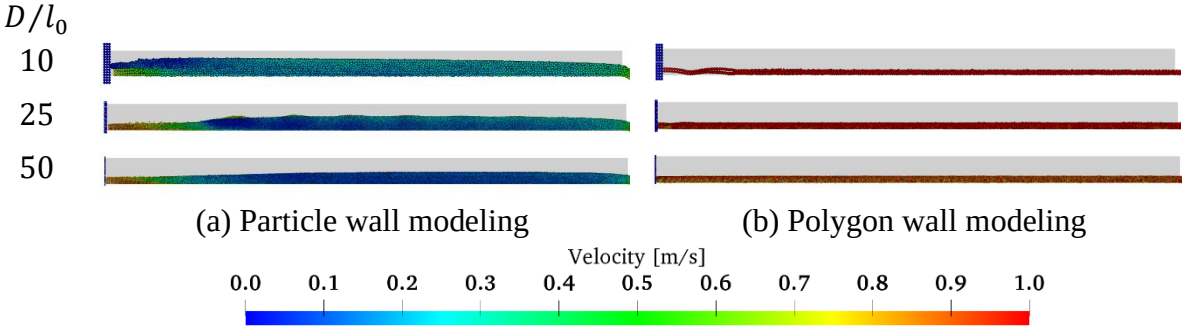

(a) Particle wall modeling (b) Polygon wall modeling

Source: the author.

Figure 19, Figure 20 and Figure 21 give the pipe filling computed at the sections S1 and S2 by using both boundary modeling for the inflow heights $h_i/D = 1.00$, 0.50 and 0.25, respectively.

Figure 19 shows that, regardless of the model resolution, the flow reaches the sections S1 and S2 at the same instant for the simulations with the polygon wall modeling for $h_i/D = 1.00$. On the other hand, when the particle wall modeling is adopted, there are small delays depending on the model resolution, and coarse resolution models lead to higher delays. When the numerical solutions reach the steady state, the height of water surface levels are almost the same for all cases with polygons, regardless of the model resolution, while lower resolution models result in a higher water surface level for the particle wall modeling.

Figure 19 – Time series of pipe filling at section S1 (a) and S2 (b) using both wall modeling and inflow height of $h_i/D = 1.00$.

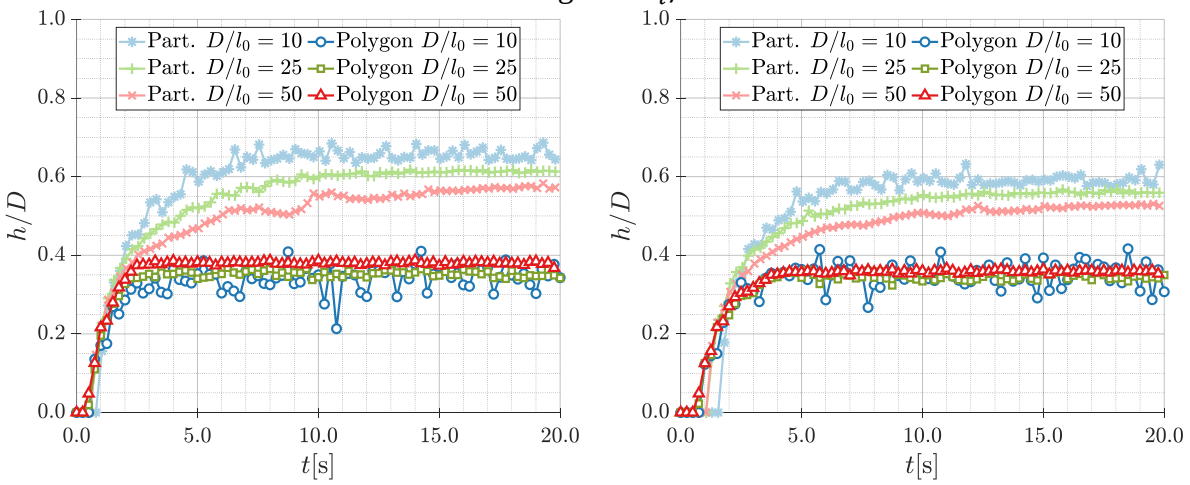

(a) Section S1 (b) Section S2

Source: the author.

For the cases with $h_i/D = 0.50$, see Figure 20, once again, regardless of the resolution, the flow reaches the sections S1 and S2 at the same instant when the polygon wall modeling is adopted. Larger delays of the lower resolution particle wall modeling are also computed. Although the steady water levels computed using polygons wall modeling with different resolutions are slightly different, good convergence is obtained. For the simulations adopting only particles, the increase of the resolution leads to a decrease of the height of the water surface level and the convergence is not achieved.

Figure 20 – Time series of pipe filling at section S1 (a) and S2 (b) using both wall modeling and inflow height $h_i/D = 0.50$.

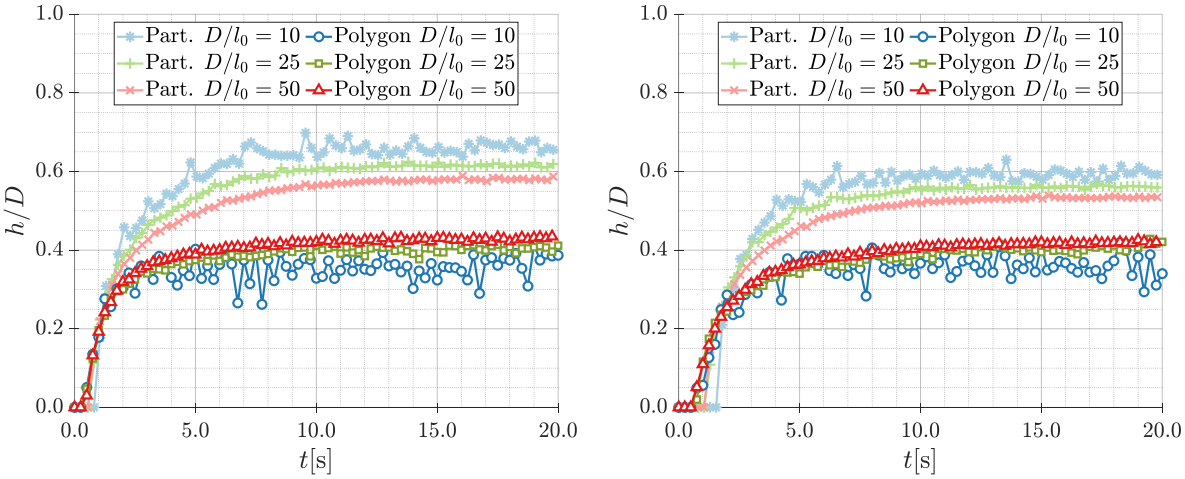

(a) Section S1 (b) Section S2

Source: the author.

Figure 21 illustrates the computed results for $h_i/D = 0.25$. As in the previous results, the polygon wall modeling results in almost the same instants when the flow reaches the sections S1 and S2, but delays occur in the results of the simulations with lower resolution of particle wall modeling. The delays computed by using particle wall modeling reveal that the accuracy of this approach is highly dependent to the resolution. This is because the non-uniform particle representation of the smooth inner pipe wall surface results in an unphysical frictional loss of the fluid flow. Moreover, since the convergence is not reached in particle wall modeling, the simulated cases require a finer resolution, which demands much larger computational resources. It is important to point out that these issues are fixed by the adoption of polygon walls, which more accurately reproduces the boundary condition.

Figure 21 – Time series of pipe filling at section S1 (a) and S2 (b) using both wall modeling and inflow height $h_i/D = 0.25$.

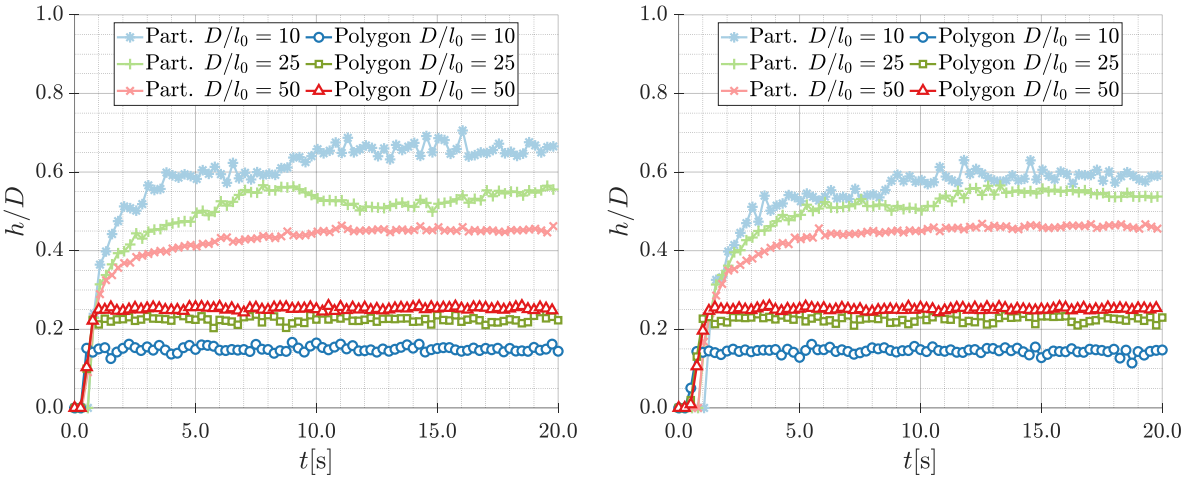

(a) Section S1 (b) Section S2

Source: the author.

The mean pipe filling computed at S1 and S2 after 10 s for both boundary modeling and three inflow heights are illustrated in Figure 22 as a function of the model resolution.

Regardless of the resolution, the mean water surface levels at S1 and S2 computed using polygon wall modeling are very close, with the level at S2 slightly higher than at S1. This provides relatively consistent results and indicates a small reduction of flow velocities associated to small energy loss between two sections of the pipe. In addition to this, mean water levels are almost independent of the resolution for the inflow $h_i/D = 1.00$. For the inflows $h_i/D = 0.50$ and 0.25, the convergence is achieved when the resolution D/l_0 is higher than 25.

In case of particle wall modeling, due the non-smooth particle wall representation of the smooth inner pipe wall, the mean water levels computed at S1 are significantly higher than those computed at S2, except for higher resolution models for the inflow $h_i/D = 0.25$.

Figure 22 – Mean pipe filling after 10 s in sections S1 and S2 as a function of resolution for both wall modeling and inflow heights: $h_i/D = 1.00$ (a), $h_i/D = 0.50$ (b), $h_i/D = 0.25$ (c).

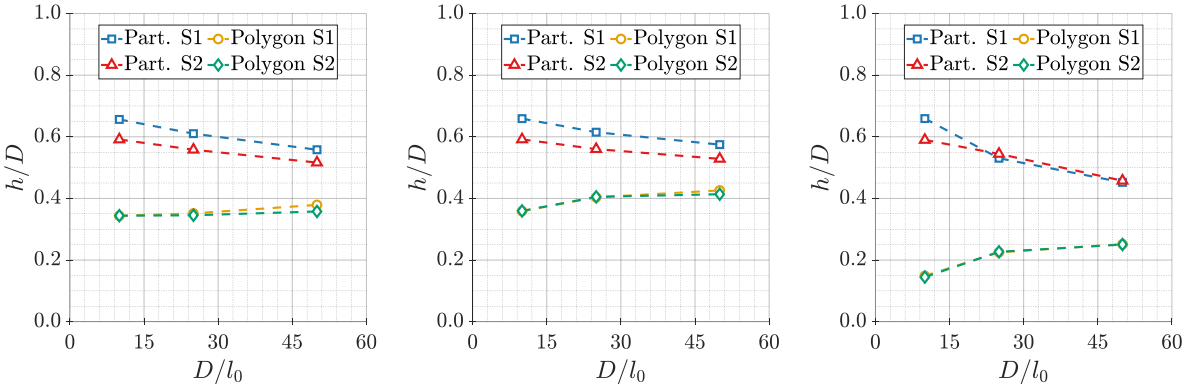

(a) $h_i/D = 1.00$ (b) $h_i/D = 0.50$ (c) $h_i/D = 0.25$

Source: the author.

The mean water surface levels at S1 and S2 computed using particle wall modeling are much higher than those obtained using polygon wall modeling. These results show relatively large unnatural energy losses caused by particle wall modeling that lead to much lower flow velocity and higher water surface levels at same flow rate.

4 EXPERIMENTAL AND NUMERICAL ANALYSIS OF SEDIMENTS REMOVAL OF DOUBLE BOTTOM BALLAST TANKS

The global trade is predominantly transported by ships, which in 2017 represented 80% of the world trade (GEF-UNDP-IMO GloBallast Partnerships Programme, 2017). In the same year, the total volume transported by ships reached 10.7 billion tons (UNCTD, 2019). The growth of the global economy reflects in the expansion of the world seaborne trade, the annual grow until 2023 is estimated in 3.8% (Hoffman et al., 2018). The increase of the importance of the maritime transport in the global economy also strength the concerns about its collateral effects on the environment.

Concerning safety and stability, when ships are travelling with low or without cargo, ballast water is used, and seawater is the most often choice. Small organisms are introduced during the ballasting operation and might survive long journeys, as larvae and spores. Depending upon the environmental conditions where they are discharged can represent a threat for the local biodiversity. It is estimated that 10 billion tons of ballast water is carried around the world per year and up to 7 thousand species are transferred in ballast water every hour of everyday (GEF-UNDP-IMO GloBallast Partnerships Programme, 2017).

The transport of invasive species impacts not only the coastal and marine environments, but also fisheries production, aquaculture, coastal infrastructure, tourism industry and human health (Pereira et al., 2016, 2014; Pereira and Brinati, 2012). In order to reduce the potential impact of invasive species transported inside ballast tanks, the International Maritime Organization (IMO) required the exchange of at least 95% of the ballast water volume in regions at least 200 nautical miles far from the coast and 200 m in depth, where the invasive species have little chance to survive. One of the proposed ballast water exchange method is the flow-through method, in which pumping water three times the tank volume shall be performed (International Maritime Organization, 2004).

Regarding the investigation of the efficiency of the ballast water exchange, several studies were reported in the literature, specially focusing on the analysis of the ballast water exchange procedure, ballast tank geometry and water density difference in the flow-through process. Arai et al., (2002) analyzed numerically the sloshing in ballast tanks during ballast water exchange. Kamada et al., (2005), applied the MPS method to verify the flow-through efficiency with fluids of same density. Wilson et al., (2006), using experimental and computational approaches concluded that the perfect mixing assumptions are not valid for some real tank geometries and three volume ballast water exchange criteria might not meet the

standards. Prange and Pereira, (2013); Qi and Eames, (2015), also investigated the influence of some tank geometries and concluded that structural changes in hopper and upper wing tank could significantly increase the exchange efficiency. Some studies focused on the analysis of the effect of the difference of the densities between the fluid inside the tank and the inflow fluid showing that the exchange efficiency could be compromised due confinement of water in the bottom or top of the tank (Chang III et al., 2009; Eames et al., 2008). Yuan et al. (2017) proposed a system of ballast water circulation, in which the sediment is suspended by water injection and separated using a hydrocyclone. Recent contribution of Güney et al. (2020) investigated the influence of minor structural changes and injection of air on the sediment removal process of the double bottom ballast tank. However, for the author's knowledge, study on the sediment removal process during the ballast water exchange is still incipient.

The sediments inside ballast tanks can be divided in four categories: soil, organic material, parts of the tank and heavy metals (Maglić et al., 2016). The soil material ranges from clays to sands, and the larger particles are introduced to the tanks when ballast water is collected too close to sea bottom. The organic material is relatively small in the composition and is partially formed by organisms that not survived long voyages. The parts of the tank consist of fragments of the protective coating due to corrosion and ballasting processes. Heavy metals might be present specially when the ballast operations occur frequently in areas polluted by industrial wastes. Maglić et al., (2019), have reported that the density of sediment deposited in ballast tanks varies between 1200 kg/m³ and 2000 kg/m³. Several studies reported the presence of significant amount of sedimented material inside ballast tanks (Prange and Pereira, 2013). Measurements made during maintenance processes, like dry docking, showed that up 200 tons of sediments can be found and more than 68% of the ships in EUA and Canada between 2000 and 2002 carries residues (Johengen et al., 2005).

The deposition of sediments in bottom of ballast tanks could compromise the economic efficiency of the ship. Beside the obstruction of the suction bell and scallops, which might impair the ballast water pumping, the sediments accumulated in ballast tanks might also be a habitat for invasive species, reducing the effectiveness of the ballast water exchange and degrading the ballast water (Prange and Pereira, 2013).

Within this context, the objective of the present study is to investigate experimentally and numerically the process of sediment removal from ballast tanks during the flow-through ballast water exchange. Aiming a comprehensive study, two-dimensional (2D) reduced-scale models of one compartment of a double bottom ballast tank were adopted for both experimental and numerical approaches. The main features of the tank, such as inlet, outlet and stiffeners

were reproduced. For this purpose, numerical simulations were performed using a particle-based method, which is extremely flexible to model complex geometries. However, for sake of simplicity, simplified modeling of the rheological behaviors of the sediments were done by representing them as granular materials in the physical experiments and modeling them as denser fluids in the numerical simulations. The effects of the flow rate and the density of the sediments were also considered. In addition to this, the effectiveness of flow deflection devices and injection of water from the bottom of the tank on improving the effectiveness of the removal of sediments were also evaluated. The water injection from the tank bottom is based on idea proposed by Prange and Pereira (2013).

This chapter is organized in 6 subsections. The experimental apparatus and model, the manometers calibration and the dimensionless parameters are presented in the subsection 1. The studied cases are presented in subsection 2. The numerical model validation is presented in subsection 3. The results are presented and analyzed in subsection 4.

4.1 EXPERIMENTAL APPROACH

Ballast tanks of vessels are generally spaces located between hull plates and cargo holds. Depending on the vessel type, the ballast tanks might belong to three main categories: collision tanks, side tanks and double bottom tanks. Collision tanks are in the fore and aft peaks, side tanks are vertical tanks located between cargo holds and the side shells and double bottom tanks are between cargo holds and bottom shell plating of the hull. Figure 23 shows a schema of the different types of ballast tanks and their positions inside a ship.

Figure 23 – Schematic of different types of ballast tanks.

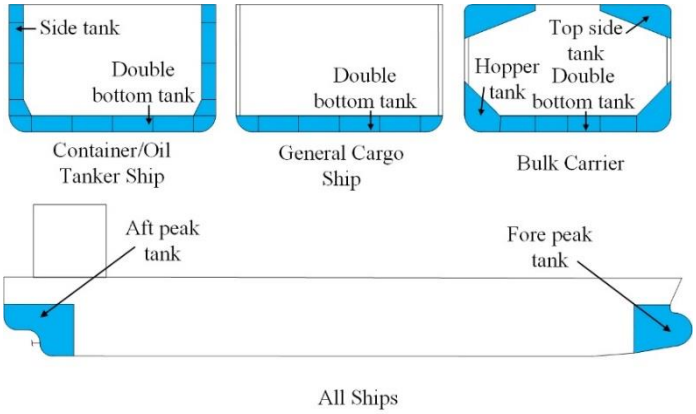

Source: the author.

The different tank geometries and locations provide different conditions for sediment removal during ballasting. The tapered geometry of the collision tanks facilitates drainage of the sediments toward the bottom of the tank. On the other hand, huge internal volume with small bottom area of side tanks also enables easier cleaning of the sediments. In the case of the double bottom tanks, the combination of relatively large bottom area, low ceiling height and presence of structural stiffeners, mainly under the tank ceiling and on the tank bottom, results in a geometry that disfavor the sediment removal.

In this way, the focus of the present study is on the sediment removal in the double bottom tanks. The present study is divided in two parts:

the first part aims to evaluate the sediment removal efficiency of the flow thought process inside a typical double bottom ballast tank, where the inflow and the outflow from the opposite sidewalls are in level and structural stiffeners are placed transversally to the flow under the tank ceiling and on the tank bottom;

the second part of the study consists of investigation of the effectiveness of two measures aiming to improve the sediment removal process:

- a flow deflector in the center of the double bottom ballast tank with an adjustable angle θ to direct the flow to the bottom and enhance the perturbation of the sediments;
- injection of ballast water from tank bottom to directly remove the sediments.

4.1.1 Experimental apparatus

The experimental apparatus to reproduce the flow through process in a ballast tank occupies two floors of the experimental facility. In the upper floor, there are four water storage tanks of 0.5 m^3 each, that are used to supply water during the experimental tests. The storage tanks are connected by horizontal pipes forming two branches A and B with two tanks each and both branches are connected to a vertical drain. In each branch, a sudden expansion of pipe section is introduced to provoke minor head loss, aiming to measure the flow rate during the tests, liquid-column gauges are installed before and after the sudden expansions of pipe section. The minor head loss leads to fluid level difference in the manometers tubes, which is used to determine the flow rate as detailed in the subsection 4.1.4. The expansions and manometer tubes of the branches are installed near the midpoint of the pipe that connects the branches to vertical drain as showed in Figure 24. The dimensions of the pipes are shown as well. In the figure, M_{A1}

denotes the position of the tube 1 of the manometer A associated to the branch, and similarly for $M_{A2,}$ M_{B1} and M_{B2}.

Figure 24 – Top view of the upper floor (a) and photo of the pipes connecting the water tanks showing the four storage tanks, the piping of the water supply and the manometers (b).

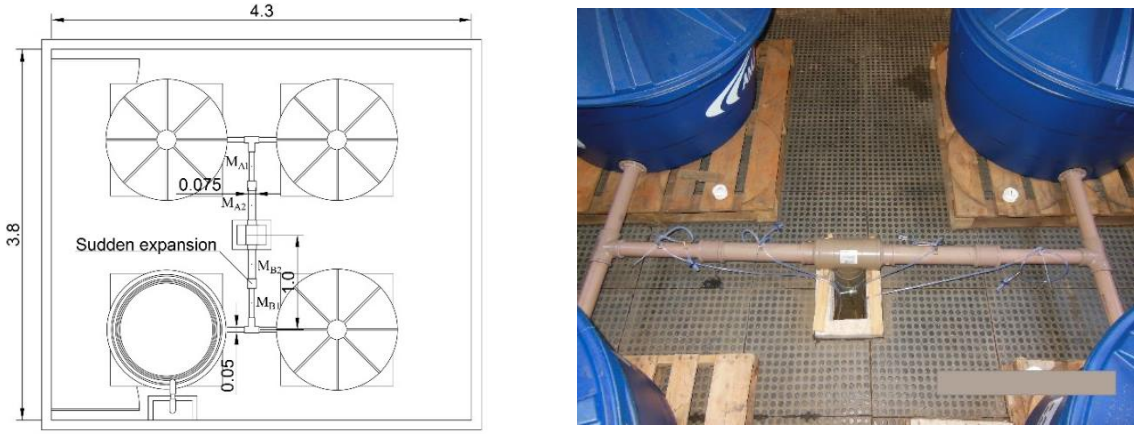

(a) (b)

Source: the author.

The vertical drain consists of an extensible pipe that enables the connection with experimental model in two different ballast water inlet positions, from side wall or from bottom, as showed in Figure 25 (a). The gate valve located in the vertical drain is used to retain the water flow before and after the tests and control the flow rate during the experiments. In the lower floor, the outlet of the model is connected to the discharge water tanks through a discharge pipe, showed in Figure 25 (b). The discharge pipe has an inverted U shape with highest section higher than the tank ceiling to assure that the model is always full of water during the tests. A square wire net is placed at the outlet of the discharge pipe to filter the sediment material from the discharged water. The panel of manometers, showed in Figure 25 (c), is recorded during the experiments in order to measure the water surface level inside the tubes and calculate the flow rate.

Figure 25 – Photos of the extensible vertical drain and gate valve (a), inverted U shape discharge pipe (b) and panel of manometers (c).

(a) (b) (c)

Source: the author.

Figure 26 presents the front view of the experimental apparatus and a photo of the experimental model connected to the vertical drain and to the discharge pipe. In the experiments, the fluid flows from the upper tanks to the experimental model under the pressure of hydraulic head, especially the elevation head. The elevation between water level in the upper tank and the top of the experimental model ranges from 1.3 m to 1.7 m to cover the desirable flow rates.

Figure 26 – Front view of the experimental apparatus (a) and photo of the experimental model connected to the vertical drain and discharge pipe (b).

(a) (b)

Source: the author.

The discharge water tanks, that consist of four water tanks of 0.5 m³ each, are used to store the water discharged during experiments. A recirculation water pump is used to pump the

water to the water storage tanks of the upper floor for reuse in the experiments. Figure 27 gives the top view of lower floor and photos of the recirculation pump and recirculation outlet.

Figure 27 – Top view of the lower floor (a), photos of the water recirculation pump (b) and recirculation outlet (c).

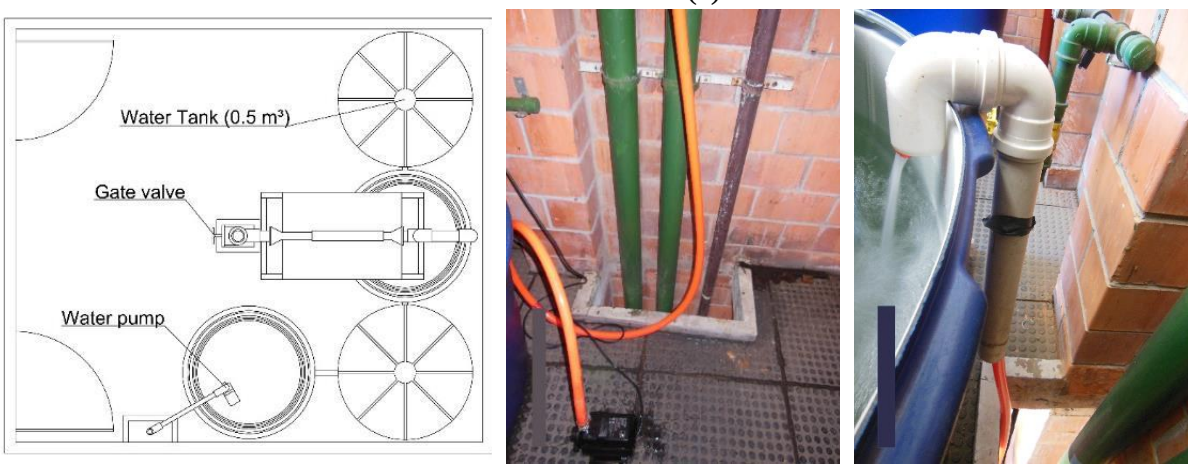

(a) (b) (c)

Source: the author.

Figure 28 shows a perspective view of the experimental apparatus, in which one tank of branch B is no shown for visualization of the horizontal pipe. The experiments were recorded using a camera Sony DSC-HX9V with a frame rate of 29.97 frames/second and resolution of 1440 x 1080.

Figure 28 – Perspective view of the experimental apparatus.

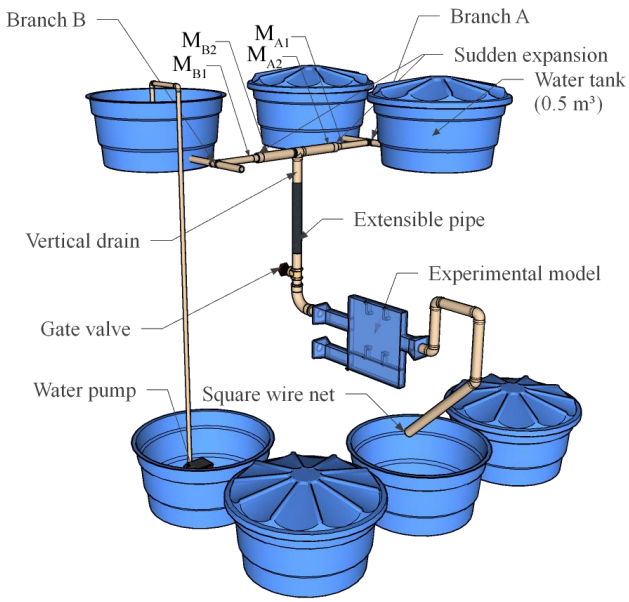

4.1.2 Experimental models

The experimental model was designed to represent a compartment of double bottom ballast tank in 1:4 reduced scale, considering the usual dimensions of a real tank. As mentioned before, double bottom tanks are considered in the present study because in such ballast tanks the deposition and removal of the sediments are more critical. For sake of simplicity, 2D model are considered in the present study.

Figure 29 provides the exploded view of the model tank that shows its internal components such as additional front and rear plates with notches and circular holes to fix the stiffeners and a flow deflector, respectively. The configuration with internal flow deflector aims to evaluate the effectiveness of the large flow perturbation on the sediment removal. In addition to this, the tank ceiling is removable to place the sediment material, as well as to replace the false bottom of the tank by one with openings that allows inflow from the bottom. In this way, a resistant tank with very flexible internal configuration, which enables easy change of model tank configuration to perform the desirable studies, is obtained.

Figure 29 – Exploded view of the reduced-scale model tank.

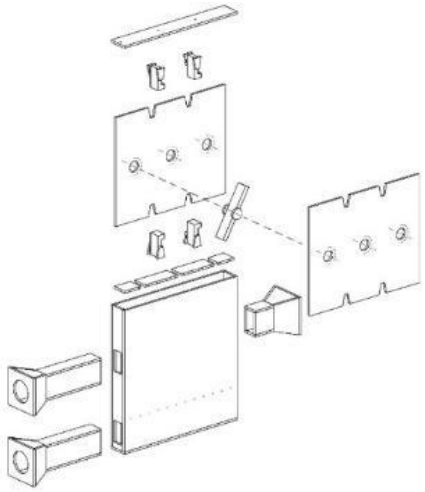

Source: the author.

Figure 30 shows front and side views of the experimental model. The main geometrical features of a section centered in the manholes of a typical double bottom ballast water tank compartment, such as the stiffeners under the ceiling and on the bottom, are reproduced. However, as a 2D model, the effects of the difference between the widths of the tank and the manhole are neglected. The main dimensions of the model tank are also provided in Figure 30. The inner dimension of the model tank is 0.6 m length, 0.5 m height and 0.05 m width.

Figure 30 – Front and side views of the reduced-scale model tank and its main dimensions.

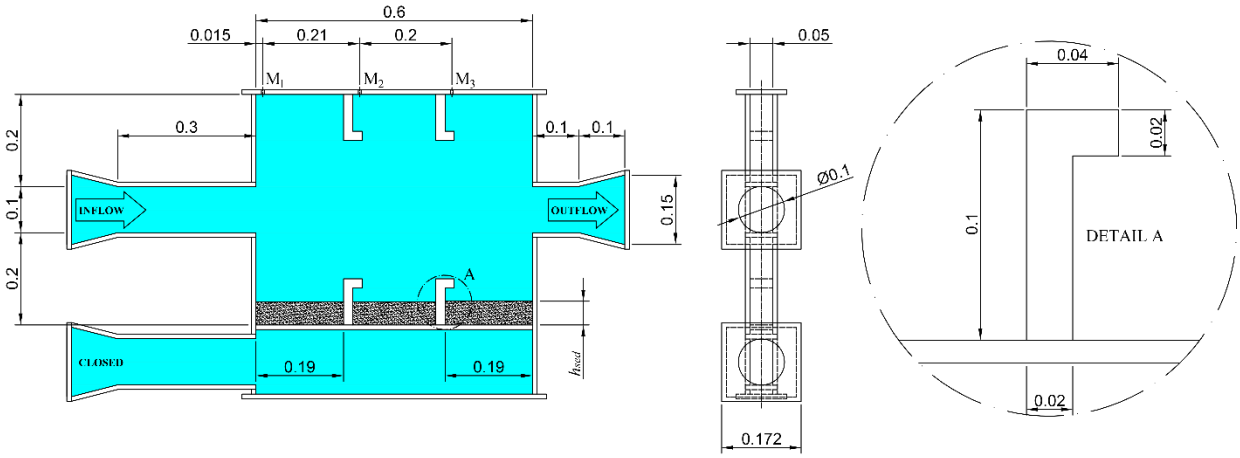

Source: the author.

The model tank was designed to be a versatile device to investigate the sediments removal considering different tank configurations. Figure 30 shows that the model tank has two intakes. The upper one is used to investigate the sediments removal process in a typical double bottom tank. The lower one is used to direct the inflow through the tank bottom to investigate the effectiveness of the flow injection from the bottom.

The model configuration used in the first part of the experiments, in which the sediments removal process of a typical double bottom tank is investigated, is also shown in Figure 30, where the grey color represents the sediment, and ‘inflow’, ‘outflow’ and ‘closed’ shows the circuit of the water flow. The parameter h_{sed} indicates the height of the sediment, and a solid plate is used as false bottom.

In the second part of the experiment, two modifications aiming improve the sediment removal process were investigated. The first one is the introduction of a deflector in the center of the tank with an adjustable angle θ. The deflector has the same width of the tank (0.05 m), length of 0.25 m and height of 0.02 m. The adjustable angle θ enable to analyze the effects of the orientation of the deflector to the main flow on the sediment removal process. The inlet and outlet are also in level. Figure 31 presents a front view of the experimental model with the addition of a deflector.

Figure 31 – Front view of the model tank configuration used in the experiment with flow deflection.

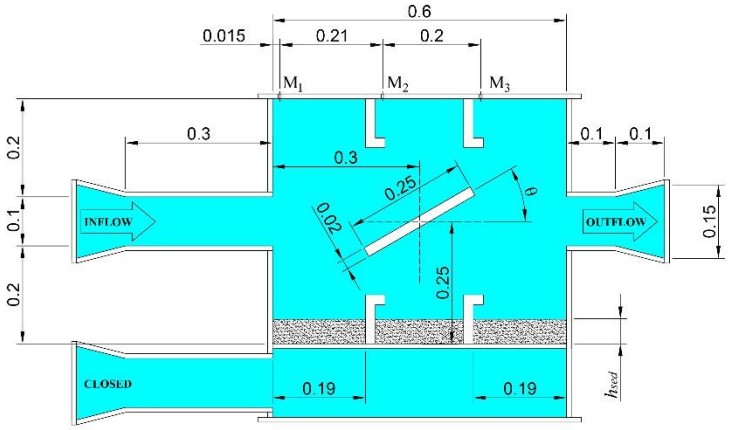

Source: the author.

The second modification investigated is the injection of water from bottom, instead the inlet and outlet in level used in the two formers configurations. For water injection from bottom, the false bottom acrylic plate, where the sediment is placed on, presents three openings 0.025 m in length and 0.05 m in width. The upper intake is closed, and the vertical drain is extended to connect the lower intake of the model tank, which head off the inflow through the false bottom. 0.5 mm squared meshes are positioned in the bottom openings to avoid the sediment flow down through the opening. Figure 32 presents a front view of the experimental model with the injection of water from bottom.

Figure 32 – Front view of the model tank configuration used in the experiment of the inlet from the bottom.

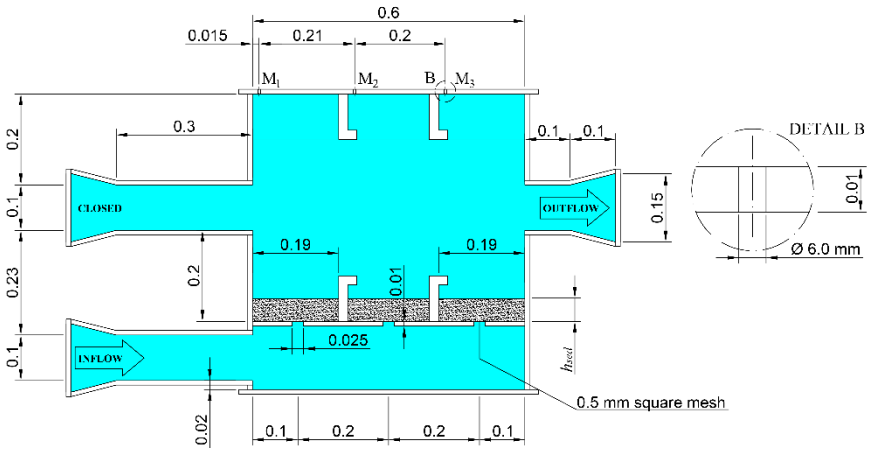

Source: the author.

The components of the reduced-scale model tank are presented in Figure 33. The notches and circular holes of the front and rear plates are used to fix the stiffeners and the flow

deflector. The inlet/outlet connectors connect the vertical drain and the discharge pipe to the tank. Except the stiffeners, the model tank is made from acrylic plates of 0.01 m thickness.

Figure 33 – Photo of the front and rear plates (a), inlet/outlet connector (b), stiffener (c) and flow deflector (d) of the reduced-scale model tank.

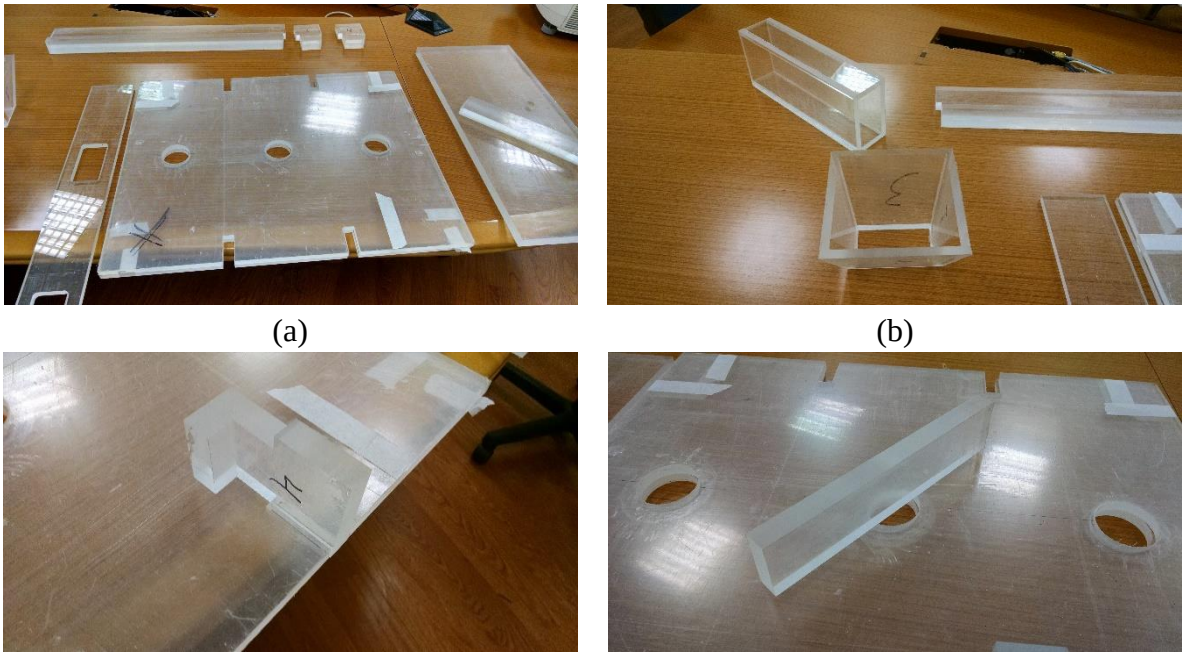

(a) (b)

(c) (d)

Source: the author.

Figure 34 provide details of the reduced-scale model tank. The inlet and the outlet are connected to the vertical drain and discharge pipe, respectively, as showed in Figure 34 (a) and Figure 34 (b). Figure 34 (c) exhibits the flow deflector, which is fixed using the circular hole. To ensure the correct measurements of the three manometers located in the tank ceiling, it is important to remove air bubbles inside the tank. For this purpose, drains are installed on the tank ceiling to remove air bubbles before each experiment, as showed in Figure 34 (d).

Figure 34 – Photo of the inlet (a), outlet (b), fixed flow deflector (c) and drains installed on the tank ceiling (d) of the reduced-scale model tank.

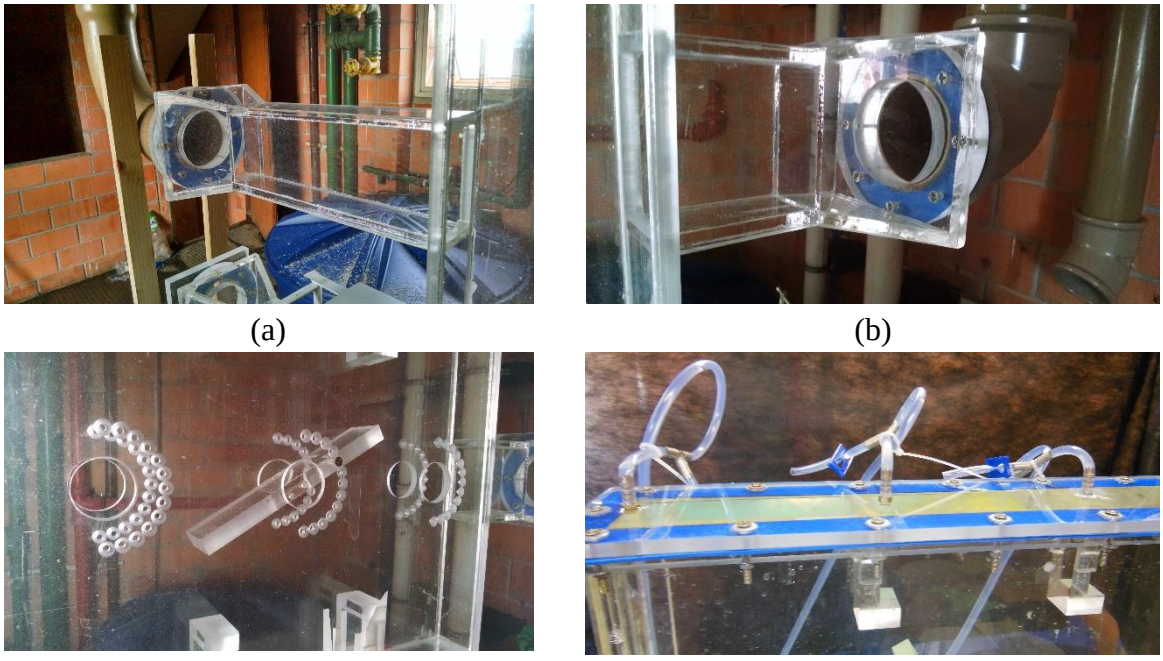

(a) (b)

(c) (d)

Source: the author.

4.1.3 Sediment material

In the experiment, two materials were used to investigate the effects of different aspects of the sediment: a plastic and a glass. Figure 35 shows photos from both sediment materials used in the experiments. The plastic and the glass material colors are yellow and orange, respectively.

Figure 35 – Sediment material used in the experiment: plastic (a) and glass (b).

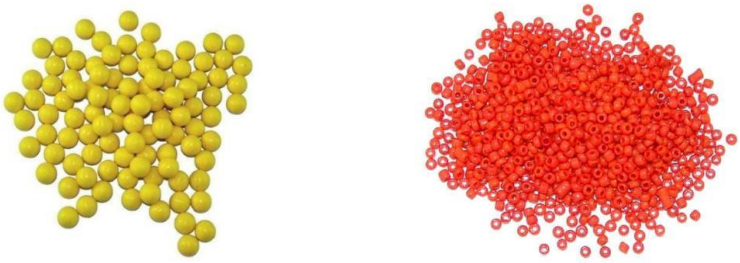

(a) (b)

Source: the author.

Table 6 shows the characteristics of the sediment used in the experiments. The plastic material is made of acrylonitrile butadiene styrene (ABS), its surface is very smooth, and it has a very accurate spherical format with 5 mm in diameter. The glass material has a torus shape

with approximately 2 mm external diameter, 1 mm internal diameter and 1 mm in height, its surface is also very smooth.

Table 6 – Characteristics of material used as sediment.

Material	Shape	External diameter [mm]	Density [kg/m³]
Plastic	Spherical	5	1020
Glass	Torus	2	1700

Source: the author.

Before each experiment, the model tank ceiling is opened , and the sediment material is placed on the bottom of the tank with a height of $h_{sed} = 10$ cm.

4.1.4 Manometers calibration

The sudden expansion of the pipe in the upper floor were designed to measure indirectly the flow rate during the tests. The tubes of the manometer are connected with each other forming a U-shape tube, in which the difference in the pressures acting in the two points, before and after the minor head loss, leads to different water levels. The different liquid levels can be related with the flow velocity as follows:

$$\Delta h = k\frac{u^2}{2g} \tag{36}$$

where Δh is the water level difference between the connected tubes, v is the scalar downstream flow velocity, g is the gravity and k is the kinetic energy factor of the piping component, which must be experimentally determined for each sudden expansion.

From the measurement of the minor head loss, the flow velocity and flow rate can be calculated. The calibration of the kinetic energy factor k was carried out by measuring the time to fill a bucket (22.45 L in volume) and the water level difference in manometers A and B considering several gate valve openings. The kinetic energy factor adopted is the mean of all measurements for each manometer, $k_A = 0.968$ and $k_B = 1.676$ for manometers A and B, respectively. Figure 36 presents the experimental measurements, the trend line of experimental points and the curve using the mean calculated k. The good agreement between the trend line and the theoretical shows the accuracy of the applied method.

Figure 36 – Calibration curve for manometer A (a) and manometer B (b).

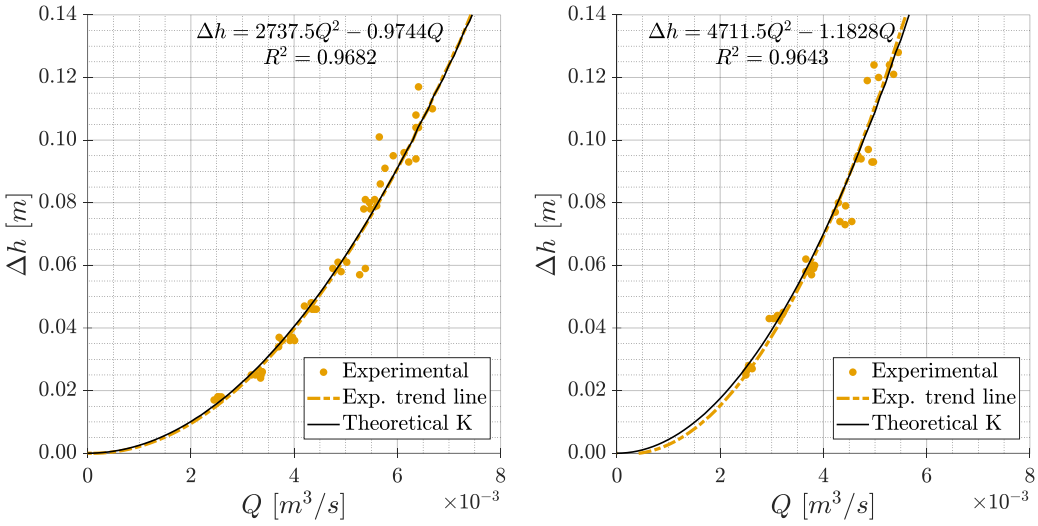

Source: the author.

The flow rate of each experimental test consists of the sum of the flow rate measured by the manometers A and B.

4.2 CASES OF STUDY

The studied cases were chosen aiming to investigate the influence of the most important variables, the flow velocity and sediment density, on the process of the sediment removal. In addition, the flow deflector angle and inflow direction were also investigated in the second part of the present study.

The gate valve opening was used to control the flow during the experiments. For each tank model and deflector angle, two gate valve openings were experimented, to be specific 1.5 and 2.5 turns of valve handle, resulting in different flow rates levels. In case of 1.5 turns of valve handle the flow rate ranges from 1.3×10^{-3} m³/s to 2.3×10^{-3} m³/s and in case of 2.5 turns ranges from 2.5×10^{-3} m³/s to 5.2×10^{-3} m³/s. The fluid used in experiments was water with density of 1000 kg/m³ and kinematic viscosity of 10^{-6} m²/s.

Three deflector angles were chosen: positive and negative attack angles and perpendicular to the flow, corresponding to $\theta = 30°$, 120° and 90°, respectively. The deflector angle follows the convention established in Figure 31.

4.2.1 Nomenclature

The nomenclature adopted in the present study for the cases without deflector follows the pattern [*tank model*]-[*material and number of turns of valve handle*] and for the cases with deflector [*tank model*]-[*deflector angle*]-[*material and number of turns of valve handle*]. Table 7 shows the abbreviations of characteristics of the studied cases. For example: SD-A030-P15 denotes the case with inlet from side wall, deflector angle of 30°, plastic as sediment and gate valve opening of 1.5 turns.

Table 7 – Nomenclature of the studied cases.

Tank model	Inflow from side wall and without deflector	SW
	Inflow from side wall and with deflector	SD
	Inflow from bottom and without deflector	BW
Deflector angle	$\theta = 30°$	A030
	$\theta = 90°$	A090
	$\theta = 120°$	A120
Material and gate valve opening	Plastic and 1.5 turns of valve handle (approx. 0.5 m/s)	P15
	Plastic and 2.5 turns of valve handle (approx. 1.0 m/s)	P25
	Glass and 1.5 turns of valve handle (approx. 0.5 m/s)	G15
	Glass and 2.5 turns of valve handle (approx. 1.0 m/s)	G25

Source: the author.

4.2.2 Transient period and experiments duration

During transient period immediately after the opening of the gate valve, the fluid accelerates until reaches steady state. The duration of the period is not negligible and can be measured based on the time that the water level inside the manometers takes to stabilize. Table 8 shows the measured velocity and the duration of the transient period for the cases investigated in this study. The values of velocity and transient period are used as input in the numerical simulations. The duration of the experiments and simulations are the transient period plus the time to steadily flow three times the model tank volume.

Table 8 – Measured flow rate, duration of transient period and total duration for each case.

Case	Flow rate [$\mathbf{10^{-3}}$ m³/s]	Velocity [m/s]	Duration of the transient period [s]	Time to flow three times the tank volume [s]
SW-P15	1.9	0.4	6.0	29.47
SW-P25	4.9	1.0	8.0	17.17
SW-G15	2.2	0.4	5.0	25.85
SW-G25	5.2	1.0	7.0	15.69
SD-A030-P15	2.0	0.4	6.0	28.00
SD-A030-P25	4.7	0.9	6.0	15.66
SD-A030-G15	2.5	0.5	6.0	23.84
SD-A030-G25	5.2	1.0	11.0	19.61
SD-A090-P15	2.0	0.4	6.0	28.98
SD-A090-P25	4.4	0.9	8.0	18.14
SD-A090-G15	1.1	0.2	6.0	48.10
SD-A090-G25	4.3	0.9	12.0	22.56
SD-A120-P15	2.3	0.5	4.0	23.34
SD-A120-P25	5.1	1.0	7.0	15.81
SD-A120-G15	2.3	0.5	6.0	25.34
SD-A120-G25	4.6	0.9	14.0	23.74
BW-P15	1.3	0.3	8.0	42.49
BW-P25	3.8	0.8	13.0	24.91
BW-G15	1.0	0.2	6.0	53.07
BW-G25	2.5	0.5	6.0	24.18

Source: the author.

4.2.3 Characteristics flow in a ballast tank

The flow in a ballast tank is characterized by two dimensionless variables: Reynolds number (Re) and Richardson number (Ri): The Reynolds number is a ratio of inertial forces to viscous forces within a fluid subject to movement and is defined as follows:

$$Re = \frac{uL}{\nu} \tag{37}$$

where u is the characteristic scalar velocity of the flow, L is a characteristic linear dimension, ν is the kinematic viscosity of the fluid. At low Reynolds numbers viscous forces are dominant and laminar flow occurs, which is characterized by smooth fluid motion. At high Reynolds numbers inertial forces are dominant and turbulent flow occurs, which is characterized by vortices and instabilities. The Reynolds similarity allows to ensure that the scaled model and its full-size version have the same flow regimes.

The Richardson number is a ratio of the buoyancy force to the flow shear force and is calculated as follows:

$$Ri = \frac{\Delta\rho g L}{\rho u^2} \tag{38}$$

where $\Delta\rho$ is the density difference between the incoming fluid and the fluid of the tank and ρ is the density of the denser fluid. When the density difference between fluids is very small or the flow velocity is very high, $Ri \to 0$, when denser fluid is injected in the tank Ri is positive and when lighter fluid is injected in the tank Ri is negative. Considering the submerged sediment surrounded by water as a fluid, the density of the fluid inside the tank consists of a composition of water and a denser fluid formed by sediment and water. In the experiments carried out in the present study, the difference between the densities of the fluids is near zero when the plastic material is employed and negative when the glass material is considered. Figure 37 presents the range of the dimensionless parameters considering actual ballast tanks, experimental studies reported in the literature and the experiments carried out in the present study. The experiments are within the flow regime and density difference that occur in actual ballast tanks.

Figure 37 – Dimensionless parameters comparison.

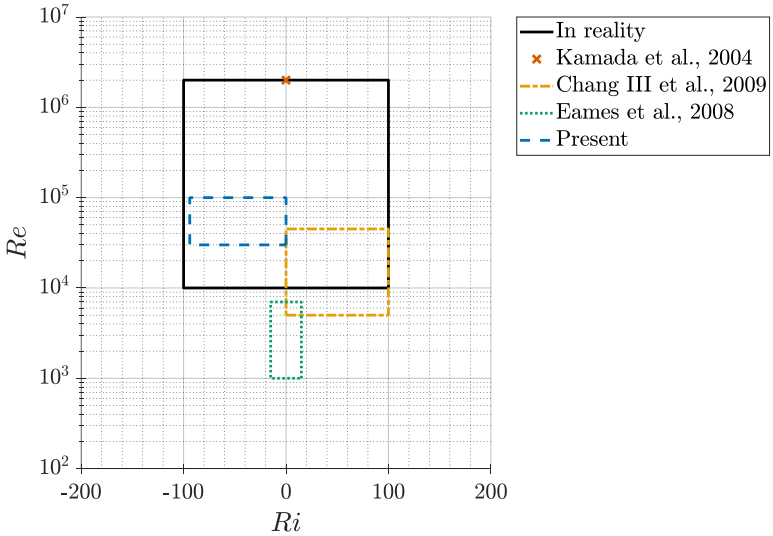

Source: adapted from Qi (2015).

4.3 VALIDATION OF NUMERICAL METHOD

4.3.1 Dimensionless variables

The investigation of the sediment removal efficiency is performed based on the amount of the sediment remained inside the double bottom ballast tank model. Since simplified 2D flow experiments and simulations were carried out, one approach to compute the amount of sediment is making use of the colored pixels of the images from the videos recorded in the experiments or rendered from simulations. The distortions of the camera lens were corrected before the pixels counting procedure. The colors of experimental sediments are yellow and orange for the plastic and glass material, respectively. In the simulations, the fluid was rendered as transparent and the sediment as magenta. Based on this approach, the area ratio is defined as follows

$$A_r = \frac{A_n}{A_0} \tag{39}$$

where A_0 and A_n are the number of sediment colored pixels at initial instant and instant n, respectively. The area ratio can be easily obtained from the post-processing of the images so that the time histories of the area ratio can be used as a reference to investigate the efficiency of the sediment removal and analyze the dynamics process obtained experimentally and numerically. However, despite the relatively small width of the 3D experimental and numerical model tanks used in the present study to reproduce 2D flow, as the colored pixels of the images of the sediment are actually the projection of small sediment particles inside the 3D models tanks, when sediment dispersion occurs inside the tank, the area ratio computed from colored pixels of the images is actually an overestimated amount of sediment particles. This is the reason why area ratio might be much larger than one when large sediment dispersion occurs. In this way, the value of the area ratio can be used as a reference to understand the dynamics of the sediment removal process, but not as an accurate estimation of the amount of the sediment inside the tank.

The area ration is calculated as a function of the dimensionless time T as follows

$$T = \frac{Qt}{V} \tag{40}$$

where Q is the flow rate, t the flushing time and V is the ballast tank volume. $T = 0$ corresponds to the opening of the gate valve in the experiments and begin of fluid acceleration in the simulations. The dimensionless time instant of the end of the transient period (T_t) can be measured based on the time that the water level inside the manometers takes to stabilize, showed in Table 8 as duration of the transient period. For better analysis of the process in steady flow regime, the dimensionless time is defined as follows by disregarding the transient period.

$$T^* = T - T_t \tag{41}$$

As a parameter to reflect the amount of sediment remained inside the tank, the sediment removal coefficient is defined by counting the actual amount of the sediment particles. As the actual volume of the sediment is difficult to be obtained when the sediment dispersion occurs, it is determined in the initial and final instants of the experiments and simulations, when the fluid is at rest or the flow calms down, and dispersion of sediment is nearly zero. The sediment removal coefficient is defined as:

$$R_r = 1 - \frac{S_f}{S_0} \tag{42}$$

where S_0 and S_f are, respectively, the volume of sediment in the initial and final instants. As a reference for the analysis, the instant $T^* = 3$, i.e., when the steady flow achieves three times the volume of the model tank, is used as final instant. It is important to point out that, as the model tank is only a simplified representation of a section of an actual ballast tank, three times the volume of model tank is much lower than the three times the tank volume required by the flow through process.

The interior the ballast tank model was divided in three regions delimitate by the stiffeners and denominated as Zone 1, 2 and 3 following the flow direction as is shown in the Figure 38. The division aims to make easy the analyses of results and better understand the process of sediment removal. In the beginning, the sediment is positioned in the bottom of each Zone uniformly distributed and with the same height, providing the same initial material amount.

Figure 38 – Regions of measurement entire tank (a) and three Zones (b).

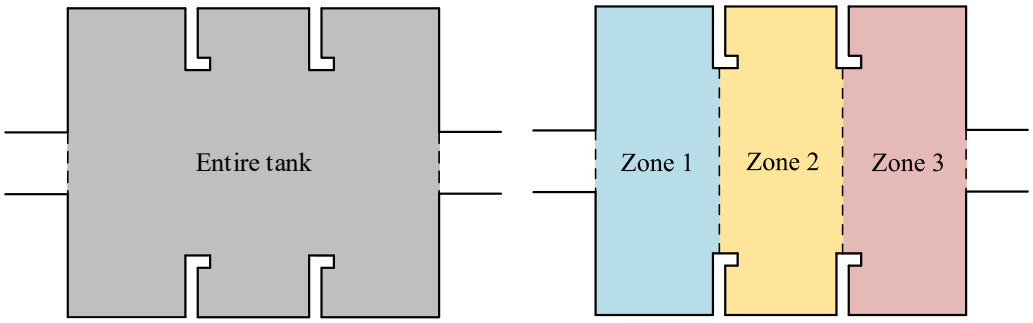

(a) (b)

Source: the author.

4.3.2 Validation case

The validation of the numerical method was performed comparing the experimental results for the case SW-P25, which involves less dense material and larger flow rate. The duration of simulation was 20 s and the measured velocity was 1.0 m/s, as showed in Table 8. The simulations were carried out using a 3D model with width of $W = 0.05$ m and four distances between particles: $l_0 = 5.0, 3.5, 2.5$ and 2.0 mm, corresponding to the resolutions $W/l_0 = 10, 15, 20$ and 25, respectively. Table 9 shows the numerical parameters, number of particles and computational time for each resolution. The pressure smooth coefficient (γ_1) and the artificial compressibility coefficient (α) adopted for all resolutions were 0.003 and 10^{-8}, respectively.

Table 9 - Numerical parameters, approximate number of particles and computational cost.

Distance between particles (l_0) [mm]	5.0	3.5	2.5	2.0
Resolution (W/l_0)	10	15	20	25
Number of particles	244480	599640	1491984	2647680
Time step [ms]	0.1	0.1	0.1	0.05
Computational nodes†	4	8	12	12
Computational time [hr]	19.8	32.0	65.6	301.5

Source: the author. †Cluster with 184 dedicated nodes Sun Blade X6275-2 Intel© Xeon© Processors X5560 (4 cores, 2.8 G25z and 24 GB of memory each).

Figure 39 shows the experimentally recorded images of SW-P25, as well as the corresponding numerically obtained snapshots by using resolution $W/l_0 = 10$, at the three instants $T^* = 1, 2$ and 3. The images show that while the sediment removal is effective in the Zone 3, accumulation of the sediment occurs in the Zone 1. The sediment in the Zone 3 is lifted and carried in the flow due to the vortex formed close to the outlet, as showed in Figure 39 (a3,

b3 and c3). The sediment accumulates in the Zone 1 due to the displacement of the material from the Zone 2, and only those sediments in the center of the tank that are perturbated by the high flow velocity are removed. The comparison between experimental and numerical results shows good agreement and the ability of the numerical model reproduces qualitatively the complex flow through with sediment removal.

Figure 39 – Experimentally recorded images and snapshots from the numerical simulations: SW-P25 (ABS) experimentally recorded images (a1, b1, c1), computed velocity field and sediment ($W/l_0 = 10$) (a2, b2, c2), velocity vectors (a3, b3, c3) at $T^* = 1$ (a1, a2, a3), $T^* = 2$ (b1, b2, b3) and $T^* = 3$ (c1, c2, c3).

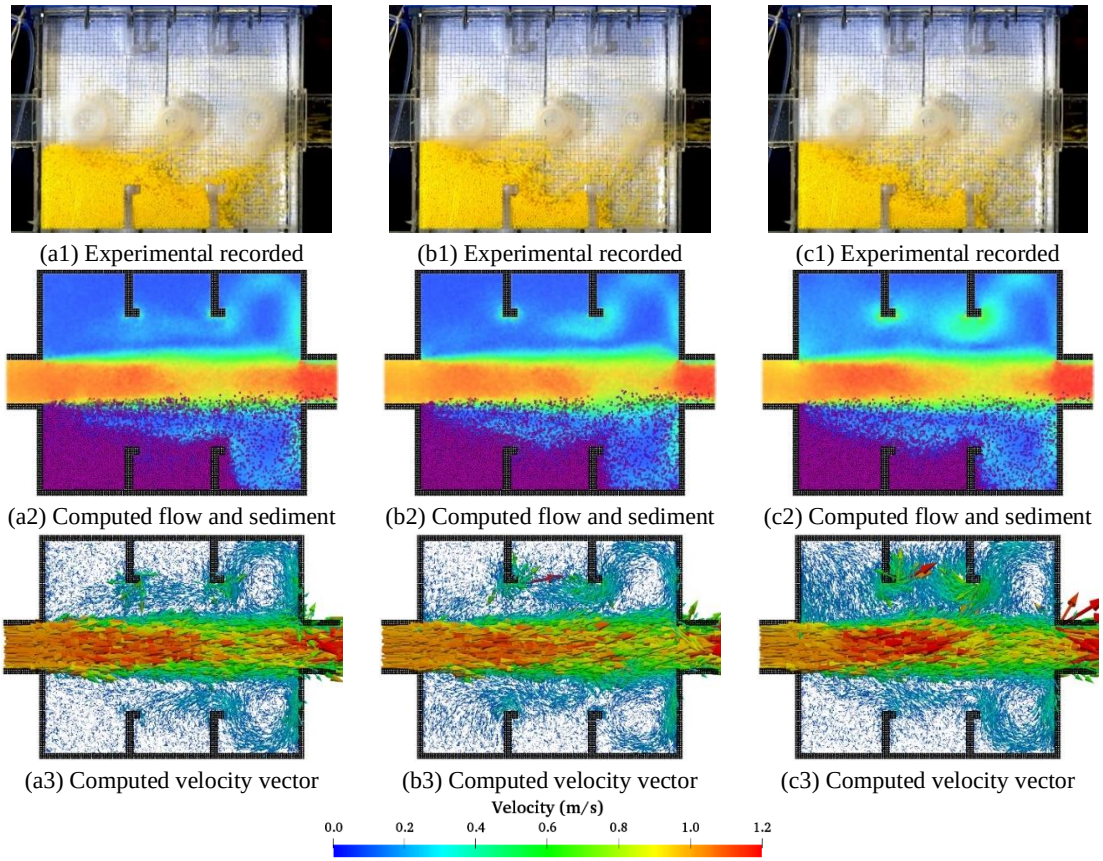

Source: the author.

The experimentally and numerically obtained time series of area ratio of the validation case SW-P25 are provided in Figure 40. The area ratios of the sediment in the Zone 1 measured experimentally and computed numerically using the different resolutions increase until reaches approximately two times the initial area ratio (see Figure 40 a). Similar process occurs in the Zone 2, where the area ratio varies between 1.5 and 2.3 (see Figure 40 b). On the other hand, the sediment area ratio in Zone 3 increases shortly in the beginning and decreases during the experiment, due the lifting and consequent removal of the material (see Figure 40 c).

Figure 40 – Time histories of sediment area ratio obtained experimentally and numerically for SW-P25 (ABS) Zone 1 (a), Zone 2 (b) and Zone 3 (c).

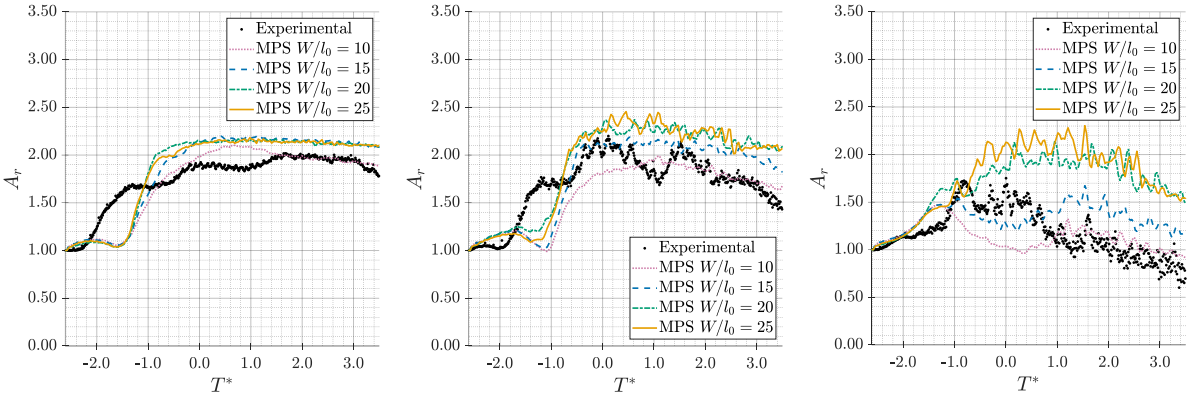

(a) (b) (c)

Source: the author.

For the entire tank, as illustrated in Figure 41, the area ratio increases during the transient period due to the dispersion of the sediment, which result in a temporary increase of sediment colored pixels in the images. After that, the area ratio decreases during the steady state, showing the effects of the sediment removal by the flow through process.

Figure 41 – Time histories of sediment area ratio obtained experimentally and numerically for SW-P25 (ABS) entire tank.

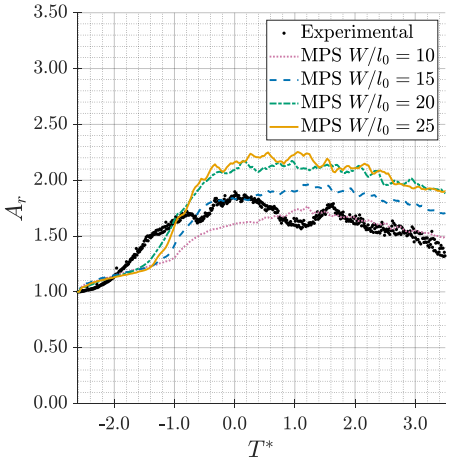

Source: the author.

The comparison between experimental and numerical results shows that despite the time lag in the transient regime, which might be caused by the deviation of the initial conditions of the numerical models from the experiments, the general behavior of the sediment removal process was reproduced in the numerical simulations. Also, specifically in this study, due to granular feature and size of the sediment used in the experiment, relatively low-resolution model with $W/l_0 = 10$, which corresponded to $l_0 = 5$ mm, reproduces nicely the experiments.

Considering the computational cost, the coarse resolution $W/l_0 = 10$ was chosen for the simulations carried out in the present study. However, for the cases with inlet from bottom the resolution $W/l_0 = 20$, which corresponds to $l_0 = 2.5$ mm, was adopted due the relatively small bottom opening (0.025 m).

4.4 RESULTS AND DISCUSSION

4.4.1 Cases with side wall inlet and without deflector

The remaining cases with side wall inlet and without deflector are shown in Figure 42, in which only the results at $T^* = 3$, which corresponds to three times volume exchange inside the model tank, are given. In the case SW-P15 (Figure 42 a1, a2 and a3), difference between measured and computed results occurs mainly in the Zone 3, probably due to the numerical damping effect that affects more significantly the reduced vortex generated by the lower flow rate (Figure 42 a3). In comparison with the case SW-P25 (Figure 39 a3, b3 and c3) shown in the validation study, the results confirm lower sediment removal effectiveness due the smaller flow velocity and consequently less intense vorticity.

In cases SW-G15 (Figure 42 b1, b2 and b3) and SW-G25 (Figure 42 c1, c2 and c3), which correspond respectively to glass material and 1.5 as well as 2.5 valve handle turns, the sediment motion is very small and nearly negligible, and no sediment removal occurs. In this way, the relatively low effectiveness of removing heavy sediment entrapped between the stiffeners by flow through approach. Also, despite the simplified modeling of the rheological behaviors, the numerical results present good agreement, especially considering the heavier sediment.

Figure 42 – Experimentally recorded images and snapshots from the numerical simulations: cases SW-P15 (a1, a2, a3), SW-G15 (b1, b2, b3) and SW-G25 (c1, c2, c3) experimentally recorded images (a1, b1, c1), computed velocity field and sediment (a2, b2, c2), and velocity vectors (a3, b3, c3) at $T^* = 3$.

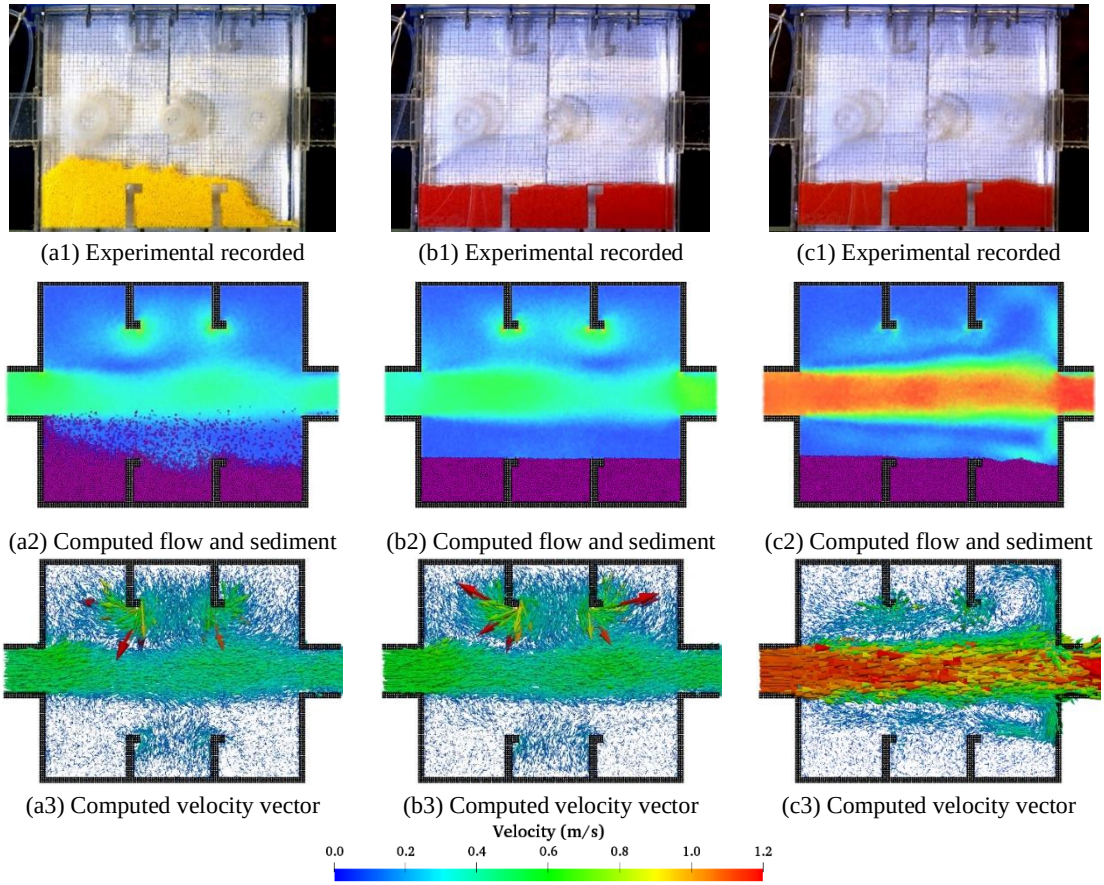

Source: the author.

The time histories of sediment area ratio obtained experimentally and numerically for cases SW-P15, SW-G15 and SW-G25 are given in Figure 43, in which the curves Z1, Z2, Z3 and ET represent the sediment area ratio of Zone 1, 2, 3 and the entire tank, respectively. In Figure 43 (a), the experimental result of the case SW-P15, which correspond to plastic material and 1.5 valve handle turns, shows a slightly increase of sediment in Zone 1 and decrease of sediment in Zone 3, due displacement of the sediment inside the tank and removal of the sediment in Zone 3. On the other hand, in the simulations the sediments removal from Zone 3 is relatively low. In Figure 43 (b) and (c), the experimental and numerical results of the cases SW-G15 and SW-G25, which correspond respectively to glass material and 1.5 as well as 2.5 valve handle turns, show extremely low displacement of sediment. Except for Zone 3 of SW-P15, all the area ratio time histories converge to a value at the final instant $T^* = 3$. This fact shows that the sediments in the tank will remain almost unchanged even considering longer flow through process.

Figure 43 – Measured and computed time histories of area ratio in Zone 1 (Z1), Zone 2 (Z2), Zone 3 (Z3) and entire tank (ET) for SW-P15 (a), SW-G15 (b) and SW-G25 (c).

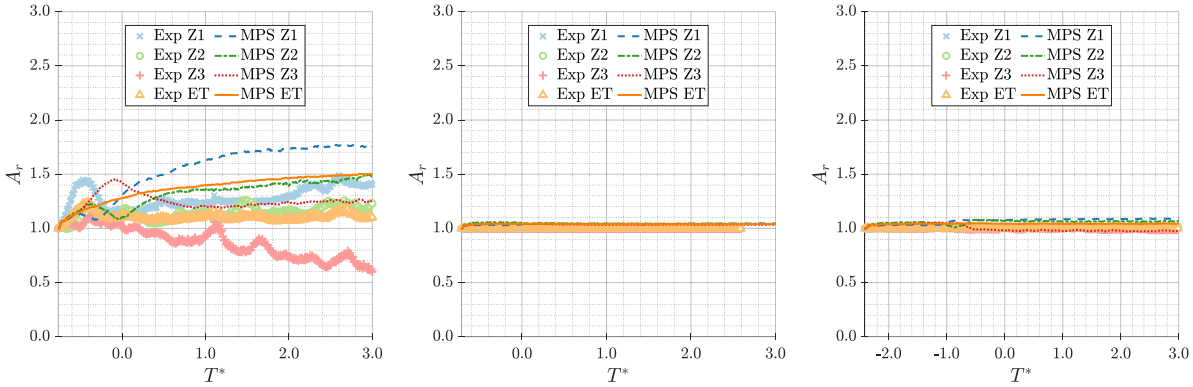

(a) SW-P15 (b) SW-G15 (c) SW-G25

Source: the author.

4.4.2 Cases with side wall inlet and with deflector

In this section, the effects of the presence of a flow deflector forming angles: $\theta = 30°, 90°$ and $120°$ in relation to the flow direction are investigated.

Figure 44 provides the images of flow deflector with $\theta = 30°$ at $T^* = 3$, i.e., after three times the volume exchange inside the tank. Only the results of three of the four cases are given in the figure because with heavier sediment the results show almost no sediment removal so that its results related to low flow rate is not worth being presented. Comparing the experimental results of cases SD-A030-P15 (Figure 44 a1, a2 and a3) and SD-A030-P25 (Figure 44 b1, b2 and b3), with lighter plastic material as sediment but different flow rates, the case SD-A030-P25, with higher flow rates, presents more suspended material and less sediments remaining in the tank, showing the effects of the stronger vortices generated by larger flow rate. This is confirmed by the numerical results (Figure 44 a3 and b3), which exhibit a high velocity flow underneath the deflector, and vortices inside Zone 1, 2 and 3 that enhances the sediment removal. The vortices lift the sediment and when the suspended sediment approach the high velocity flow around the deflector, it is carried and removed from the tank. Especially in Zone 2 and 3, much stronger and lower vortices combined with lower high-speed stream leads to remarkable sediment removal in these zones.

For the case SD-A030-G25 (Figure 44 c1, c2 and c3), with heavier glass material as sediment, both the experimental and the numerical results show that only the sediment of Zone 2, which is underneath the deflector, is eroded and partially removed by the deflected flow. In comparison with the lighter sediments (Figure 44 a1, a2, b1 and b2), the relatively low effectiveness of removing heavy sediment entrapped between the stiffeners by flow through

approach is also confirmed in this configuration. However, in relation to the case without the deflector SW-G25 (Figure 42 c1, c2 and c3), despite the more complex configuration, the effectiveness of the deflector in providing additional heavier sediment removal can be verified.

Figure 44 – Experimentally recorded images and snapshots from the numerical simulations: cases SD-A030-P15 (a1, a2, a3), SD-A030-P25 (b1, b2, b3) and SD-A030-G25 (c1, c2, c3) experimentally recorded images (a1, b1, c1), computed velocity field and sediment (a2, b2, c2), and velocity vectors (a3, b3, c3) at $T^* = 3$.

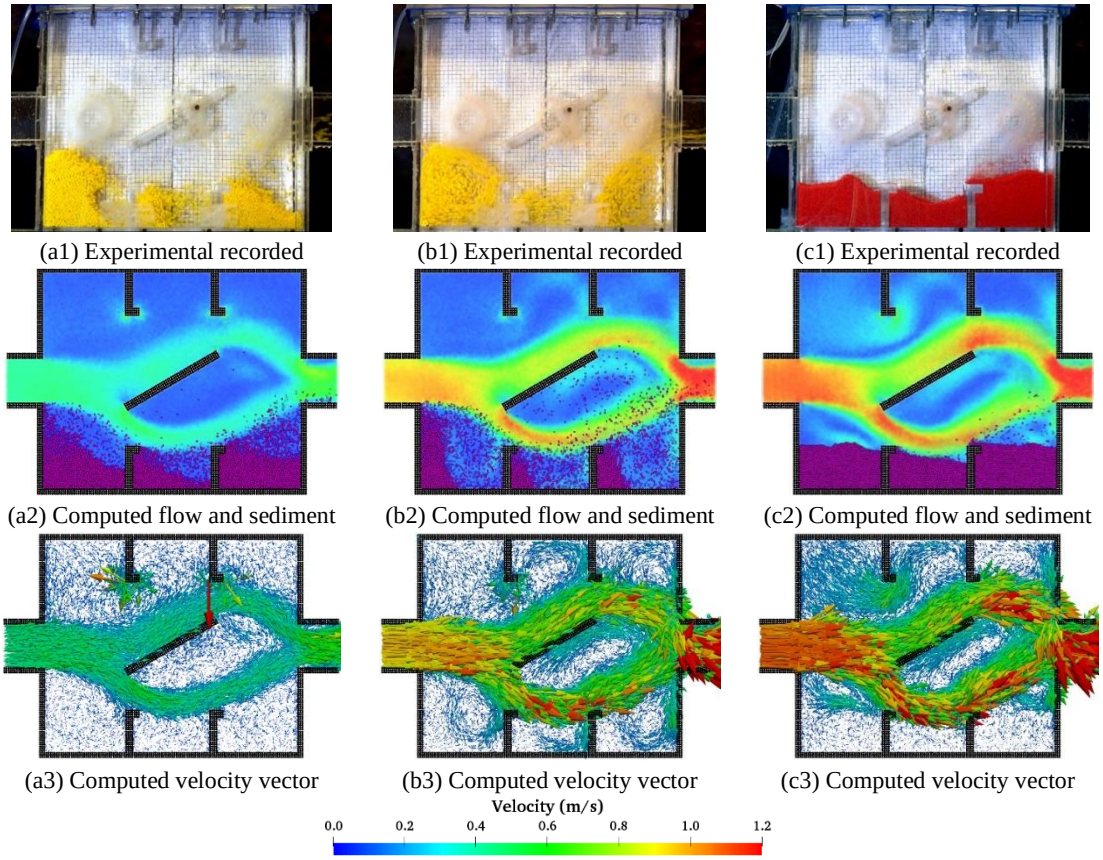

Source: the author.

In Figure 45, the measured and computed time histories of sediment area ratio for cases with flow deflector angle $\theta = 30°$ are presented. For case SD-A030-P15 (Figure 45 a), according to the experiment, the sediments of all Zones are suspended in the initial instants reaching a maximum peak before $T^* = 0$. This fact, as well as the peak value, is reproduced in the numerical simulations, for Zone 2. For Zone 3, the computed peak is delayed and with lower peak. On the other hand, in the transient period, the computed arear ratio of Zone 1 is very different to the experimental one, and no remarkable peak of the area ration were computed in the transient period. Nevertheless, after the transient period, in all the three zones, the experimental and numerical results agree very well, as the overall area ratio of the entire tank.

Between $T^* = 0$ and $T^* = 3$, the sediment area ratio decreases monotonically due sediment removal, which occur more remarkably in Zone 2 and 3.

For case SD-A030-P25 (Figure 45 (b)), light sediment under larger flow rate, due to large flow velocity and strong vortices formed in all Zones, remarkable sediment suspension and dispersion occurs, which results in large area ratio shown in the graph. However, after reaching the steady state, significant reduction of the area ratio is obtained. Compared to the case SW-P25, straight flow through without the deflector (Figure 41), the effectiveness of the deflector for the sediment removal is shown. It is interesting to point out that, in this case, the transition behavior of the area ratio is quite well reproduced in the simulation. After $T^* = 0$, despite the computed area ratios are lower than the experimental ones for all three zones, decrease of the area ratios could be qualitatively captured by the numerical modeling.

For case SD-A030-G25 (Figure 45 (c)), in both experimental measurement and numerical simulation, only the area ratio in Zone 3 increased significantly during the transient period . This increase of area ratio is caused by the heavy sediment of Zone 2 suspended by the deflected flow and passes through the Zone 3 to reach the outlet. On the other hand, the gradual reduction of the area ratio in Zone 2 illustrated the removal of the heavy sediment in this zone. Finally, the sediment in Zone 1 remains almost unchanged. Generally, the numerical results agree well with the experimental ones, especially in the case of heavy sediment.

Figure 45 – Measured and computed time histories of sediment area ratio in Zone 1 (Z1), Zone 2 (Z2), Zone 3 (Z3) and entire tank (ET) for SD-A030-P15 (a), SD-A030-P25 (b) and SD-A030-G25 (c).

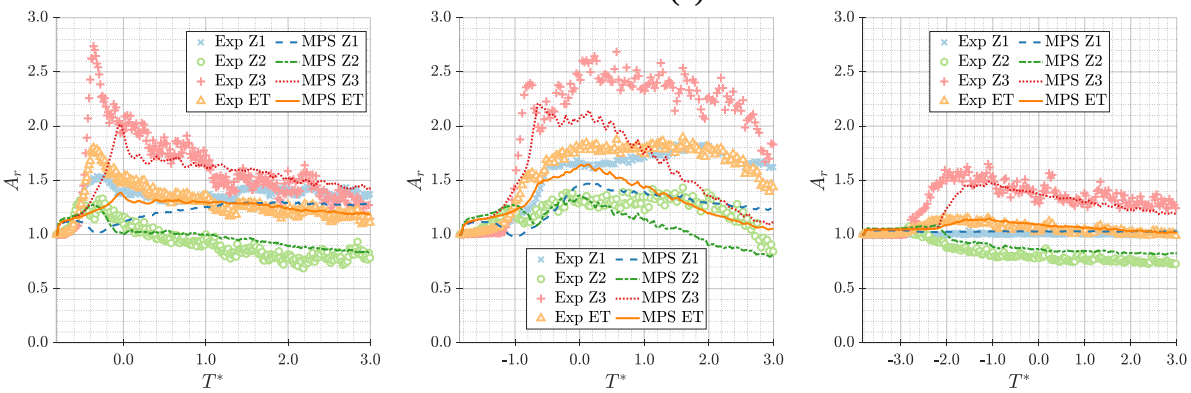

(a) SD-A030-P15 (b) SD-A030-P25 (c) SD-A030-G25

Source: the author.

Figure 46 shows the images obtained considering deflector with angle $\theta = 90°$ at $T^* = 3$ associated to the cases SD-A090-P15, SD-A090-P25 and SD-A090-G25. The still images recorded experimentally show that both SD-A090-P15 and SD-A090-P25, with light sediments,

significant amount of sediments remained in Zone 1, and the sediment was almost completely removed in Zone 2 and Zone 3.

The numerical results (Figure 46 a3, b3 and c3) show that the deflector deviate the flow that erodes the sediment in Zone 2 and generates large vortices that lift and remove the sediments in Zone 3. Nevertheless, the computed results present larger amount of residual sediment in Zone 3 in both cases SD-A090-P15 and SD-A090-P25.

Figure 46. Experimentally recorded images and snapshots from the numerical simulations: cases SD-A090-P15 (a1, a2, a3), SD-A090-P25 (b1, b2, b3) and SD-A090-G25 (c1, c2, c3) experimentally recorded images (a1, b1, c1), computed velocity field and sediment (a2, b2, c2), and velocity vectors (a3, b3, c3) at $T^* = 3$.

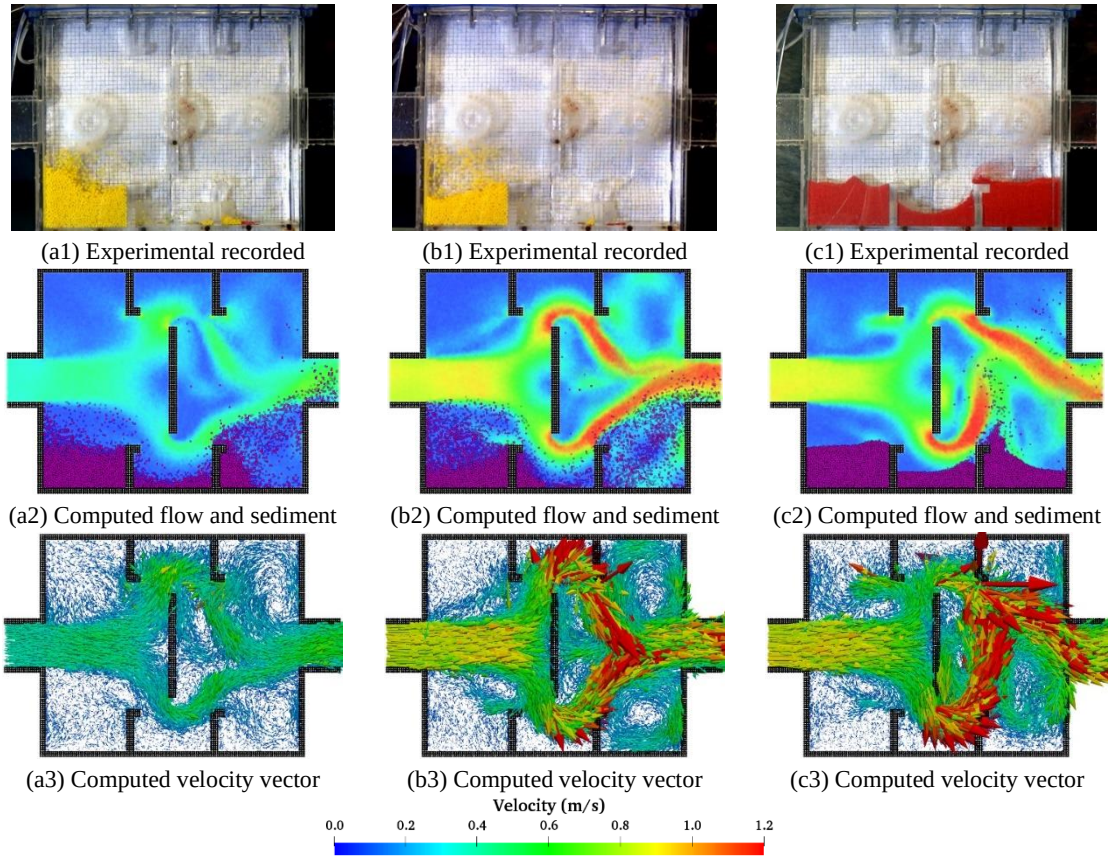

Source: the author.

The area ratio time histories of cases with flow deflector angle $\theta = 90°$ are presented in Figure 47.

In cases SD-A090-P15 and SD-A090-P25 (Figure 47 (a) and (b)), with light sediment, the experimental and numerical results show that the sediments were lifted during the transient period. The experimental results show that the sediment in Zones 2 and 3 were quickly removed from the ballast tank, with remarkable decrease of the area ratios. On other hand, computed

area ratios decrease slower, which lead to some errors in the final remaining amount of sediments. However, for Zone 1, the experimental and numerical results agree well.

Figure 47 (c) shows the area ratio time histories of the of the case SD-A090-G25, with heavier sediment. It is interesting to point out that in Zone 3 the variation of suspended sediments is significantly large, and the sediment removal in Zone 2 is the largest one of the three zones and steeply decrease of sediments occurred. Despite some differences, in general the numerical results also agree relatively well with the experimental ones, reproducing the general behavior of the sediment removal process.

Figure 47 – Measured and computed time histories of sediment area ratio in Zone 1 (Z1), Zone 2 (Z2), Zone 3 (Z3) and entire tank (ET) for SD-A090-P15 (a), SD-A090-P25 (b) and SD-A090-G25 (c).

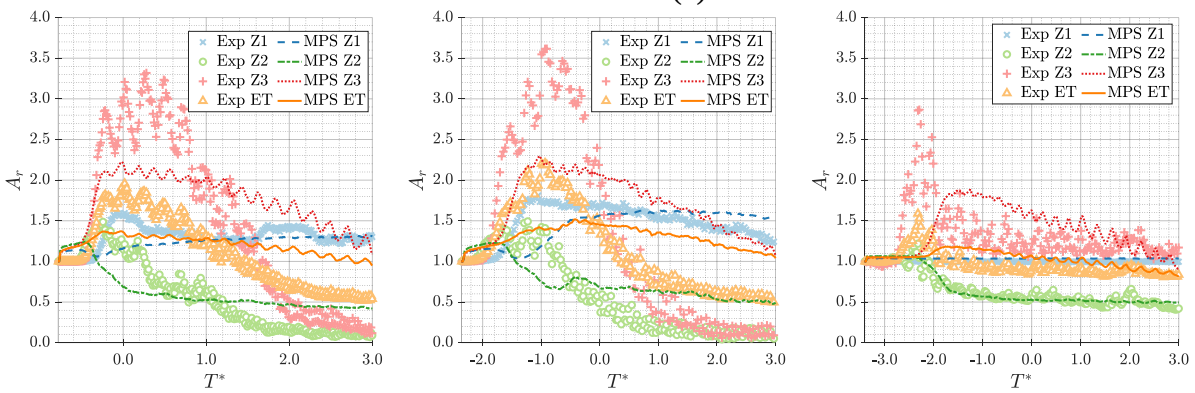

(a) SD-A090-P15 (b) SD-A090-P25 (c) SD-A090-G25

Source: the author.

Figure 48 shows the images obtained considering deflector with angle $\theta = 120°$ at $T^* = 3$. The experimental results of the cases SD-A120-P15 and SD-A120-P25 (Figure 48 a1 and b1), with lighter sediments, show that significant amount of sediments accumulated in Zone 1, and the sediment removal is effective in Zone 2 and 3. In case SD-A120-P15, with lower flow rate, few sediments can also be found in Zone 2. The numerically computed velocity fields (Figure 48 a2 and b2) show high flow velocities on the tip of the deflector with $\theta = 120°$ because of the small gap left between the tips and the stiffeners. As a result, strong vortices (Figure 48 a3 and b3) are generated near the tips and effective sediment removals occur in Zone 2 and 3. On the other hand, relatively low speed zone created in the Zone 1 leads to negligible removal, and the vortex in Zone 2 leads to a back flow that move the sediment of Zone 2 to Zone 1, which explains the experimentally observed accumulation of the sediment in Zone 1 (Figure 48 (b3)).

Regarding the case SD-A120-G25, with heavier sediment, Figure 48 c1, c2 and c3 show that high velocity flow close to the tips of the deflector is almost unable to remove the sediment, and while the sediments in Zone 1 and 3 remain nearly unchanged, only Zone 2 presented small removal of the sediment.

The comparison between experimental and numerical results show that despite some difference in the amount of the sediments remained in the Zones, the final distribution of the sediment in the were reproduced fairly well by the numerical model both in low and high flow velocity and light and heavy sediments.

Figure 48 – Experimentally recorded images and snapshots from the numerical simulations: cases SD-A120-P15 (a1, a2, a3), SD-A120-P25 (b1, b2, b3) and SD-A120-G25 (c1, c2, c3) experimentally recorded images (a1, b1, c1), computed velocity field and sediment (a2, b2, c2), velocity vectors (a3, b3, c3) at $T^* = 3$.

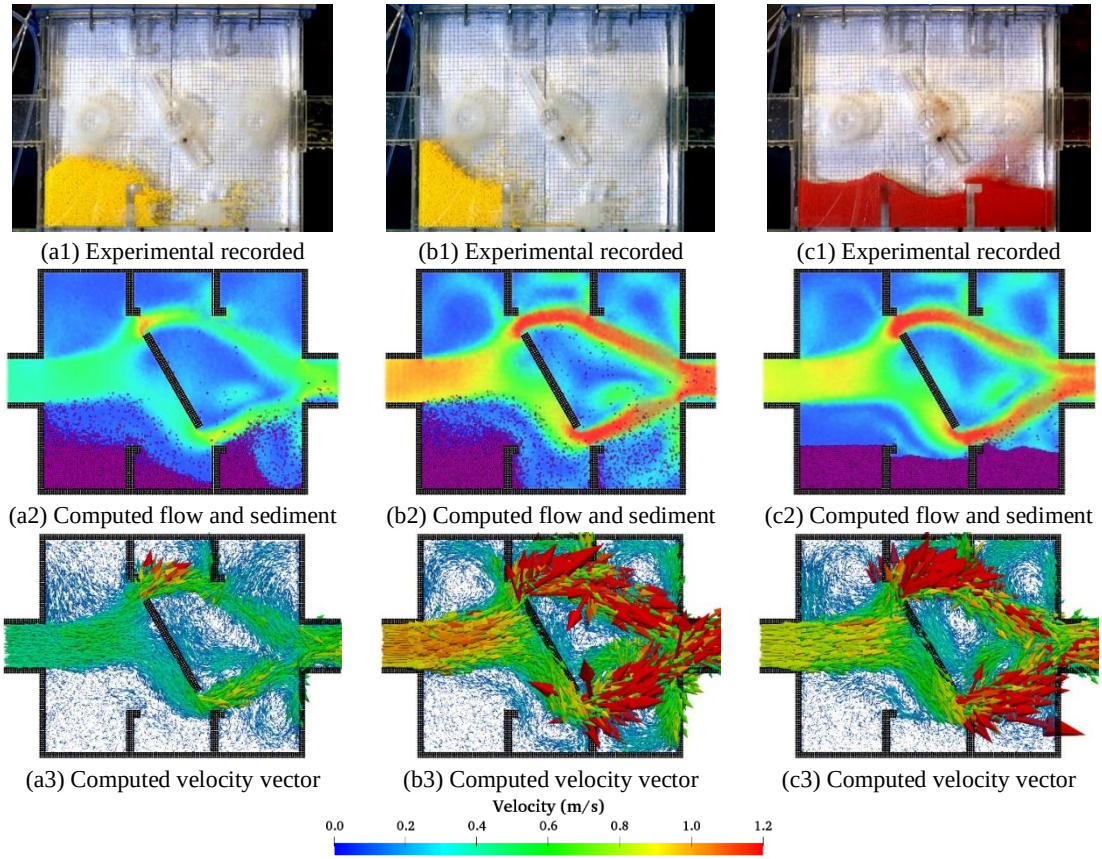

Source: the author.

The measured and computed time histories of area ratio for cases with deflector angle $\theta = 120°$ are presented in Figure 49. As in cases with deflector angle $\theta = 90°$, the experimental results shows that for light sediments, SD-A120-P15 and SD-A120-P25, given in Figure 49 (a) and (b), respectively, large dispersion of the sediment occurs in Zone 3 in the beginning, followed by effective removal of the sediment. After end of transient period, the

area ratio of Zone 2 also decreases significantly due to removal of the sediment. In the numerical results, the sediment dispersion is smaller, but the amount of remaining sediment in Zone 2 and 3 at $T^* = 3$ is slightly larger. In Zone 1, despite the time lag in the transient period, the computed curves and sediment amounts at $T^* = 3$ are similar to experimental ones.

In the case of heavier sediment, SD-A120-G25, of which the area ratio time histories are presented in Figure 49 (c), the measured and computed results agree well except in Zone 3, in which the computed dispersion is larger in the beginning. However, after end of transient period the numerical result converges to the experimental one.

Figure 49 – Measured and computed time histories of sediment area ratio in Zone 1 (Z1), Zone 2 (Z2), Zone 3 (Z3) and entire tank (ET) for SD-A120-P15 (a), SD-A120-P25 (b) and SD-A120-G25 (c).

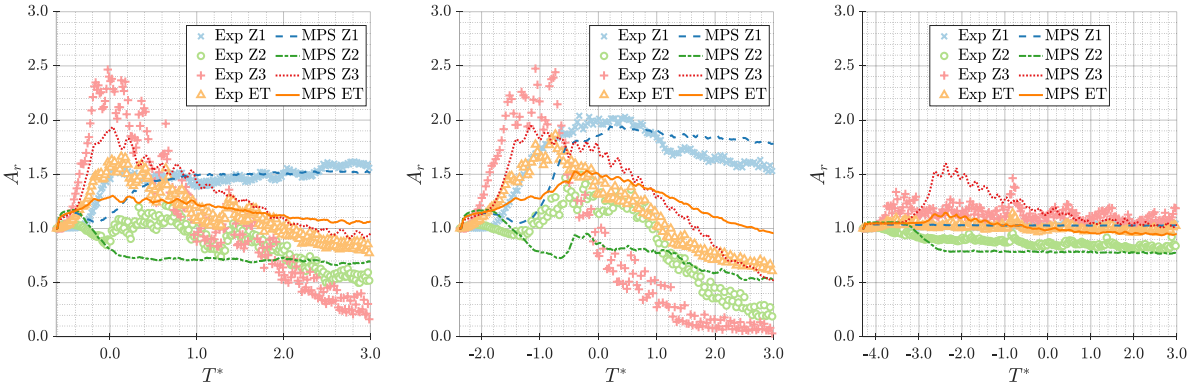

(a) SD-A120-P15 (b) SD-A120-P25 (c) SD-A120-G25

Source: the author.

By comparing the results obtained from the cases with and without the flow deflector, the effects on the sediment removal due to the flow perturbation induced by the deflector can be confirmed.

In case of the light sediments, instead sediment removal restricted to Zone 3, near the outlet, the deflector installed in the middle of the tank enhanced the sediment removal in the Zone 2 and 3. Considering the geometry of the internal structures analyzed herein, the deflector positioned with $\theta = 90°$ is the most effective one, providing nearly 100% cleaning in Zone 2 and 3 at $T^* = 3$, in both low and high flow rates. Nevertheless, like the case of $\theta = 120°$, the sediment remains entrapped in Zone 1, near the inlet. In this way, despite better performance with the deflector at $\theta = 90°$ or $\theta = 120°$, the solutions are only partially effective. On the other hand, with the deflector at $\theta = 30°$, the flow perturbation occurs in all the tank and provokes the dispersion of the sediment in three Zones, which might enhance the sediment removal. However, until $T^* = 3$, significant amount of sediments remained in all the Zones.

Finally, for heavier sediment entrapped within the bottom stiffeners, no sediment suspension occurs, and it is exceedingly difficult to be removed even using larger flow rate, and the flow deflector enhances slightly and locally the removal process by eroding the sediment.

4.4.3 Cases with inlet from bottom

Despite the flow deflector investigated in the previous subsection is not very effective to enhance the sediment removal, the obtained results show that flow perturbation that provokes sediment dispersion is relevant to the process. Thus, a more complex concept considering inlet from the bottom is analyzed in this sub session.

The still images at $T^* = 3$ of three of the four cases with the bottom inlet obtained experimentally and the snapshots computed numerically are given in Figure 50. In the cases BW-P15 (Figure 50 a1, a2 and a3) and BW-P25 (Figure 50 b1, b2 and b3), with lighter sediments, the sediments were completely removed from tank in experiments. In the numerical results, the sediments were also removed from the bottom, but there were few remaining sediments dispersed in flow.

In case BW-G25 (Figure 50 c1, c2 and c3), with heavier sediment, the experimental result indicates small amount of sediment remained beside the bottom inlets, while in the computed results only very few sediments remain on bottom of Zone 3.

Figure 50 – Experimentally recorded images and snapshots from the numerical simulations: cases BW-P15 (a1, a2, a3) , BW-P25 (b1, b2, b3) and BW-G25 (c1, c2, c3) experimentally recorded images (a1, b1, c1), computed velocity field and sediment (a2, b2, c2), velocity vectors (a3, b3, c3) at $T^* = 3$.

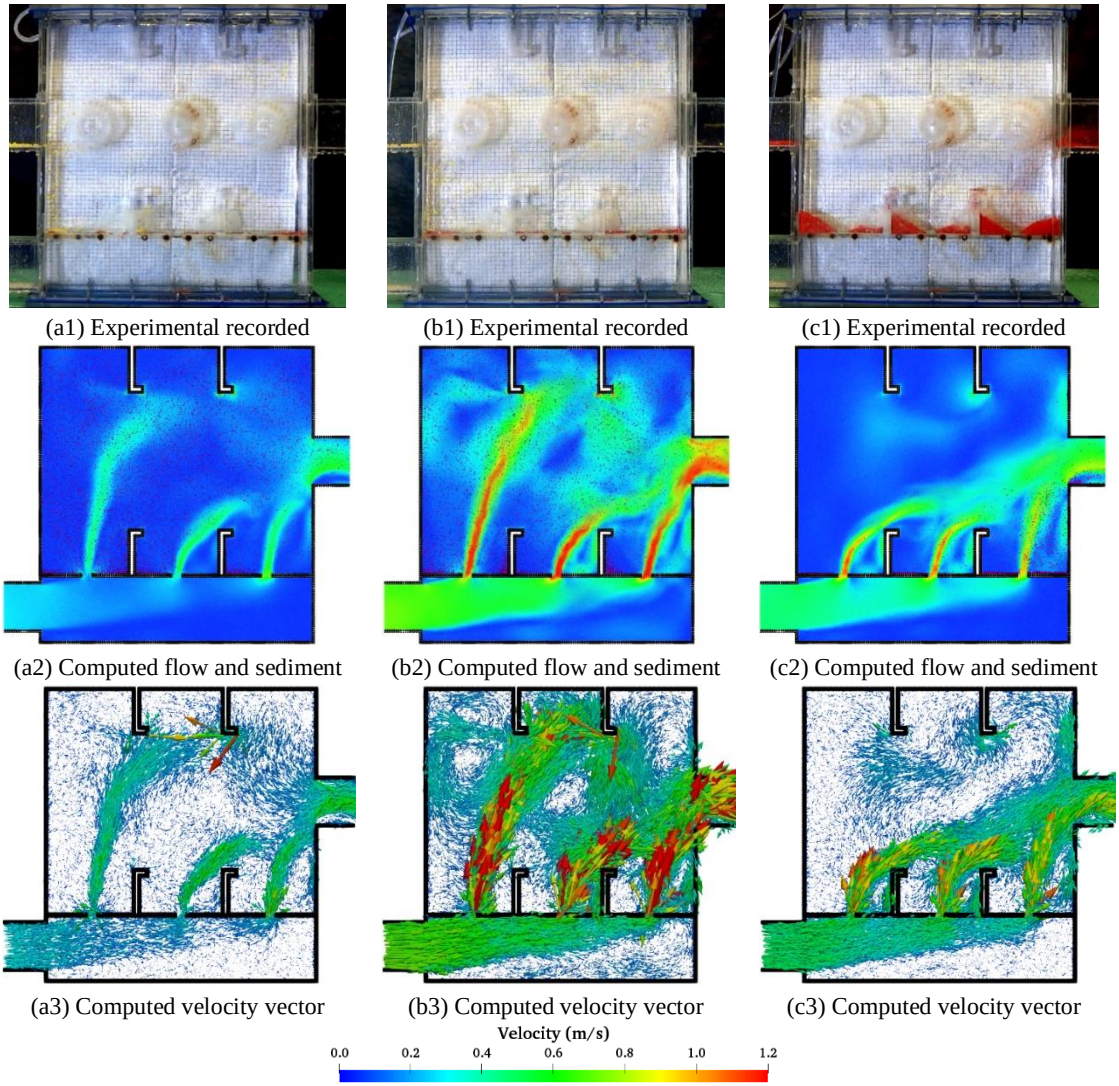

Source: the author.

Figure 51 shows time histories of the area ratio obtained experimentally and numerically for the cases with inlet from bottom. The results of the cases BW-P15 and BW-P25, given in Figure 51 (a) and (b), respectively, show a fast increase of the area ratios for both experimental and numerical results. This is caused by the dispersion of the sediments due to perturbation from the flow through the bottom openings. The numerical curves are delayed in relation to the experimental ones, in both cases BW-P15 and BW-P25. However, the behaviors of the experimental and numerical curves are similar. After reaching the peak values, the area ratios decrease rapidly. In the experiments, the sediment was completely removed before $T^* = 3$.

However, in the numerical results, there is an amount of remaining material in the all the three Zones, which are sediments dispersed in the flow, as shown in Figure 50 a2 and b2.

For case BW-G25, in Figure 51 (c), the experimental result shows a very fast and effective sediment removal process. On the other hand, delay of the numerical curves also occurs. However, at $T^* = 3$ the area ratio values are similar to the experimental results.

Figure 51. – Temporal comparison of experimental and numerical sediment area ratio in Zone 1 (Z1), Zone 2 (Z2), Zone 3 (Z3) and entire tank (ET) for BW-P15 (a), BW-P25 (b) and BW-G25 (c).

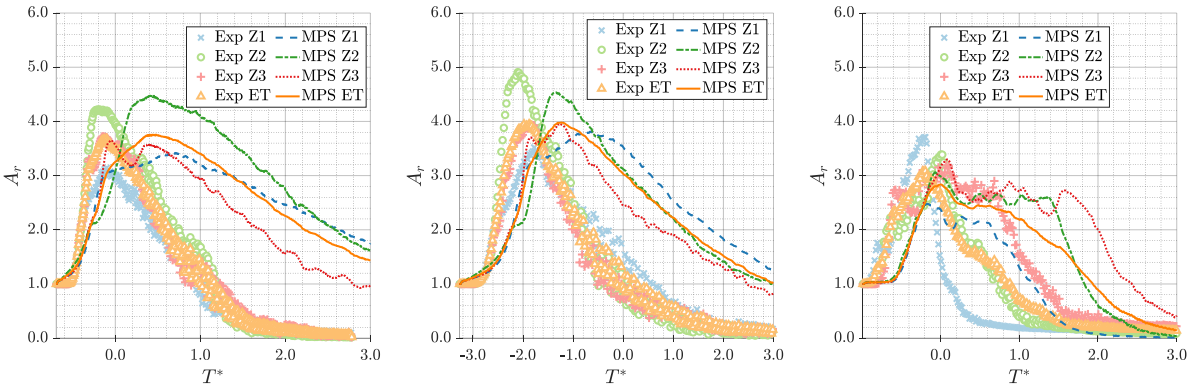

(a) (b) (c)

Source: the author.

In general, the experimental and numerical results agree fairly well, and both indicate that the inlet from bottom is able to generate large perturbation to the sediment and it is very effective for the sedimental removal.

4.4.4 Summary of the performances

Summarizing the results obtained, the sediment removal coefficient at $T^* = 3$ is presented in Figure 52, Figure 53 and Figure 54. In original configuration of the experiments, the sediment removal occurs only with lighter material associated to higher flow rate, as showed in Figure 52. In this condition the sediment removal coefficient reaches 30.4% and 22.8% in experiments and numerical simulations, respectively.

Figure 52 – Experimental and numerical sediment removal coefficient at $T^* = 3$ for cases with inflow from side wall and without deflector (SW).

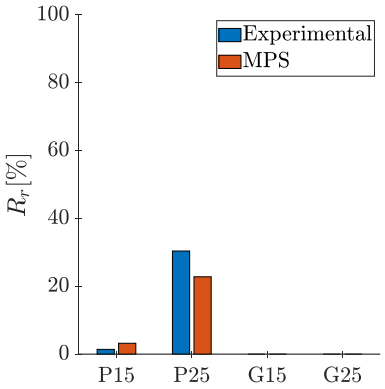

Source: the author.

The addition of the flow deflector increases the sediment dispersion and removal, and the case with flow deflector angle $\theta = 90°$ leads to the higher values of sediment removal coefficient for both lighter and heavier sediments, as showed in Figure 53. For lighter sediment, the measured and computed removal coefficients reach 72.8% and 64.5%, respectively under higher flow rate, and for the heavier sediment, these coefficients are 16.9% and 28.4%, respectively.

Figure 53 – Experimental and numerical sediment removal coefficient at $T^* = 3$ for cases with inflow from side wall and with deflector angle of 30° (a), 90° (b) and 120° (c).

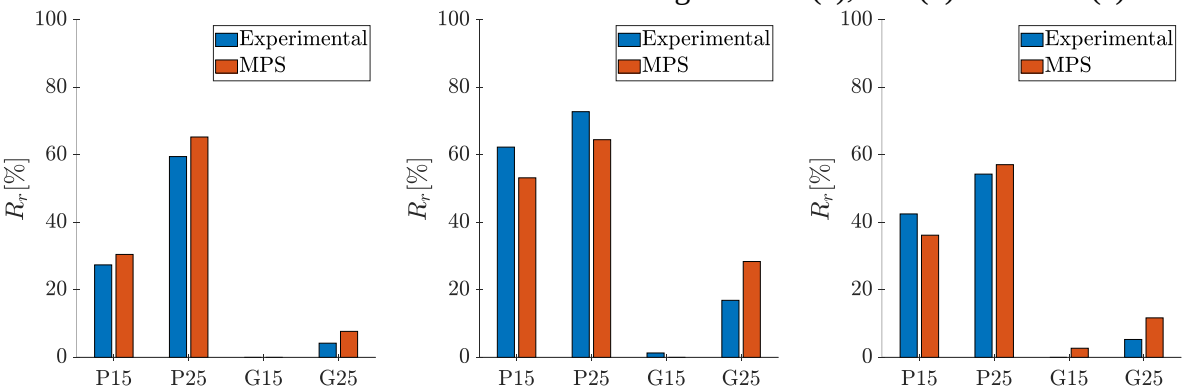

(a) SD-A030 (b) SD-090 (c) SD-120

Source: the author.

Much higher sediment removal occurs considering inlet from bottom. In case of lighter sediment, the removal is complete even for the case with low flow coefficient, as showed in Figure 54. Regarding the heavier sediment, despite the discrepancy between experimental and numerical results, which are 78.4% and 98.0%, respectively, both sediment removal coefficients are the best ones obtained with the heavier sediment.

Figure 54 – Experimental and numerical sediment removal coefficient at $T^* = 3$ for cases with inflow from bottom and without deflector (BW).

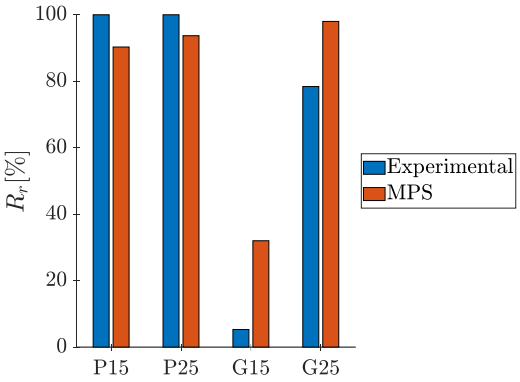

Source: the author.

Finally, it is important to point out that the results based on sediment removal at $T^* = 3$ does not correspond to the actual condition of flow through ballast water exchange, in which both the duration and flow volume are much higher than considered in the present experimental and numerical studies. However, since in most of the cases investigated herein the volume sediments remained unchanged after $T^* = 3$, it is clear that additional flow through the ballast tank tends to neglectable effects on the sediment removal. In this way, the performance of all the cases shown in the present paper is representative of the actual conditions.

5 FINAL REMARKS

This work was dedicated to numerically investigate two phenomena involving solid-liquid multiphase flow: waste transport inside a building drainage network and sediment removal inside a ballast tank. The numerical method adopted to model the complex geometries and flow behavior of the simulated cases was the Moving Particle Semi-Implicit (MPS), which is a Lagragian meshless particle-based method. The solid was modeled in two different ways: in the first study, the waste was modeled as a rigid body and, in the second study, the sediment was considered as a denser fluid.

5.1 NUMERICAL INVESTIGATION ON THE HYDRODYNAMICS AND WASTE TRANSPORT IN HORIZONTAL DRAINS OF A BUILDING DRAINAGE NETWORK

5.1.1 Influence of a wye on the hydrodynamics and waste transport

A simplified bathroom drainage model was adopted to investigate the hydrodynamics in the vicinity of a wye and its influence on transport of solids inside a horizontal drain. As a result, important conclusions can be drawn as follows:

1. In the case of lower diameter (75 mm) and low pipe slope (0 and 1%), the encounter of the wash basin and shower flows with the discharge of WC flush in the wye generates a backwater wave that propagates upstream in the drain 1. The magnitude of the wave height is dependent of the pipe slope and in the critical case, with null pipe slope, the wave height reaches 10 mm.
2. The height of water surface level inside the drain 2 depends on the diameter of the drain 1. The monitored sections of the drain 2 present pipe filling higher than 0.85 for almost 3 s for cases with diameter of 75 mm and null slope. Although the model neglected the presence of air entrapment, the high pipe filling might indicate a flow regime change from a free-surface to a pressure-driven flow, that is a undesirable condition, because it might compromise trap seals and reduce the flow rate.
3. When the solid is approaching the wye, its velocity decreased due the influence of the incoming flow from the drain 2. Then the water level behind the solid increases until it thrusts the solid to flow though the wye. The solid floats as the height of the water surface level increases, and it reaches the stack with a relatively high velocity. In the

cases with diameter of 100 mm and null pipe slope the incoming flow from the drain 2 reduced locally the flow velocity in downstream direction and did not increased sufficiently the heigh of the water surface level to lift the solid and eliminate the friction due contact between the solid and pipe. As a result, the solid stopped and remains deposited before the wye until end of simulation.

Since high filling ratios were computed in several cases investigated herein, as recommendation for further study, the effect of the air entrapped should be considered. Moreover, the investigation of the influence of the wall boundary modeling, performed after the simulations of simplified bathroom drainage model, showed that the particle wall modeling should present large unnatural energy loss. Therefore, comparison with results using the polygon wall modeling should be recommended in future research.

5.1.2 Influence of the wall boundary modeling of circular geometries

The unphysical frictional loss inside the pipe is investigated by considering two models: particle and polygon wall modeling. From the outcome results and comparisons conducted here, important conclusions can be drawn as follows:

1. For the simulations adopting particle wall modeling, the increase of the resolution leads to a decrease of the water level and the convergence is not achieved. On the other hand, convergence is achieved for all simulations with polygon wall modeling.
2. Compared to the results of the polygon wall modeling, lower flow velocity and higher water levels are computed in simulations with particle walls due the significant unphysical friction, i.e., a large unnatural energy loss.
3. A considerable decrease of the water levels along the pipe occurs for the simulations with particle wall modeling, while they remain almost constant for the simulations with polygon walls.

Furthermore, the convergence was not reached in the simulations with the discrete particle wall modeling, which requires higher resolution models, and demands much larger computational resources.

5.2 EXPERIMENTAL AND NUMERICAL ANALYSIS OF SEDIMENTS REMOVAL OF DOUBLE BOTTOM BALLAST TANKS

In the present study, the sediment removal process inside double bottom ballast tanks during the flow through process were investigated experimentally and numerically. The simplified experimental model was designed to study the influence of the flow rate and the sediment density on the sediment removal. In addition, the effectiveness of a flow deflector and inflow though the bottom were also verified.

As a reference for the analysis of sediment removal process, time histories of the area ratio are adopted to investigate the dynamic of the process. In addition to this, sedimental removal coefficients at the final instant of the experiments and simulations were used as a parameter to verify the effectiveness of the sediment removal. The final instant is defined as the instant when the steady flow reaches three times the volume of the model tank, and the results showed that almost no additional sediment removal occurs after this instant.

The results with the conventional double bottom tank configuration showed that:

1. the flow through process is ineffective to remove the sediments entrapped between the stiffeners.
2. The sediment removal is essentially restricted in the vicinity of the outlet, where vortex is generated.
3. Increasing of the flow rate enhances the removal of lighter sediment, but without inducing sediment perturbation and dispersion in the conventional tank configuration, its marginal benefit is extremely limited.
4. Density of the sediments play important role in the effectiveness of the removal process, since the perturbation and dispersion of the lighter sediment is much easier, its removal is much more effective than heavier sediments.

In the second phase, a flow deflector in the center of the tank was added and the outcomes showed that:

1. high velocity flow around the deflector and vortices in the bottom of the tank are induced, which perturbates the sediment and enhances its dispersion and removal.
2. Nevertheless, while the sediment is remarkably removed in the mid and aft zones of the tank, no sediment perturbation and removal occur in the vicinity of the inlet.
3. Among the three flow deflector angles considered in the study ($\theta = 30°, 90°$ and $120°$), the most effective one is $\theta = 90°$, i.e., perpendicular to the main stream direction, which achieved 72.8% and 16.9% of sediment removed for lighter and heavier sediment, respectively, under higher flow rates.

Finally, inlet from the bottom of the tank was considered, despite the complexity and feasibility of its physical implementation:

1. it provided the more effective sediment removal results, with almost perfect cleaning of the sediments entrapped between the bottom stiffeners.
2. For the cases with light sediment, the sediments were completely removed with low as well as high flow rates. For the case with heavier sediment, 21.6% of the sediment remained at the corners of the tank bottom.

In general, the numerical results agree well with the experimental ones, and the overall dynamic behaviors of the sediment removal process were reproduced by the numerical modeling. Some discrepancies in the absolute values of measured and computed results were obtained, but they are within the expectations considering the simplified experimental and numerical modeling in tank geometry, flow conditions and rheology of the sediment. In this way the proposed numerical approach is valid for qualitative investigation of the process.

In summary, some relevant insights about the most important variables of the sediment removal were obtained. However, further work is required to extend this analysis to more realistic tank geometries, especially considering full 3D models as well as more complex rheological characteristics of the sediments, more accurate measuring techniques and use of turbulence models in the numerical modeling.

REFERENCES

Akiyama, K., Otsuka, M., Shigefuji, H., 2014. Basic Study on a Method for Predicting the Waste-Carrying Performance in the Horizontal Drain Pipe of a Water-Saving Toilet, in: CIB W062. p. 12.

Amaro Jr., R.A., Osello, P.H.S., Cheng, L.-Y., 2017. Moving particle simulation with solid-solid contact, in: V International Conference on Particle-Based Methods – Fundamentals and Applications. pp. 734–743.

Amaro Jr, R.A., Pereira, L.S., Cheng, L.-Y., Shakibaeinia, A., 2019. Polygon Wall Boundary Model in Particle-Based Method: Application To Brumadinho Tailings Dam Failure, in: 25th ABCM International Congress of Mechanical Engineering. p. 10. https://doi.org/10.26678/abcm.cobem2019.cob2019-1869

Arai, J., Koshizuka, S., Murozono, K., 2013. Large eddy simulation and a simple wall model for turbulent flow calculation by a particle method. Int. J. Numer. Methods Fluids 772–787. https://doi.org/10.1002/fld

Arai, M., Makiyama, H.S., Cheng, L.-Y., 2002. Numerical Simulation of Sloshing of Water in Ship Tanks During Sequential Ballast Water Exchange in Seaways. https://doi.org/10.1115/OMAE2002-28261

Bellezi, C.A., Motezuki, F.K., Cheng, L.-Y., Nishimoto, K., 2013. Flow conditioning modeling and application to particle method, in: 3rd International Conference on Particle-Based Methods Fundamentals and Applications, Particles 2013. pp. 852–864.

Chang III, P.A., Wilson, W., Carneal, J., Atsavapranee, P., Verosto, S., Reid, D.F., Jenkins, P.T., 2009. Final Report: Computational modeling of Ballast Water tanks to improve understanding and maximize effectiveness of management practices and treatment mechanisms. phase ii -- extension of laboratory study, NATIONAL OCEANIC AND ATMOSPHERIC ADMINISTRATION.

Cheng, C.L., Liao, W.J., He, K.C., Hsieh, C.H., Liu, Y.C., 2013. Empirical approach to main drain system design and solid transportation performance in buildings. Build. Serv. Eng. Res. Technol. 34, 393–406. https://doi.org/10.1177/0143624412460239

Cheng, L.-Y., Oliveira, L.H., Favero, E.H., 2012. Particle-based Numerical Analysis of Drainage Flow inside Building System. Int. Symp. Cib W062 Water Supply Drain. Build. 227–238.

Cheng, L.-Y., Oliveira, L.H., Favero, E.H., Oliveira, I.B., Gonçalves, O.M., 2013. Simulation of drainage system in building using particle-based numerical method., in: International Symposium Cib W062 on Water Supply and Drainage for Buildings. pp. 77–91.

Cheng, L.-Y., Oliveira, L.H., Osello, P.H.S., Rubens Augusto, A.J., 2017. A numerical investigation on the hydrodynamic impact loads of the solid waste transport inside main drains. Int. Symp. Cib W062 Water Supply Drain. Build. 463–474.

Cheng, L.-Y., Oliveira, L.H., Osello, P.H.S., Rubens Augusto Amaro Jr., 2016. A numerical modeling of solid waste transport in main drain, in: International Symposium Cib W062

on Water Supply and Drainage for Buildings. pp. 1–10.

Cheng, L.Y., Oliveira, L.H., Ferracini, D.A., Gonçalves, O.M., 2014. A numerical study on waste transport in main drain, in: International Symposium Cib W062 on Water Supply and Drainage for Buildings. pp. 1–12.

Cundall, P.A., Strack, O.D.L., 1979. A discrete numerical model for granular assemblies. Géotechnique 29, 47–65. https://doi.org/10.1680/geot.1979.29.1.47

Eames, I., Landeryou, M., Greig, A., Snellings, J., 2008. Continuous flushing of contaminants from ballast water tanks. Mar. Pollut. Bull. 56, 250–260. https://doi.org/10.1016/j.marpolbul.2007.10.032

Fernandes, D.T., Cheng, L.-Y., Favero, E.H., Nishimoto, K., Liang, ·, Cheng, Y., Eric, ·, Favero, H., Nishimoto, K., Cheng, L.-Y., Favero, E.H., Br, K., 2015. A domain decomposition strategy for hybrid parallelization of moving particle semi-implicit (MPS) method for computer cluster. Cluster Comput. 18, 1363–1377. https://doi.org/10.1007/s10586-015-0483-3

GEF-UNDP-IMO GloBallast Partnerships Programme, 2017. The GloBallast Story: Reflections from a Global Family.

Gingold, R.A., Monaghan, J.J., 1977. Smoothed particle hydrodynamics: theory and application to non-spherical stars. Mon. Not. R. Astron. Soc. 181, 375–389. https://doi.org/10.1093/mnras/181.3.375

Gormley, M., Campbell, D.P., 2006. The transport of discrete solids in above ground near horizontal drainage pipes: A wave speed dependent model. Build. Environ. 41, 534–547. https://doi.org/10.1016/j.buildenv.2005.02.017

Güney, C.B., Danışman, D.B., Ertürk Bozkurtoğlu, Ş.N., 2020. Reduction of ballast tank sediment: Evaluating the effect of minor structural changes and developing a pneumatic cleaning system. Ocean Eng. 203. https://doi.org/10.1016/j.oceaneng.2020.107204

Hoffman, J., Juan, W., Sirimanne, S.N., Asariotis, R., Assaf, M., Benamara, H., Premti, A., Rodríguez, L., Weller, M., Youssef, F., 2018. Review of Maritime Transport.

Ikeda, H., Koshizuka, S., Oka, Y., Sun Park, H., Sugimoto, J., 2001. Numerical analysis of jet injection behavior for fuel-coolant interaction using particle method. J. Nucl. Sci. Technol. 38, 174–182. https://doi.org/10.1080/18811248.2001.9715019

International Maritime Organization, 2004. International convention for the control and management of ships ballast water and sediments.

Johengen, T., Reid, D., Fahnenstiel, G., MacIsaac, H., Dobbs, F., Doblin, M., Ruiz, G., Jenkins, P., 2005. Assessment of Transoceanic NOBOB Vessels and Low-Salinity Ballast Water as Vectors for Non-indigenous Species Introductions to the Great Lakes.

Johnson, K.L., 1985. Contact Mechanics. Cambridge University Press, Cambridge. https://doi.org/10.1017/CBO9781139171731

Kagami, H., Otsuka, M., Nakato, T., 2013. A Study on the Discharge Characteristics of Water-

Saving Toilets using Different Amounts of Flushing Water and the Evaluation of the Carrying Performance Thereof. Int. Symp. Cib W062 Water Supply Drain. Build. 129–142.

Kamada, K., Minami, K., Shoji, K., Shiotani, S., Ishida, H., 2005. Study of ballast water exchange by pumping-through method 1, 707–712. https://doi.org/10.1109/oceans.2004.1405520

Koshizuka, S., 1995. A Particle Method for Incompressible Viscous Flow with Fluid Fragmentation. Comput. Fluid Dyn. J. 4, 29–46.

Koshizuka, S., Oka, Y., 1996. Moving particle semi implicit method for fragmentation of incompressible fluid. Nucl. Sci. Eng. 123, 421–434.

Koshizuka, Seiichi, Oka, Y., 1996. Moving-particle semi-implicit method for fragmentation of incompressible fluid. Nucl. Sci. Eng. 123, 421–434.

Lee, B.H., Park, J.C., Kim, M.H., Hwang, S.C., 2011. Step-by-step improvement of MPS method in simulating violent free-surface motions and impact-loads. Comput. Methods Appl. Mech. Eng. 200, 1113–1125. https://doi.org/10.1016/j.cma.2010.12.001

Lee, E.W.M., Yu, K.F., Xu, L., 2013. Application of computational fluid dynamics for prediction of clogging locations in building drainage system. Int. Symp. Cib W062 Water Supply Drain. Build. 65–75.

Littlewood, K., Butler, D., 2003. Movement mechanisms of gross solids in intermittent flow. Water Sci. Technol. 47, 45–50. https://doi.org/10.2166/wst.2003.0217

Lucy, L.B., 1977. A numerical approach to the testing of the fission hypothesis 82, 1013–1024.

Maglić, L., Frančić, V., Zec, D., David, M., 2019. Ballast water sediment management in ports. Mar. Pollut. Bull. 147, 237–244. https://doi.org/10.1016/j.marpolbul.2017.09.065

Maglić, L., Zec, D., Frančić, V., 2016. Ballast water sediment elemental analysis. Mar. Pollut. Bull. 103, 93–100. https://doi.org/10.1016/j.marpolbul.2015.12.042

McDougall, J.A., Swaffield, J.A., 2000. Simulation of building drainage system operation under water conservation design criteria. Build. Serv. Eng. Res. Technol. 21, 41–51.

Mitsume, N., Yoshimura, S., Murotani, K., Yamada, T., 2015. Explicitly represented polygon wall boundary model for the explicit MPS method. Comput. Part. Mech. 2, 73–89. https://doi.org/10.1007/s40571-015-0037-8

Motezuki, F.K., Ribeiro, G.H. de S., Kurokawa, F.A., Cheng, L.-Y., 2015. Modelagem do escoamento tridimensional do concreto fresco utilizando o método Moving Particle Semi-Implicit, in: XXXVI Ibero-Latin American Congress on Computational Methods in Engineering. Rio de Janeiro, pp. 1–17.

Ng, H.C.H., Cregan, H.L.F., Dodds, J.M., Poole, R.J., Dennis, D.J.C., 2018. Partially filled pipes: Experiments in laminar and turbulent flow. J. Fluid Mech. 848, 467–507. https://doi.org/10.1017/jfm.2018.345

Pereira, N.N., Botter, R.C., Folena, R.D., Pereira, J.P.F.N., da Cunha, A.C., 2014. Ballast water: A threat to the Amazon Basin. Mar. Pollut. Bull. 84, 330–338. https://doi.org/10.1016/j.marpolbul.2014.03.053

Pereira, N.N., Brinati, H.L., 2012. Onshore ballast water treatment: A viable option for major ports. Mar. Pollut. Bull. 64, 2296–2304. https://doi.org/10.1016/j.marpolbul.2012.07.026

Pereira, N.N., Colombo, F.B., Chávez, M.I.A., Brinati, H.L., Carreño, M.N.P., 2016. Challenges to implementing a ballast water remote monitoring system. Ocean Coast. Manag. 131, 25–38. https://doi.org/10.1016/j.ocecoaman.2016.07.008

Prange, G.J., Pereira, N.N., 2013. Ship ballast tank sediment reduction methods. Nav. Eng. J. 125, 127–134.

Qi, Z., 2015. Flushing Ballast Tanks. University College London.

Qi, Z., Eames, I., 2015. Implications of ballast tank geometry and treatment technology on NIS removal. Ocean Eng. 103, 211–222. https://doi.org/10.1016/j.oceaneng.2015.04.046

Swaffield, J.A., McDougall, J.A., 1996. Modelling solid transport in building drainage systems. Water Sci. Technol. 33, 9–16. https://doi.org/10.1016/0273-1223(96)00364-2

Swaffield, J.A., McDougall, J.A., Campbell, D.P., 1999. Drainage flow and solid transport simulation in defective building drainage networks. Build. Serv. Eng. Res. Technol. 20, 73–81. https://doi.org/10.1177/014362449902000206

Tanaka, M., Masunaga, T., 2010. Stabilization and smoothing of pressure in MPS method by Quasi-Compressibility. J. Comput. Phys. 229, 4279–4290. https://doi.org/10.1016/j.jcp.2010.02.011

Tsukamoto, M.M., Cheng, L.Y., Motezuki, F.K., 2016. Fluid interface detection technique based on neighborhood particles centroid deviation (NPCD) for particle methods. Int. J. Numer. Methods Fluids 82, 148–168. https://doi.org/10.1002/fld.4213

UNCTD, 2019. World Investment Report 2019: Special Economic Zones.

Valencio, I.P., Gonçalves, O.M., 2019. Drainage and sewage system performance – Consequences of reductions in toilet flush volume. Build. Serv. Eng. Res. Technol. 40, 576–594. https://doi.org/10.1177/0143624418821079

Wilson, W., Chang, P., Verosto, S., Atsavapranee, P., Reid, D.F., Jenkins, P.T., Verosto, Stephan Atsavapranee, P., Reid, D.F., Jenkins, P.T., 2006. Computational and Experimental Analysis of Ballast Water Exchange. Nav. Eng. J. 118, 25–36. https://doi.org/10.1111/j.1559-3584.2006.tb00460.x

Yuan, H., Zhou, P., Mei, N., 2017. Numerical and experimental investigation on the ballast flushing system. Ocean Eng. 130, 188–198. https://doi.org/10.1016/j.oceaneng.2016.12.003